Università degli
Studi di Pavia

Dipartimento di Fisica
Nucleare e Teorica

Istituto Nazionale di
Fisica Nucleare

DOTTORATO DI RICERCA IN FISICA – XIX CICLO

Radiation Biophysics Modelling: track structure theoretical bases and Monte Carlo simulations of DNA damage

dissertation submitted by

Daniele Alloni

to obtain the degree of
DOTTORE DI RICERCA IN FISICA

Supervisors: Prof. Andrea Ottolenghi
Dr. Francesca Ballarini
Department of Nuclear and Theoretical Physics, University of Pavia, and INFN Pavia.

Referee: Prof. Marco Durante
Department of Physical Sciences, University "Federico II" of Naples, and INFN Naples.

… to Silvana
… and to my family.

Aknowledgements ...

First of all I would like to express my thanks to my supervisors Prof. Andrea Ottolenghi and Dr. Francesca Ballarini for their scientific advices and friendship during these long years.

I am grateful to Dr. Werner Friedland of the *GSF Institute* of Munich, friend and 'father' of the PARTRAC code, for his continuous and helpful support. I'm thankful to Dr. Marco Liotta for his help with the code during all these years, and to Dr. Giorgia Givone for the 'one-track' plots.

A special thanks goes to Prof. Domenico Scannicchio, Director of the Department of Nuclear and Theoretical Physics of Pavia and Leader of the Medical Physics Group, for his availiability, support, and frienship.

I am thankful to the colleagues of *Istituto Superiore di Sanitá* for the experimental results reported in this work. I would like to thank Prof. Marco Durante, the external referee of my thesis, for his availability and his useful suggestions.

My heart-felt thanks goes to my father and my mother who have always believed in me.

Finally, a very special thanks goes to Silvana (*the Amazing Maga Silvan and her three cats*) ... thank you for your infinite patience, support and *love* since the beginning of this story, and for having me explained some of the obscure aspects of the DNA biochemical structure.

... and special aknowledgements

I am indebited with Prof. Adalberto Piazzoli, President of `L.E.N.A.` (`Laboratory of Applied Nuclear Energy`), my *maestro* and friend for all these years of scientific support and discussions on many problems of Physics, life and death.

I am grateful to Dr. Ing. Andrea Borio di Tigliole, Director of

`L.E.N.A`, for having me introduced into the charming field of Nuclear Reactor Physics, to Dr. Andrea Salvini and all the colleagues of `L.E.N.A` and to the *cyclotronists* for their avaliability, friendship, support and scientific advices.

My personal infinite thanks goes to Dr. Michele Prata, friend and colleague and '*distiller*' of this thesis, for his helpful suggestion and for having me encouraged during these last months.

I am thankful to Dr. Alberto *Blucker* Sacchi for being the reanimator of my laptop and for the scientific, anatomic and alchoolic discussion during these years. Finally, my sincere thanks goes to *Belgian Beer* for having me relaxed after all these nights of hard work.

Daniele, Pavia, *Halloween 2007*

Contents

Introduction

[...] A poet once said, "*The whole universe is in a chalice of beer*[1]." We will probably never know in what sense he meant that, for poets do not write to be understood. But it is true that if we look at a chalice of beer closely enough we see the entire universe. There are the things of physics: the twisting liquid which evaporates depending on the wind and weather, the reflections in the glass, and our imagination adds the atoms. The glass is a distillation of the earth's rocks, and in its composition we see the secrets of the universe's age, and the evolution of stars. What strange array of chemicals are in the beer? How did they come to be? There are the ferments, the enzymes, the substrates, and the products. There in beer is found the great generalization: *all life is fermentation.* Nobody can discover the chemistry of beer without discovering, as did Louis Pasteur, the cause of much disease. How vivid is the beer, pressing its existence into the consciousness that watches it! If our small minds, for some convenience, divide this chalice of beer, this universe, into parts – physics, biology, geology, astronomy, psychology, and so on – remember that nature does not know it! So let us put it all back together, not forgetting ultimately what it is for. Let it give us one more final pleasure: drink it and forget it all!

R. P. "Dick" Feynman, in "Six Easy Pieces".

The evaluation of the risk associated to low doses of ionizing radiation is still an open question in radiation research [1]. For radiation protection purposes, the risk at low doses is generally obtained by extrapolations from data at higher doses, mainly obtained from A-bomb survivors. However, the Hiroshima and Nagasaki survivors were mainly exposed to low-LET radiation, thus providing estimations which might not hold for high-LET exposure. Astronauts' exposure to space radiation represents an example of scenario where high-LET radiation

---

[1]In the original text the object is a *glass of wine*. The choice to replace it with a *chalice of beer*, is my personal tribute to this ancient (trappist, preferably) drink.

plays a relevant role since Galactic Cosmic Rays (GCR) spectra contain a large component of high-LET particles, for example iron ions. Therefore, for a reliable risk estimations there exists a strong need for both experimental and modelling studies, the latter possibly based on radiation *track structure* simulations taking into account the complex structure of the heavy ion tracks, which are characterized by energetic secondary electrons that can travel several tens of microns far away from the primary ion track. Monte Carlo (MC) code based on a description of the track structure at the nm level, also called *event-by-event* codes, are particularly suitable as a starting basis to build soundly-based mechanistic models of the action of ionizing radiation (including heavy ions) on biological structures. The scenario at low doses can be further complicated, as will be discussed in this work, by the possible occurrence of "non-targeted" effects - typically *bystander effects* (BE) - consisting of the induction of cytogenetic damage in cells which have not suffered any energy deposition by radiation, but respond to molecular signals released by irradiated cells. These effects might play a non negligible role following exposure to radiation in space, where only a fraction of cells are traversed by radiation. This might have important implications on the estimation of low-dose risks, which is currently based on the so-called "Linear No Threshold" (LNT) hypothesis. According to this approach, the risk at low doses can be estimated by linear extrapolation of data at higher doses. Indeed, during the last decade the large amount of data on non-targeted effects has challenged the LNT hypothesis, suggesting that the risk at low doses might be not linear. Whether the risk would be most likely to be supralinear or sub-linear is still not clear, and probably it does strongly depend on the specific exposure conditions.

Chapter 1 is dedicated to a general survey of the mechanism by which different types of ionizing radiation interact with matter and track structure theory. The elements and principles of computational techniques for track structure simulation are also presented.

Track structure analysis based on computer simulations requires the cross sections for the interaction of primary and secondary charged particles with matter. Water in liquid state, being the dominant component in cells, is widely used as model substance in biophysical MC radiation transport code. Because of the intrinsic difficulties of obtaining detailed cross sections for inelastic interactions by charged particles in condensed phase matter, all of our information on such cross sections must be determined from appropriate theory.

The conventional theory, presented in Chapter 2, used to descibe inelastic processes is based on the (*plane wave*) *first Born approximation* (BA) and the *dielectric theory* (DT). The first is a perturbative treatment that is expected to be valid only for sufficiently fast projectiles, the latter is used to describe the collective response of the condensed medium to external perturbation, that is the passage of the charged particles.

Using the BA and DT, the general structure of the inelastic cross section will be expressed by the product of two distinct factors, one dealing *with the incident particle only* and one with *the target only*. The first factor is nearly trivial; the

second is the *dynamic form factor* (DFF) of the medium and it is directly related the dielectric properties of the medium, that is to the the imaginary part of (complex) *dielectric response function* (DRF) of the medium. The DRF used in such cross section calculations is estimated on the basis of optical data, experimental information and theoretical models. Input data cross sections, actually used in the PARTRAC code for heavy ion interaction in the non relativistic regime, are calculated in the framework of DT and are obtained from proton interaction cross sections by scaling with the effective charge squared (Barkas formula) the differential cross section for a proton of same velocity.

Chapter 3 is dedicated to the biological effects of ionizing radiation. A description of the DNA structure and its organization in different levels (from the DNA double-helix to chromosome territories) is given and a description of the different types of radio-induced damage are presented.

In Chapter 4 we present the biophysical Monte Carlo code PARTRAC (PARticles TRACks) used in this work and developed in collaboration with the *GSF Institute* of Munich. The recent improvement of cross sections and geometrical models of the DNA and chromatin structure makes it possible to test separately different assumptions on the mechanisms, leading from the initial radiation insult to the induction of certain biological endpoints. As shown in this Chapter, the PARTRAC code provides a detailed (atom-by-atom) description of the DNA and chromatin structures, thus making it possible to test working hypotheses on the radiation action mechanisms in a quantitative way and to perform extrapolations safer than hitherto possible to parameter regions where no experimental data exist (e.g., at low doses). The DNA target model used in the PARTRAC code includes six levels of DNA organization and completely reproduces the human genome. In this Chapter we present a study focussed on the role of DNA/chromatin organization and scavenging capacity (SC) in Ultra Soft X-Ray (USX) and proton induced DNA damages.

In the context of astronauts' exposure to GCR, Chapter 5 is dedicated to heavy ion track structure and DNA fragmentation. The recent upgrade of the PARTRAC code with implementation for heavy ions allowed us the investigation of DNA fragment spectra induced in human fibroblast by iron ions of different energy and LET. The comparison between experimental and simulation data, performed analyzing the number of radiation induced DNA fragments as a function of dose, is given showing the the predictive power of the PARTRAC code against the data concernig the number of fragments in non-experimentally detectable ranges.

Due to the large uncertainties affecting the knowledge of the mechnism governing BEs, only few theoretical models were developed until now. Remaining in the framework of MC codes, in Chapter 6 we present our diffusion-based modeling approach for the study of bystander effect following irradiation. The starting scenario of our simulations is *as controlled as possible* in order to minimize the number of assumptions and free parameters in our model. The identification of the involved signal molecules, number of released molecules per hit cell, mass, diffusion coefficient and their probability of emission/reactions are fundamental

parameters that can be modulated in order to reproduce recent experimentral results.

Ionizing radiation, track structure theory and Monte Carlo techniques

This Chapter is dedicated to a general survey of the mechanism by which different types of ionizing radiation interact with matter and track structure theory. The knowledge of the basic physics (e.g., cross sections) of radiation interaction and energy transfer is fundamental to understand the biological effects of radiation in living tissues. Microdosimetric studies have revealed how the comprehension of a large number of biological scale phenomena needs the knowledge of physical, chemical and biological events on a nanometric scale, that is the scale of the DNA double-helix . For a complete analysis of radiation effects in matter (and expecially, in this context, in biological materials), knowledge and study of track structure of incident particles (primary particles) and secondary particles is essential. This is necessary because the knowledge of physical quantities such as LET[1] (Linear Energy Transfer) or mean absorbed dose (mean absorbed energy per unit mass) are not able to explain in a detailed way the *stochastic and discontinuous sequences of energy transfer in the target material*, that is what we can define *track structure.*

The track structure approach is able to analyze in a "event by event" description quantities sush as *radial dose* and *local* characteristics of energy depositions. Non-stochastic quantities can then be obtained starting from the single elements that contribute to their definition.

In the next Sections we will describe, in a qualitatively way, the physics of radiation-matter interaction, focussing our attention on liquid water which serves as a substitute of soft tissue in most Monte Carlo codes. A summary of fundamental cross sections for these processes is given, and the effects of track structures for different kind of radiation will be explained at the end of this Chapter. Heavy charged particles are particularly emphasized since they play a central role in the effects of ionizing radiation and in this research work. Ionizing radiation is often

---

[1]See Section 1.3.

used to excite objects from their ground state to study the nature and dynamics of the processes that bring the object back to the old or to a new quasi-equilibrium state. The spatial distributions of species excited by the radiation affect their reaction probability, which in turn governs the final changes in the micro- and macroscopic structure of the material.

Along the track, the primary particle leaves ions, electrons (secondary particles), excited molecules, and molecular fragments (free radicals) that have lifetimes longer than, say 10^{-10} s. These are species that remain after the decay of plasmonlike excitations and superexcitations. The new species are the starting points of subsequential physical, chemical, and biological processes. They mark the end of the *physical stage* of radiation action and the beginning of the *chemical stage* (see Figure 1.1).
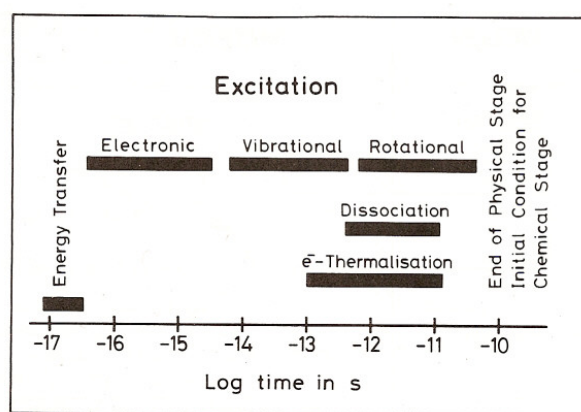
Figure 1.1: Time scale of processes occurring during the physical stage of energy transfer from ionizing radiation to molecules [11].

During the latter stage, diffusion and reaction of primary species (see Chapter 3) with other radiogenic species or with molecules of the irradiated object alter the pattern of the physical track structure.

Thus, it is the objective of *track structure theory* to

1. identify the molecular changes of importance for the development of a radiation effect under consideration;

2. predict and explain the spatial distribution of relevant species with a minimal assumption regarding preliminary processes; this spatial distribution should be given in terms of the *joint probability* to find an event of type $\mathcal{S}_1$ at position $\mathbf{x}_1$ and at the same time an event $\mathcal{S}_2$ at position $\mathbf{x}_2$ and $\mathcal{S}_3$ at $\mathbf{x}_3$, and so on, to account for spatial correlations for further reactions. In this way we can redefine the concept of track structure as an event by event description of radiation-matter interaction described by the n vectors $\mathcal{S}_j (i, \mathbf{x}_i, E)$, $j = 1, ..., n$, where i is the nature of the interaction, $\mathbf{x}_i$ is the position of the ith interaction, and E is the energy involved in this interaction (in the case of ionization events, the vectors $\mathcal{S}_j$ include the energy and emission angle of the secondary electron);

6

3. identify the parameters of the physical track structure that predominantly determine the nature and magnitude of a final radiation effect and that may also be used to characterize a radiation field with regard to its radiation action when compared to other fields.

In the following discussion it will become evident that electrons, in particular low-energy electrons, are the porters that distribute most of the energy to the individual molecules in matter and thus create most of the track structure. The interaction of electrons is described in Subsection 1.1.1. With consistent sets of interaction cross sections, track structures can be simulated on computers by means of Monte Carlo codes.

1.1 A survey on radiation-matter interaction

1.1.1 Generalities on ionizing radiation

When ionizing radiation passes through a material (gas, liquid, solid, plasma), it experiences multiple elastic and inelastic collisions with the atoms (molecules) of this material. Ionizing radiation is generally characterized by its capacity to excite and ionize the atoms and molecules of the medium where they interact. A first distinction can be done between *directly ionizing* radiation and *indirectly ionizing* radiation.

Charged particles belong to the first type, and in general they release their energy directly in the medium with electromagnetic interactions (except for highly energetic particles which can interact via nuclear reactions, losing a negligible amount of energy). We can divide these interactions in the following classes

- inelastic collisions with atomic electrons of the medium;

- elastic scattering with the atomic nucleus;

- Cherenkov emission radiation;

- nuclear reactions;

- bremsstrahlung radiation (braking radiation).

It is important to underline that, except for very high energy particles, inelastic collisions play an important role in the energy release in the medium.

The amount of energy transfer in each collision is a small fraction of the kinetic energy of the incident particle; whenever in a material of low density the number of collisions per unit path lenght is high enough to observe a substantial energy loss in thick layer of the material.

Neutrons and photons belong to indirectly ionizing radiation. First they transfer their energy to the charged particles of the medium, then these secondary charged

particles follow the same energy loss mechanism previously described for the directly ionizing radiation.

The most important interaction processes are described in terms of cross sections and treated quantitatively. Charged particles are particularly emphasized since they play an essestial role in this work. A more detailed discussion on the theory which describes charged particles interaction with biological matter will be presented in Chapter 2, when dealing with charged particle interaction in condensed matter.

Interaction of photons with matter

Unlike charged particles, photons are electrically neutral and do not steadly lose energy as they penetrate matter. On the contrary, they can travel some distance before interacting with an atom. How far a photon will penetrate is governed statistically by a probability of interaction per unit distance travelled, which depends on the specific medium traversed and on the photon energy. When a photon interacts, it might be absorbed and disappear or it may be scattered, changing its direction, with or without loss of energy.

Photons having sufficient energy to cause ionizations in the irradiated material interact - depending on the energy and atomic composition of the exposed substance - via four main processes

- elascic scattering without energy transfer;

- Compton scattering;

- photoabsorption (or photoelectric process);

- pair formation.

The first case will not be treated since it does not contribute to biological radiation effects. For the sake of completeness, the interaction with nuclei (nuclear photoeffect) must be mentioned, but because of its minor importance it will be not further discussed.

A photon imparts a large fraction of its energy to a single electron, which then ionizes many other molecules along its path. The track generated by a photon is therefore an electron track.

Electrons set in motion by inelastic photon collision in turn excite and ionize other molecules. Thus the original photon can produce an avalanche of higer generation electrons with decreasing starting energies, which all contribute to the track formation.

Compton cross section

This is the special case of a collision between a photon with an atomic electron which is considered free, i.e. the photon energy is much larger than the electron's binding energy. The collision theory applied to this case gives the differential

8

cross section $d\sigma_e$ for an energy transfer T_2' (energy of the scattered electron) per scattering electron

$$d\sigma_e\left(T_2'\right) = \frac{\pi r_0^2 m_{e0} c^2}{\left(h\nu_1\right)^2} \left\{ 2 + \left(\frac{T_2'}{h\nu_1 - T_2'}\right)^2 \left[2 + \left(\frac{T_2'}{h\nu_1 - T_2'}\right)^2 \times \right.\right.$$

$$\left.\left. \times \left(\frac{m_{e0}^2 c^4}{\left(h\nu_1\right)^2} + \frac{h\nu_1 - T_2'}{h\nu_1} - \frac{2m_{e0}c^2}{h\nu_1} \cdot \frac{\left(h\nu_1 - T_2'\right)}{T_2'}\right)\right]\right\} dT_2' \quad (1.1)$$

where $r_0 = 2.818 \times 10^{-15}$ m is the classical electron radius, $h\nu_1$ is the energy of the incoming photon.

The total cross section σ_e for the total number of scattering events is obtained by integration of the previous relation for $0 \le T_2' \le T_{2\,\text{max}}'$, where $T_{2\,\text{max}}'$ is given by

$$T_{2\,\text{max}}' = \frac{h\nu_1}{1 + \frac{1}{2}\frac{m_{e0}c^2}{h\nu_1}} \quad (1.2)$$

yelding the result

$$\sigma_e = 2\pi r_0^2 \left[\frac{1+\alpha}{\alpha}\left(\frac{2\left(1+\alpha\right)}{1+2\alpha} - \frac{1}{\alpha}\ln\left(1+2\alpha\right)\right) + \frac{1}{2\alpha}\ln\left(1+2\alpha\right) - \frac{1+3\alpha}{\left(1+2\alpha\right)^2}\right] \quad (1.3)$$

with $\alpha = h\nu_1 / m_{e0}c^2$.

The probability for a Compton scattering depends on the number of electrons in the medium and is, therefore, proportional to Z. The dependence on the incident photon energy is given by Eq. (1.3). For low energies ($\alpha \ll 1$) the following expansion can be used

$$\sigma_e \approx \frac{8}{3}\pi r_0^2 \left(1 - 2\alpha + ...\right) \quad (1.4)$$

whereas, a good approximation for high energies ($\alpha \gg 1$) is given by

$$\sigma_e \approx \pi r_0^2 \frac{1 + 2\ln 2\alpha}{2\alpha} \quad (1.5)$$

Photoeffect cross section

In the preceeding description of the Compton process it is possible to show, using the collision theory, that photons can never transfer their energy completely to free electrons. This is not the case with low photon energies where the binding energy of the electron can no longer be neglected. Conservation of momentum can then be secured by transfer to the atom as a whole. In this way the kinetic energy of the electron is given by

$$T_2' = h\nu_1 - E_B \quad (1.6)$$

where E_B is the electron binding energy.

Cross sections, therefore, no longer apply to single electrons but to the atom as a whole. An acceptable approximation is given by

$$\sigma_A \approx \frac{Z^4}{(h\nu_1)^3} \tag{1.7}$$

where σ_A is the atomic cross section and Z is the nuclear charge of the medium.

Pair creation cross section

If $h\nu_1 > 2m_{e0}c^2$, i.e., if the photon energy is larger than twice the rest energy of the electron, the photon may "materialize" by the formation of an electron-positron pair. Pair formation does not occur in vacuo, it requires the partecipation of an intense electric field, normally that of an atomic nucleus which receives also part of the photon momentum. The photon energy is distributed between the rest energy and the kinetic energy of the two particles created

$$h\nu_1 = T_{electron} + T_{positron} + 2m_{e0}c^2 \tag{1.8}$$

The calculation of interaction cross sections is complex. In a first approximation, the atomic cross section σ_{pair} is proportional to the square of the nuclear charge of the medium and to the photon energy

$$\sigma_{pair} \approx Z^2 \cdot h\nu_1 \tag{1.9}$$

The particles formed may have high energies. They will ionize atoms along their path, but they may also emit bremmstrahlung radiation thus giving up again part of the initially absorbed energy.

Summary of photon interaction cross sections

The total interaction cross section is the sum of those of the single components. This means that on a *per atom* basis we have

$$\sigma_{total} = Z \cdot \sigma_{Compton} + \sigma_{photo} + \sigma_{pair} \tag{1.10}$$

The Compton cross section is multiplied by the electron number (equal to the nuclear charge Z of the atoms in the medium) since it is related to single electrons. While in the photo and pair-formation process the photon energy is completely absorbed, this is not the case of Compton scattering. The absorption cross section σ_a per atom is

$$\sigma_a = \frac{\sigma_e \cdot T_2'}{h\nu_1} \tag{1.11}$$

so that the total absorption cross section $\sigma_{a\ total}$ per atom becomes

$$\sigma_{a\ total} = Z \cdot \frac{T_2'}{h\nu_1}\sigma_{e\ Compton} + \sigma_{photo} + \sigma_{pair} \tag{1.12}$$

The Fig. 1.2 shows the cross section dependence on energy, with water as absorbing medium.
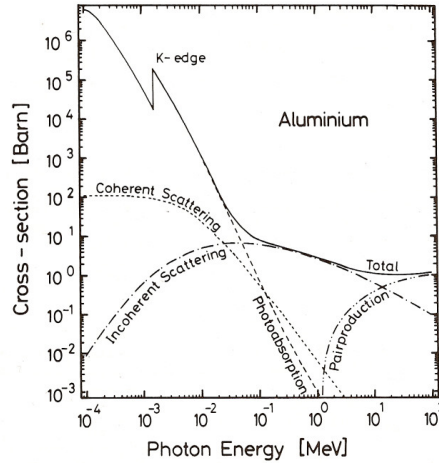
Figure 1.2: Cross sections (in barn/atom; 1 barn = $10^{-28}m^2$) for various types of interaction of photons with aluminium, a typical low-Z material [11].

Interaction of neutrons

Neutrons may interact with matter via five processes if scattering without energy transfer is excluded

- elastic collision;

- inelastic collision;

- non elastic collision;

- capture;

- spallation.

The first case represents the 'classical' collision; in the second, a neutron is captured by an atomic nucleus and emitted with changed energy; while in the third, the neutron is reejected as a part of another partice, e.g. an α particle. In the capture reaction, the neutron remains in the nucleus and a different particle or γ photons are emitted. Spallation is the fragmentation of a nucleus leading to a number of various reaction products. Except for elastic collision, nuclear excitation is a common side-reaction without concomitant emission of γ quanta. The probability of any interaction to occur depends on the neutron energy. In the lower range - below 5 MeV - only the elastic collisions play asignificant role, except for very low energies (below 100 keV) where capture reactions dominate. Most of them are (n,p) processes, i.e. upon neutron capture, a proton is ejected. Inelastic and non elastic interactions begin to become significant above 2.5 or 5

MeV, respectively, spallation around 20 MeV. In all these cases, part of the energy is also transferred to γ quanta which are emitted from excited nuclei.

For most practical purposes, however, elastic collision is the major energy transfer process. The fundamental parameter for the mechanism of energy loss depends on the mass ratio of the two collision partners and is largest if they possess equal masses (in fact, in thermal nuclear reactors, hydrogen contained in water molecules is the fundamental element for the slowing down and moderation of neutrons coming from the fission of fissile neclei). When the taget is biological, that is for example a tissue, the water contained in the target plays an inportant role in the generation, after neutron interaction, of charged secondary particles. For this reason the actual energy deposition in the medium is essentially due to charged secondary particle, i.e. mainly protons. The situation is, therefore, comparable to that of electromagnetic radiation where the electrons play this role. Neutrons - like photons - are indirectly ionizing.

Many details on cross section interactions and processes regarding neutrons can be found, for example, in [2, 3].

Interaction of heavy charged particles: protons and ions

Monte Carlo simulations of the passage of heavy charged particles (protons and ions) in the cell nucleus, and the study of the ion-induced fragmentation effects on DNA, are one of the main part in this work. A heavy charged particle traversing matter loses energy primarly through the ionization and excitation of atoms and molecules. The moving charged particle exerts electromagnetic forces on atomic electrons and imparts energy to them. The transferred energy may be sufficient to knock an electron out of an atom and thus ionize it, or it may leave the atom in a excited, nonionized state. As we will show in Subsection 1.2.2, a heavy charged particle can tranfer only a small fraction of its energy in a electronic collision. Its deflection in a collision is negligible. Thus a heavy charged particle travels an almost straight path through matter, losing energy almost continuously in small amounts through collisions with atomic electrons, leaving ionized and excited atoms in its way. In contrast beta particles (e^- or e^+), can lose a large fraction of their energy and undergo large deflections in single collisions with atomic electrons. Thus they do not travel in straight lines. An electron can also be sharply deflected by an atomic nucleus, causing it to emit photons in bremsstrahlung process. For ions with specific energy E per mass in the range 0.5-100 MeV/u, around 65-75 % of the energy lost is transferred to and then transported by secondary electrons, 15-25 % is needed to overcome their binding potential, and the residual 5-10 % produces neutral excited species. The large fraction transferred to secondary electrons emphasizes the importance of electrons also in this context. For 0.8 MeV/u particles, around half of all ionizations are produced by the fast ion itself, and the rest by its secondary electrons. With increasing ion energy, two out of three ionizations are ultimately due to secondary electrons and are thus not necessarily located close the ion path.

Heavy charged particles interact with matter - depending on their energy - by

three main processes

- electron capture (low energies);

- collision with atomic electrons (medium and high energies);

- nuclear collisions and nuclear reactions (very high energies).

The first point is a new interaction process for fast ions, compared to electrons. Heavy charged particles of energy in the range 0.1-5 MeV can capture electrons from target molecules into their own continuum state (charge transfer to the continuum), which leads to the ejection of additional secondary electrons. These have essentially the same velocity as the ion and travel in essentially the same direction. The last point is of less importance for this thesis and will not be detailed; it plays a role, however, with very energetic ions where it leads to fragmentation of the incoming particle so that an originally "pure" beam is contaminated with lighter ions. This effect has to be taken into account in the determination of the so-called depth-dose curves. Most important is the collision with electrons where the interaction is mediated by the electric field of the two partners and depends, therefore, on the impact parameter. With larger distances (large impact parameters), the amount of energy transferred is small so that the binding energy of the electron may no longer be neglected. These events are named "glancing" or "soft" collisions. The analytical treatment requires quantum-mechanical considerations, which are given in the literature. As a result of these interactions, the atoms are not only ionized but also excited. The probability of these to occur depends on the particular properties of the medium. In this case, the reaction cannot be treated as a collision between the ion and a free electron, and the atom or molecule interacts as a whole.
With small impact parameters, i.e. large energy transfer compared to the electrons binding energy, the situationis is simpler. From a theoretical point of view this means the possibility to apply the formal pertutbation treatment on the collision dynamics (as we will see in Chapter 2 in the case of heavy charged ions). Many total and differential cross sections for protons and a few other fast ions have been measured or derived from theories [4, 5]. The magnitude of cross sections of charged particles is proportional to the square of their electric charge Z. The classical Rutherford cross section is

$$\frac{d\sigma}{dE} = 4\pi a_0^2 R^2 \frac{Z^2}{T} \frac{1}{Q^2} \tag{1.13}$$

where

$T = \frac{1}{2} m_e v^2$
$m_e =$ electron mass
$v =$ ion velocity
$Q = E + U =$ energy transfer

13
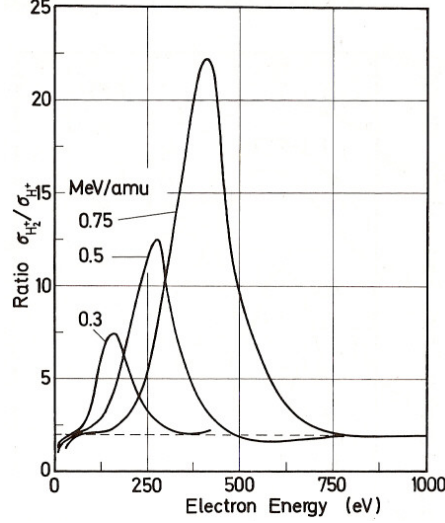
Figure 1.3: Ratio of eneregy differential cross sections for the production of secondary electrons by H_2^+ and H^+ projectiles of various specific energies impinging on hydrogen gas [11].

This relationship is approximately correct for bare nuclei or fast ions with tightly bound electrons, but the assumption that it holds also for fast ion with loosely bound electrons is not correct. Fig. 1.3 shows an example of this failure.

The ions H_2^+ and H^+ are both singly charged and a constant cross section ratio might be expected, but over a wide secondary electron energy range the contribution of the ejected electron of the H_2^+ molecule shows that such a simple scaling from proton cross sections to heavy-ion cross sections is not obtained. Scaling from proton data to heavier ions is done with the so called *effective charge* Z^* for the specific ion. The quantity Z^* depends on ion energy and the interacting medium. It becomes smaller with low velocities because of electron capture. There are a number of semiempirical expressions avaiable for its calculation based on different assumptions, but not a generally accepted theory applicable for all media. Because of the lack of experimental data, the uncertainties are many, particularly for heavy ions. A useful approximation for water - still widely popular in radiation biology - is the *Barkas formula* wich is given by

$$Z^*(\beta) = Z \left[1 - \exp\left(-125\beta/Z^{2/3}\right)\right] \tag{1.14}$$

where Z is the ion atomic number and $\beta = v/c$ its relative speed. We will return to this relation in Chapter 2.

Interaction of electrons with matter

Like heavy charged particles, electrons can excite and ionize atoms. In addition, they can also radiate energy by *bremsstrahlung* (braking radiation). Electrons are of primary importance in the caracterization of the track structrure of all the type of ionizing radiation in matter: all the energy of photons or fast primary electrons is transferred to matter by secondary electrons (or by electrons of higher

generations) and the same can be said for the energy loss of heavier particles as neutrons, protons or ions. Four main processes are important in the interaction of electrons with matter

- collision with shell electrons;

- bremsstrahlung;

- Cerenkov radiation;

- nuclear reactions.

Nuclear processes, which play an important role only at very high energies can be disregarded here. Collisions basically follow the same rule as with ions, but a non-relativistic treatment is generally not appropriate. Further complications arise by the fact that incoming and outgoing particles cannot be distinguished (a detailed treatment is beyond the scope of this work). The differential cross section is given by the Moeller formula

$$\frac{d\sigma_e}{dT_2'} = \frac{2\pi e^4}{(4\pi\varepsilon_0^2)\, m_{e0}c^2\beta^2} \cdot \frac{\left[1 - \frac{T_2'}{T_1} + \left(\frac{T_2'}{T_1}\right)^2\right]^2}{\left(1 - \frac{T_2'}{T_1}\right)^2 \cdot T_2'^2} \tag{1.15}$$

where the notation for electron kinetic energies have the same meaning as for Eq. (1.1).

With higher energies, *bremmsstrahlung* becomes more and more important. This kind of radiation is caused by the deceleration of electrons in the field of the nucleus and depends, therefore, on the atomic composition of the medium. Knowing the collision and radiative losses for electrons, a useful rule of thumb for the bremmstrahlung radiation is given by

$$r = \frac{T_1 \cdot Z_M}{700} \tag{1.16}$$

where r is the ratio between collision and radiative losses, T_1 is the electron energy in MeV, and Z_M is the atomic number of the medium.

Cerenkov radiation is generated if the speed of a charged particle passing through matter exceed that of ligth in the medium. This criterion sets a lower limit below which this process does not occur (about 500 keV for water). In terms of energy loss, it is usually not important but may lead to the generation of ultraviolet light which may then be responsible for a certain biological radiation damage.

Electron interactions leading to ionization of a molecule (a) cause the ejection of another electron (which in turn might be able to ionize another molecule); (b) usually leave the molecule in an excited state that can decay by dissociation, Auger electron emission, photon emission, and so on; and (c) involve relatively large energy transfer.
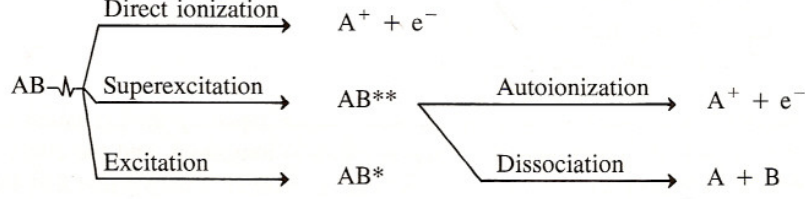
Figure 1.4: Dissociation schemes of molecules after radiation energy transfer.

Elastic collisions also contribute to electron track structure. Though not leaving a mark in the irradiated matter themselves, they influence the location of the next inelastic event, and this factor has to be considered when one constructs the physical part of the Monte Carlo codes, in which cross sections for each type of collision are the fundamental inputs for track structure simulations. For a rigorous calculation of charged particle track structure a set of absolute elastic, excitation, and ionization cross sections is needed for the atoms and molecules of the medium, expecially when the tools for the study of track structure are Monte Carlo techniques. Complete and accurate data sets are not yet avaliable for any material. However, useful estimate for such cross sections can be derived from singly or doubly differential cross sections, from integral data, from data on low-energy photoabsorption, and from theoretical considerations. Estimates for condensed media are usually extrapolated from gas phase data. For electrons a large literature exists on experimental and theoretical cross sections [6, 7, 8, 9, 10].

Analysis of photoabsorption and electron scattering data and theoretical considerations about the energy levels of the molecule under consideration are necessary to derive elastic and inelastic electron scattering cross sections and to check their internal consistency and theys consistency whith theoretical constraints. The asymptotical behaviour of the total cross section for inelastic scattering of high energy electrons is given, according to Bethe, by

$$\sigma = AT^{-1} \ln T + BT^{-1} + CT^{-2} + ... \tag{1.17}$$

where A, B, and C are constant depending on the medium properties, and T is the energy of the incident electron. The kinetic energy spectra of secondary electrons is important for radiation track structure theory. Unfortunately, not many absolute experimental data exist for such cross sections. In the first Born approximation[2] the singly differential cross section for the production of secondary electrons of energy E is

$$\frac{d\sigma}{dE} = \frac{4\pi a_0^2}{T} \sum_i \left[\frac{df}{dQ_i} \frac{R^2}{Q_i} \ln \left(\frac{4TRC(Q_i)}{Q_i^2} \right) + B(T, Q_i) \right] \tag{1.18}$$

where

---

[2]See Chapter 2 for a more detailed description of the Born approximation.

$Q_i = E + U_i =$ energy transfer

$U_i =$ binding energy in ith orbital

$df/dQ_i =$ dipole oscillator strength for ionization with energy transfer Q_i

where the function $C(Q_i)$ depends only on the target molecules, not on the incident particle.

The starting point for a study of the energy deposition of electrons is their stochastic track structure. Input data for track structure calculations are cross sections for all relevant interactions derived from experimental data and theory.

1.1.2 Kinematics of collisions: maximum energy transfer

Assuming that the the particle is moving rapidly compared with the electron and that the transferred energy is large compared with the binding energy of the electron in the atom, we give the maximum energy that a heavy charged particle can lose in colliding with atomic nucleus. Using non relativistic elementary collision theory the resul is given by the formula

$$Q_{\max} = \frac{1}{2}MV^2 - \frac{1}{2}MV_1^2 = \frac{4mME}{(M+m)^2} \tag{1.19}$$

where $E = MV^2/2$ is the initial kinetic energy of the heavy particle, M and m are the mass of the heavy particle and electron, respectively, and V, V_1 are the velocities of the heavy particle before and after the collision, respectively. Note that when the two masses are equal $(M = m)$ the previous equation gives $Q_{\max} = E$; so the incident particle can transfer all of its energy in a billiard-ball type collision.

The exact relativistic expression for the maximum energy transfer is

$$Q_{\max} = \frac{2\gamma^2 mV^2}{1 + 2\gamma m/M + m^2/M^2} \tag{1.20}$$

where $\gamma = 1/\sqrt{1-\beta^2}$, $\beta = V/c$. Except at extreme relativistic energies, $\gamma m/M << 1$, in which the case the previous formula reduces to

$$Q_{\max} = 2\gamma^2 mV^2 = 2\gamma^2 mc^2\beta^2 \tag{1.21}$$

which is the usual relativistic result.

1.2 Stopping power

The tracks of heavy charged particles are often characterized by their mean rate of energy loss and their range. This mean rate, the *stopping power*, has been the object of many theoretical and experimental studies, which led to substantial knowledge about the general principles . However the accuracy for actual stopping power values for charged particles heavier than α particles and for all particles at

low energies is far from satisfactory. When a fast charged particle passes through a material (gas, liquid, solid, plasma) it experiences multiple elastic and inelastic collisions with the atoms (molecules) of this material.

Let $\langle \Delta E \rangle$ be the *mean energy lost* by the particle as it travels along a path segment Δx. In the case of small Δx the quantity $\langle \Delta E \rangle$ is proportional to Δx. Therefore, the rate at which the particle loses energy is conveniently characterized by the ratio $\langle \Delta E \rangle / \Delta x$ depending, in the limit $\Delta x \to 0$ on the mass, charge, and velocity of the particle and on the properties of the material in the vicinity of the point where the particle is found. In this limit the ratio is conventionally termed the *stopping power of the material* and is denoted by $-dE/dx$; this notation takes into account that the change in energy of a particle passing through a material is always a negative quantity (so $-dE/dx$ is a positive quantity). The stopping power introduced has the dimension of *energy/length*, i.e. MeV/cm or keV/μm, for example. The path covered by the particle in a material can be measured not only in centimeters or microns, but also by the mass of the layer covered, for example in units of g/cm^2

$$X = \rho x \tag{1.22}$$

where ρ is the density of the medium. Connected with this is another, equivalent, definition of the stopping power

$$-\frac{dE}{dX} = \frac{1}{\rho}\left(-\frac{dE}{dx}\right) \tag{1.23}$$

This quantity is called the *mass stopping power*; its dimensions are, for example MeV/(g/cm^2).

A fundamental contribution to the stopping power of a material is due to inelastic collisions of a particle with atoms in the medium when the energy of the particle is spent on excitation or ionization of the atoms. Further, we shall see that ionization processes are more essential here than are excitation processes, which are not accompanied by the atoms losing their electrons. In this connection, the stopping power of charged particles passing through a material is usually called *ionization stopping*, and the energy losses occurring in the stopping process are termed *ionization losses*. The energy loss per unit path, i. e., the stopping power of a material $-dE/dx$, is termed *ionization stopping power*. Our task consists in expressing the stopping power of a material through the characteristics of quantum collision processes of a particle with individual atoms of the material. We will return to this concept and to a direct calculation of this fundamental quantity in Chapter 2 when dealing with the important case of heavy charged particles in condensed matter.

1.3 Remarks on radiation energy deposition: dose and LET

Energy transfer by radiation to biological systems is both of foundamental and practical importance. The central quantity with ionizing radiation is the dose (absorbed energy per unit mass). However, there is a difference between transferred energy and deposited energy, as will be expalined. The spatial distribution of absorption events also plays a significant role, which is macroscopically described by the *Linear Energy Transfer* (LET). The applicability of this concept is discussed and the differences with stopping power are briefly presented in the following.

1.3.1 Dose

Ionizing radiation transfer energy to matter through ionizations and excitations is dicsussed extensively in the foregoing Sections. Most significant is the fact that the interacting entities - particles or quanta - do not deposit energy by a single event, and that secondary particles are liberated which are able to transport energy away from the site of primary interaction. A detailed treatment of relevatnt problems is only possible within the framework of a general transport theory and is not given here, where we restrict ourselves to a simplified discussion.

Fig. 1.5 summarizes the situation in a small mass element. An ionizing particle or quantum of energy E enters the volume where it loses an energy amont dE by creating either electromagnetic radiation (quantum energy $E'_{\gamma i}$) and/or a secondary particle (kinetic energy T'). Only parts of these energies, namely $E_{\gamma i}$ and T_i remain in the mass element since the secondary radiation may leave the volume carrying away a certain fraction of the originally transferred energy. Here it becomes clear why it is necessary to distinguish between *transferred energy* and *deposited energy*.
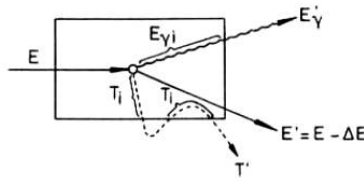
Figure 1.5: Schematic view of energy released and absorbed in matter [12].

The energy dE_{abs} absorbed in the volume, according to Fig. 1.5 is

$$dE_{abs} = U + E'_{\gamma i} + T'_i \tag{1.24}$$

where U is the binding energy of the secondary particle. The total transferred energy dE is

$$dE = U + E' + T' \tag{1.25}$$

19

i.e. $dE \geq E_{abs}$. Both are equal only if the path of the secondary particle lies completely inside the mass element and if there are no radiative losses. In the case of secondary particle equilibrium each outgoing particle is exactly compensated by an entering one of the same type and energy. The *dose* is defined as the expectation value of the absorbed energy divided by the mass dm of the volume

$$D = \frac{\overline{dE_{abs}}}{dm} \tag{1.26}$$

The unit of dose is the Gray (Gy) wich equals 1J/1kg.

1.3.2 Linear energy transfer (LET)

As pointed out in previous Subsections, the energy deposition in an exposed medium is mediated almost exclusively by charged particles. These cause ionizations on their way loosing parts of their energy in succesive steps until they reach the end of their range. Depending on the type of particle, the ionizations are more or less spaced, which is, of course, very important if one considers energy depositions in very small sites (for example in the cell nucleus). The situation may be described, for instance, by the energy loss of a particle per distance travelled. The corresponding quantity is called *Linear Energy Transfer* (LET), which is defined as the amount of transferred energy per unit length. Besides the LET_∞, also the 'restricted LET' is used, which is the locally transferred energy per unit length. The attribute 'locally' is of special importance since it postulates that only the energy fraction is counted which leads to ionizations and/or excitations within the considered site. The remaining kinetic energy of particles leaving the site is excluded. This case is particularly relevant with electrons since they may possess considerably long ranges. It has become customary to specify a limit of energy deposition below which the deposition is considered to be local (energy restriction); 100 eV has been widely accepted, which corresponds to an electron range of about 5 nm. Electrons of longer ranges are called 'δ electrons' or 'δ rays'.

The total transferred energy per unit lenght is the stopping power $-dE/dx$, as introduced in Section 1.2. It is numerically equal to LET_∞, i.e. without restrictions. There is however a conceptual differences: the stopping power deals with the energy loss of the particle, while the LET focuses on the energy deposition in the medium. The energy limits are also called cut-off energies, their values in eV are indicated by subscript to LET.

1.3.3 Sparsely- and densely-ionizing radiation

One of the most important characteristics of track structure for damage induction in small targets (e.g. cell nucleus) is the capacity to form event '*clusters*'. With this characteristic, radiations are usually divided into two groups: *densely ionizing* and *sparsely ionizing* radiation. In Fig. 1.6 is presented the energy deposition frequency higer than E per unit dose in a target cylinder of height and diameter of 25 nm: it is possible to note how low-LET radiation (sparsely ionizing) produces

a higher number of energy depositions with respect to the high-LET radiation (densely ionizing).
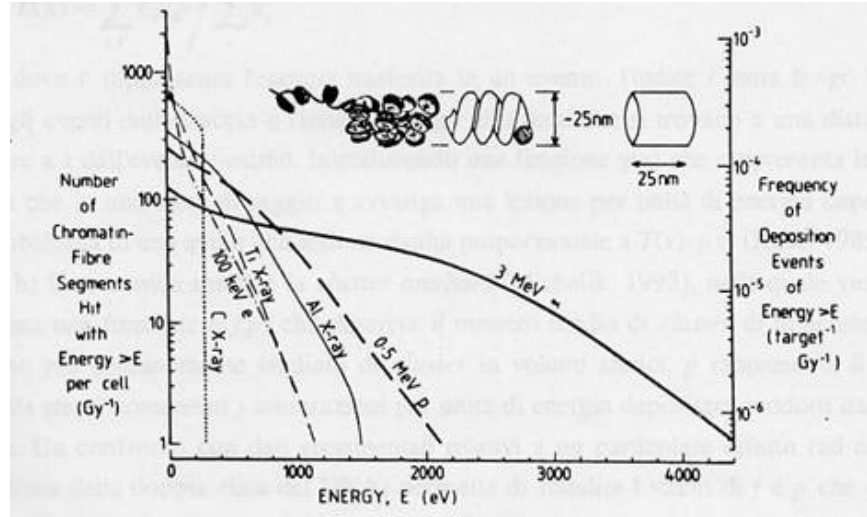
Figure 1.6: Frequencies of energy depositions in a cylinder with dimension 25×25 nm (chromatin fiber dimension) for different LET radiation. The scale on the right indicates the energy deposition frequencies greater than E per unit dose; the scale on the left indicates the number of cylinder hit with a energy greater than E per unit dose and cell. There are underlined the different characteristics between densely and sparsely ionizing radiation.

For this reason low-LET radiation is more effective in the induction of damages produced also by small energy depositions, while, on the contrary, high-LET radiation is more effective with a higher energy threshold. In other words, densely ionizing radiation has a lower probability to hit the volume under consideration, but when it happens it has a higher probability of damage induction. However, this distinction is not enough to justify the different behaviour of these two types of radiation on the biological level. It has been widely verified that different radiation qualities, with the same LET, produce different effects in matter. For this reason, for a detailed study of the basic mechanisms of radiation induced damage it is necessary to analyze the nanometric spatial distribution of each sigle event and their relative interaction probabilities.

1.4 Elements of computational techniques for track structure simulation

Averaged quantities like absorbed dose, energy imparted to a target site, and stopping power do not accurately predict physical, biological, or chemical radiation effects. The reason is the stochastic nature of such processes. Track structure theories [11] give deeper information about spatial and temporal aspects of the consequences of radiation. Track structure calculations require adequate cross sections for the relevant processes in the material under consideration. The generation, synthesis, and testing of cross sections consumes most of the time spent

21

on a problem. Once a satisfactory data base has been derived, one can use Monte Carlo techniques to simulate charged particle track structure with a computer, event by event. The cross sections (that are the fundamental inputs of simulations) have to be processed in a way that speedy sampling from the probability distributions is permitted.
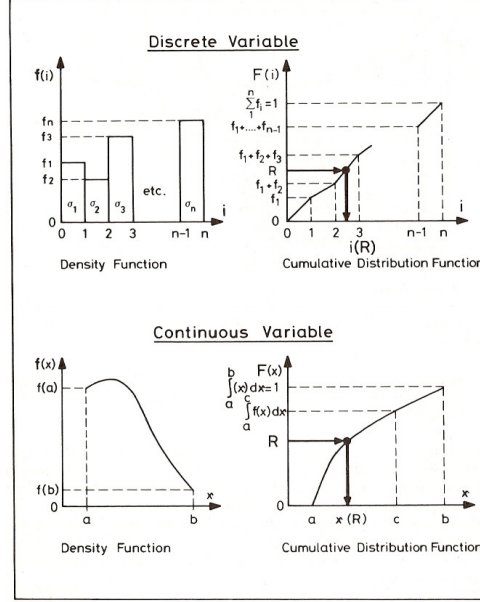
Figure 1.7: Principles of random sampling from discrete and continuous distributions [11].

To this purpose, it is useful to derive and store the mean free paths between subsequent collisions for primary and secondary particles. For the same reason it is necessary to precalculate for all relevant processes (each described by its own cross section) the ratios of their cross sections to the total cross section. The cumulative distribution function $F(i)$ of the discrete density of the ratios $f(i)$ can be stored and used directly to sample from it (with the help of a *random number generator* which gives the random number R) the type $i(R)$ of the interaction at the next collision (Fig. 1.7) so that

$$\sum_{i=1}^{j-1} f_i = F_{j-1} \leq R \leq \sum_{i=1}^{j} f_i = F_j \tag{1.27}$$

with R uniform (in a distribution sense) on the interval $[0; 1)$.

For a continuous variable x (distance to the next event, energy of secondary electron, scattering angle and so on) the following equation has to be solved for x

$$R = \frac{\int_0^x dx' f(x')}{\int_0^\infty dx' f(x')} \tag{1.28}$$

In both cases random numbers are needed, the use of which are the main characteristics of Monte Carlo techniques and calculations.

The *probability density* for the distance to the next collision along the line of flight between s and $s + ds$ is for any particle

$$p(s) = \frac{1}{\lambda} \exp(-\lambda s)\, ds \qquad (1.29)$$

where λ is the *mean free path* between collisions (expetation value of the distance between two succeeding events). This leads to the sampling scheme of the distance s to the next event,

$$s = -\lambda \ln R \qquad (1.30)$$

with R uniform in $[0, 1)$.

During an interaction a photon, neutron, or charged particle can be scattered into a new direction. This can be taken into account by

1. using appropriate coordinate frames, namely a fixed Cartesian coordinate frame at a meaningful point of reference and local spherical coordinate frames with moving origins at the actual points of collisions, with their polar axes coincident with the path of flight (Fig. 1.8);

2. Euler angle transformation of the direction cosines after scattering in the local frame into new direction cosines in the fixed frame.
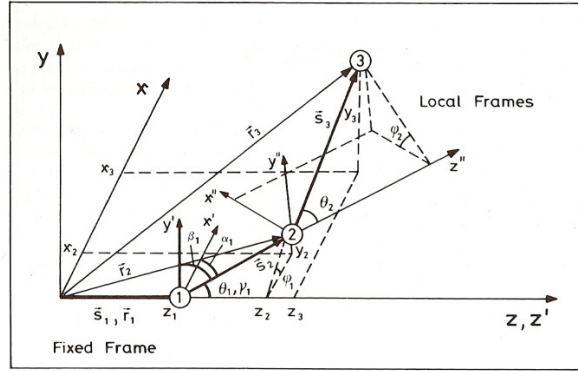
Figure 1.8: Coordinate systems used in Monte Carlo track structure calculations and relevant direction cosines [11].

With the flight distance s to the next event determined by Eq. (1.30), this gives the Cartesian coordinates of the event in the fixed frame for processing and evaluation; then the next event can be calculated, and so on.

These are the computational principles of Monte Carlo radiation track structure calculations. A succesful application of this technique is presented in Chapters 4 and 5 in the context of the PARTRAC code used in this work.

23

1.4.1   Characteristics of photons and neutrons tracks

Photons and neutrons in most cases produce primary events separated by distances that are large compared to the ranges of their secondary charged particles. This is illustrated in Fig. 1.9 for water and air. Therefore, the track structures produced by primary electrons, protons, and heavier ions are similar to those produced by photons and neutrons. However, with photons and neutrons, two radiations
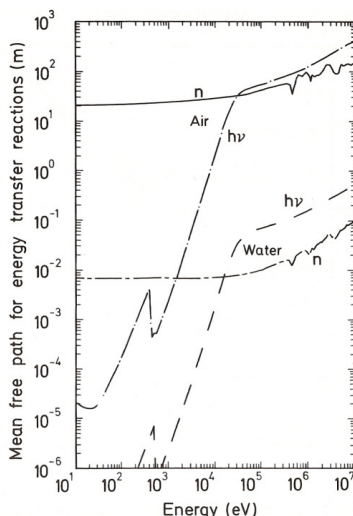
Figure 1.9: Mean free paths for energy transfer reactions of neutrons and photons in dry air and water [11].

more than one particle sometimes leaves the same affected atom or molecule, for example, because of Auger electrons emission after shell ionization, or an $(n, 3\alpha)$ reaction. An important characteristic of photon and neutron track structure, is that the ranges of secondary particles from neutrons (mainly protons and heavier charged particles) are much shorter than those of photons (electrons). Therefore, for the same absorbed dose neutrons have a smaller chance to affect a certain small site of interest in the irradiated matter. However, if the small site happens to be affected, the amount of energy to the site in this interaction is much larger (because of the higher stopping power of ions compared to that of electrons). This consideration is useful for the determination of the specific biological effects after irradiation.

1.4.2   Sructure of electron tracks

Electron track structures have been calculated for energies from about 10 eV to several MeV, for gases, liquids and solids. Here a few characteristic results are shown, using tracks of keV electrons in water vapour.

Fig. 1.10 is a two-dimensional projection of three dimensional tracks generated by computer simulations, which originally contain full information about the location of each event and its physicochemical nature. The figure shows that (a)
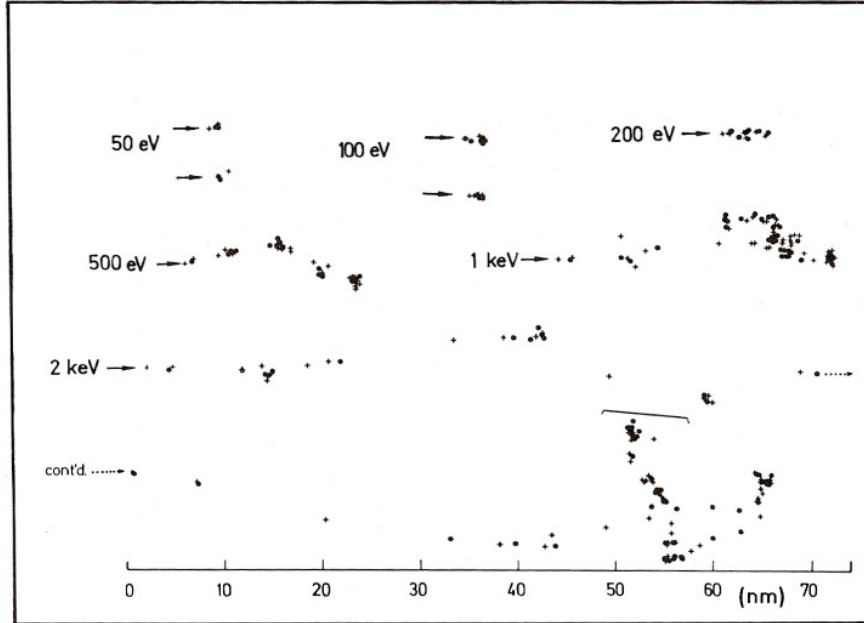
Figure 1.10: Two-dimensional projections of electron tracks in water vapor calculated with a Montecarlo simulation program previous to PARTRAC (MOCA-8) [11]. For graphical reason the 2 keV electron track is continued in the last line. For this plot all 20 types of activations are divided into two classes: +, excitation; •, ionization [11].

the number of events increases with electron energy, (b) with increasing electron energy the mean distance between inelastic collisions increases, (c) electrons suffer appreciable angle scattering, and (d) the event density is particularly high in the track ends of the primary and secondary electrons. The largest number of events with small distances to their neighbors can be found in tracks of electrons of around 500 eV; electrons with lower energy produce less events per energy deposited, and those with higher energies produce them further apart on the average.

1.4.3 Structure of proton tracks

Figure 1.11 shows simulations of three tracks each of short fragments of 0.3-, 1-, and 3 MeV protons in water vapor to demonstrate the similarities and differencies between fast ion tracks of the same energy compared to those of different energy. In general, these tracks are straight because the heavier mass of fast ions prevents them from being scattered as much as electrons in elastic and inelastic collisions. With increasing ion energy, the relative fraction of all events produced directly by the fast ion decreases from more than two-thirds for energy T around 0.3 MeV/u to around one-third at 5 MeV/u. The fraction of events on or close the ion path also decreases. This is due to the $T^{-1} \ln T$ behaviour of the secondary electron inelastic cross sections, and the 'hardening' of the secondary electron spectrum with increasing ion energy (the secondary electron maximum energy increases with T). The linear density of fast secondary electrons along the ion path, however, is

25
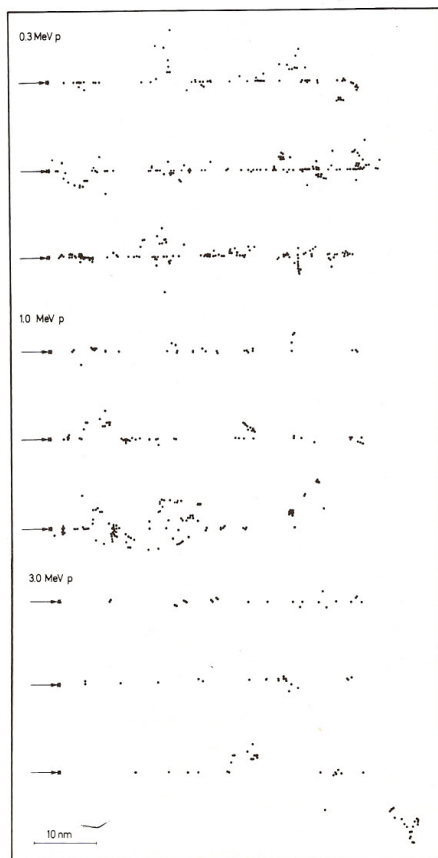
Figure 1.11: Proton track segments in water (0.3, 1.0, and 3.0 MeV, three tracks per energy) calculated with anoter Monte Carlo simulation program previous to PARTRAC (MOCA-14) [11].

rather small, and it decreases with increasing secondary electron energy ($\propto E^{-2}$). Therefore the usefulness of defining a *radial dose* concept and calculation for the classification of heavy ion tracks, which averages the energy deposited by secondary electrons at a certain radial distance from the ion path along the path. It is important to note that the differences in the three track structures produced by protons (and tracks of the same type for other particles) of the same energy are completely due to the *stochastic nature of all single-collision processes.*

1.4.4   Structure of heavy charged particles tracks

For protons and α particles, experimental cross section data and theory permit estimates of basic imput data for track structure calculations with reasonable accuracy for a few target materials for a restricted energy range, say,0.3-10 MeV/u. Fig. 1.12 (left panel) shows two-dimensional projections of track segments from 1 to 8 MeV α particles in vater vapor, calculated with a code older than PARTRAC (MOCA-14) [11].

All primary and secondary inelastic events are symbolized by a dot, through

26
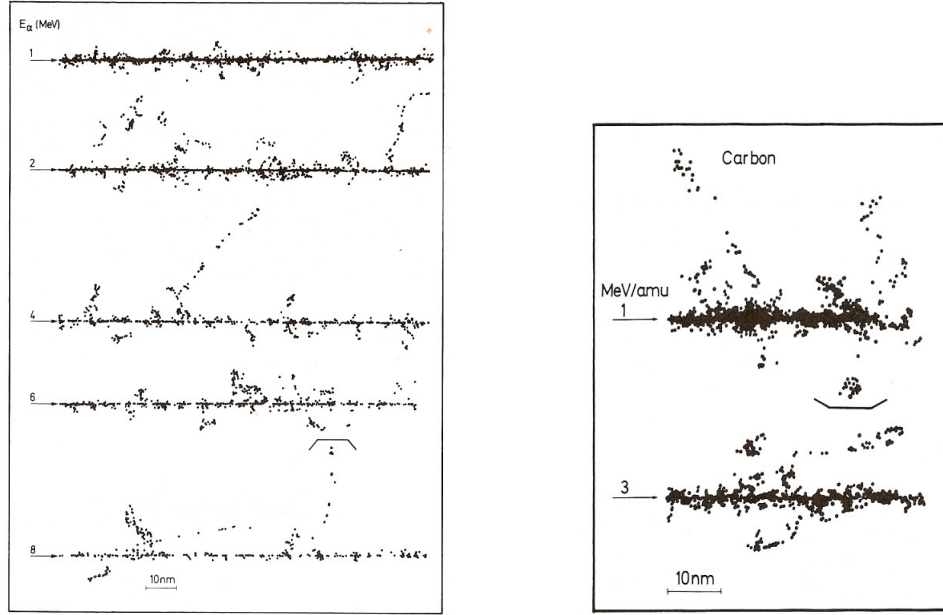
Figure 1.12: *Left*: Calculated α particle track segment (1, 2, 4, 6, and 8 MeV) in water (MOCA-14)[11]; *Right*: Track segments of 1- and 3 MeV/u carbon ionsin water (MOCA-14) scaled from proton tracks of the same velocity by multiplication of primary electron ejection cross sections by the effective charge squared (see Barkas formula) [11].

the full informationon their physical and chemical nature are avaliable in the code as output of the physical end chemical modules (see Chapter 4). The higher density of events stems from the Z^2 dependence of all ion cross sections. The electron transport, however, is independent of the charge of the ejecting ion. Because of the Z^2 dependence of the primary cross sections, higher energy secondary electron tracks are also visible per unit track lenght for α particles than for protons.

In these computed α particle tracks one can see the transition from the *grain count* (single, separated events along the ion path) regime at high particle energies to the *track width* (overlapping events on and close the ion path) regime at lower energies. This can lead to different types of radiation actions as we will discuss in the Chapter dedicated to DNA radiation damage in the cell nucleus.

Presently is still very difficult to perform reliable track structure calculations for ions heavier than α particles because of the lack of comprehensive experimental absolute cross sections and the lack of accurate enough theories. As mentioned above the existence of loosely bound electrons in the projectile is the main reason of this problem. However, to give a semiquantitative example, track structure of fast Carbon ions were derived from proton tracks by multiplying all primary ion cross sections with the velocity dipendent effective charge squared $[Z^*(\beta)]^2$ as calculated from Barkas's formula. Fig. 1.12 (right panel) gives an idea of such heavy ion tracks.

Another problem is the comprehension of the collective response of liquid water used as principal target in radiobiological studies. Next Section gives a qualitative description of differences between water vapor and water in liquid phase.

27

The next Chapter will illustrate in a more detailed way the calculation of such cross sections taking into consideration the collective behaviour of water molecules under irradiation of heavy charged particles.

1.5 Differences between liquid and gas phase
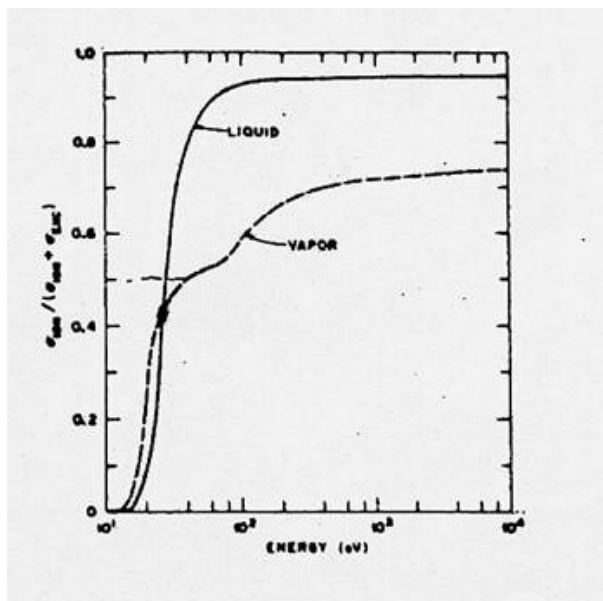
Figure 1.13: Relative contribution of excitations and ionization as a function of incident electron energy. Comparison between simulation results of electron track in water vapor and liquid water [13].

In the codes that simulate the interaction between radiation and biological targets, water is choosen as the medium in which radiation transport takes place, being the primary constituent of living organisms. Electron and other radiation interactions can be described by cross sections calculated for water in vapor phase or in liquid phase. In the most recent versions of the PARTRAC code used in this work, the liquid phase has ben choosen because it describes in a better way the real biological target. The two main characteristics that distinguish energy deposition in liquid and gas phase are

- the relative importance of ionizations and excitations is different (see Fig. 1.13). In liquid phase there is a major ionizations contribution above 50 eV. In particular the minimal energy for ionization is about 8 eV for liquid phase, while the value for water vapour is 12.6 eV and the mean energy for ion pair formation is about 30 eV/ip (eV per ion pair produced) for vapor while is 20 eV/ip for liquid;

- the presence in the liquid phase of collective phenomena which extend the effect of a local energy deposition to neighbor molecules can involve a large number of electrons ($\sim 10^9$) at a distance of the order of some nanometers.
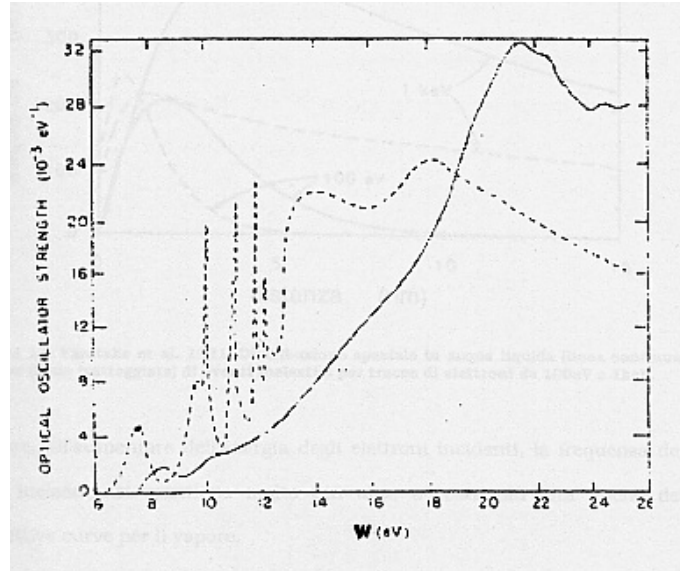
Figure 1.14: Optical oscillator strength of liquid water (continuous line) and water vapor (dashed line) as a function of incident electron energy [14].

In Fig. 1.14 are depicted the the optical oscillator strengths of water vapour and liquid water. While in the case of water vapour (dashed line) the peaks in correspondence of the excited states of the single molecule are evident, in the case of liquid water (continuous line) a continuous and gradual absorption is privileged and is characterized by a shift of the maximum values to higher energies. This is due to the strong binding between neighbour water molecules, which in liquid water behave like a lattice favouring a collective response.

29

Interaction of charged particles in condensed matter

Charged particle track-structure analysis is a useful basis for understanding the early physical and chemical stages of radiation action on matter in general. This holds especially in radiation biology, i.e. in research on the effects of radiation on the cell, which has a highly inhomogeneous spatial and chemical structure. Track structure analysis based on computer simulations requires as input data cross sections for the interactions of electrons (primary or secondary) and other charged particles with molecules in the matter under consideration. In the cell soft tissue, water is the dominant component, and it is largely in the liquid state.

These kinds of simulations use the classical trajectory picture and follow the incident particle, as well as all produced secondary particles, from starting to ejection energies down to total stopping, by experiencing elastic and inelastic events. However, because of the scarcity of experimental and theoretical knowledge on the details of the molecular, chemical consequences of energy transferred in inelastic collisions, earlier track structure calculations for radiation biophysics have been using water in the vapor state as a model substance. More recent Monte Carlo simulation codes like the PARTRAC code used in this work, use liquid water as a model substance for soft tissues. The use of liquid water requires detailed cross sections as input data which take into consideration the collective response of condensed matter, that is the liquid phase.

Because of the intrinsic difficulties of obtaining detailed cross sections for inelastic interactions by charged particles in condensed phase matter, all of our information on such cross sections must be determined from appropriate theory. The conventional theory used to describe inelastic processes such as excitation and ionization of matter, is based on the (*plane wave*) *first Born approximation*[1] (BA) and the *dielectric theory*. The first is a perturbative treatment that is expected

---

[1] This assumption allows the description of the incoming particle as a plane wave, i.e. a free particle. See for example S. Boffi, *Da Laplace ad Heisenberg - Un'introduzione alla meccanica quantistica e alle sue applicazioni*, Ed. La Goliardica Pavese, 1992, p. 496.

to be valid only for sufficiently fast projectiles, with velocities much larger than the orbital velocities of the atomic electrons. The latter is used to describe all the information of the condensed medium and its collective response to external perturbation. The dielectric theory of inelastic processes will be the main part of the next Sections where we will show how to obtain, starting for first principles, the general formula for the inelastic cross section in condensed phase matter.

2.1   Dielectric theory for inelastic scattering

In this theoretical framework, we will show that the general structure of expressions such as cross section for a process in which a fast particle transfers a given amount of energy and momentum can be expressed by two distinct factors, one dealing *with the incident particle only* and the other one with *the target only.* The first factor is nearly trivial; the second, the *dynamic form factor* of the medium, constitutes the central object of study in this Section. The dynamic form factor is directly related to the dielectric properties of the medium, that is to the (complex) *dielectric response function* (DF) of the medium by which it is possible to express quantities such as cross sections or stopping power. The framework of these calculation is commonly called the *dielectric theory of inelastic scattering processes* [20]. In the BA approximation, that is for sufficiently fast collisions[2] the influence of the incident particle upon an atom or molecule that constitute the medium may be regarded as a sudden and small external perturbation and the applicability of perturbation theory is justified.

2.1.1   Response of a system to a time-dependent perturbative potential

In order to introduce the dielectric theory of inelastic processes, we need to recall some basic concepts and formuls from Quantum Mechanics and Perturbation Theory.

The majority of the macro- and microscopic properties of a quantum system can be related to the following general problem: an external perturbation varying in both space and time is imposed on the system (e.g., an electric field, magnetic field, or, most important in this context, the passage of a charged particle), and we ask what the response is to this perturbation (electric polarization and current, magnetization, etc). For a weak perturbative potential H_1, the response is in general *linear*, that is proportional to H_1.

Let us therefore consider the general case where a system, with Hamiltonian H_0 that includes the interaction between the particles of the system (for example the interaction of the electrons in a molecule). Let us apply to it a perturbation whose intensity varies with time, characterized by an interaction potential $AF(t)$.

---

[2]We restrict ourselves to the theoretical treatment of fast collision relatively to the context of this work, that is fast charged particle but still in the nonrelativistic regime.

The operator A which operates on the wave function of the system is hermitian. Its time dependence is absorbed completely in the real scalar factor $F(t)$. The wave function $|\varphi_s(t)\rangle$ satisfies the Schroedinger equation

$$i\frac{\partial|\varphi_s(t)\rangle}{\partial t} = (H_0 + AF(t))|\varphi_s(t)\rangle \tag{2.1}$$

(where we have taken units such that $\hbar = 1$). In order to completely define $|\varphi_s(t)\rangle$, it is sufficient to impose one boundary condition: we shall assume that, for $t = -\infty$, $F(t) = 0$, the system being in its ground state $|\varphi_{s0}\rangle$.

Until now we have used the Shroedinger representation, in which the operators A, H_0, ... are independent of time. It is convenient to switch to the Heisenberg representation defined by the transformation

$$|\varphi(t)\rangle = e^{iH_0t}|\varphi_s(t)\rangle$$

In order to retain the same average values, it is simultaneously necessary to modify the definition of operators, which becomes

$$\mathbf{A}(t) = e^{iH_0t}Ae^{-iH_0t}$$

After the transformation, Eq. (2.1) is written as

$$i\frac{\partial|\varphi\rangle}{\partial t} = \mathbf{A}(t)F(t)|\varphi\rangle \tag{2.2}$$

The *response* of the system is nothing more than the average value of a certain operator B, which can be current, magnetic moment, etc. Thus we want to calculate

$$\langle\varphi|\mathbf{B}(t)|\varphi\rangle = \langle B\rangle$$

Now, since we are limiting ourselves to a linear response (*weak perturbation*), it is sufficient to calculate $|\varphi\rangle$ to first order in A by perturbative calculation. Let us write $|\varphi\rangle$ in the form of an expansion

$$|\varphi\rangle = |\varphi_0\rangle + |\varphi_1\rangle + ...$$

We see at once that

$$i\frac{\partial|\varphi_1\rangle}{\partial t} = \mathbf{A}(t)F(t)|\varphi_0\rangle$$

This equation is easily integrated because of the boundary condition indicated above, and the result is

$$|\varphi_1\rangle = -i\int_{-\infty}^{t}dt'\,\mathbf{A}(t')F(t')|\varphi_0\rangle \tag{2.3}$$

where $|\varphi_0\rangle$ is independent of time because of the choice of representation. To the first order, $\langle B\rangle$ is given by

$$\langle B \rangle = B_0 + \langle \varphi_0 | \mathbf{B}(t) | \varphi_1 \rangle + \langle \varphi_1 | \mathbf{B}(t) | \varphi_0 \rangle \tag{2.4}$$

where B_0 is the average value of B in the ground state $|\varphi_0\rangle$. Inserting (2.3) in (2.4) we obtain the final expression for $\langle B \rangle$

$$\langle B \rangle - B_0 = i \int_{-\infty}^{t} dt' F(t') \langle \varphi_0 | [\mathbf{A}(t'), \mathbf{B}(t')] | \varphi_0 \rangle \tag{2.5}$$

2.1.2 The response function of the system

If the perturbation is reduced to an impulse given to the system at time $t = 0$, that is to say $F(t) = \delta(t)$, the response becomes

$$\langle B \rangle - B_0 = \varphi_{AB}(t) = \begin{cases} 0 & \text{for } t < 0 \\ i \langle \varphi_0 | [\mathbf{A}, \mathbf{B}(t)] | \varphi_0 \rangle & \text{for } t > 0 \end{cases} \tag{2.6}$$

The quantity $\varphi_{AB}(t)$ is called the *response function* of the system: it describes the response at a time t after the excitation impulse. Let us remark that φ_{AB} is zero for $t < 0$, which is in conformity with the principle of causality. We see that φ_{AB} is completely determined if the commutator $[\mathbf{A}, \mathbf{B}(t')]$ is known. Note that every function can be considered as a succession of impulses, of appropriate chosen amplitude. More precisely, we have

$$F(t) = \int_{-\infty}^{+\infty} dt' \delta(t - t') F(t')$$

Since the response of the system is linear, in order to obtain the response to the excitation $AF(t)$ it is sufficient to add the responses to each of the elementary impulses,

$$\langle B \rangle - B_0 = \int_{-\infty}^{+\infty} dt' \varphi_{AB}(t - t') F(t') \tag{2.7}$$

and inserting (2.7) into the expression (2.6) for $\varphi_{AB}(t)$, remarking that $\langle \varphi_0 | [\mathbf{A}(t'), \mathbf{B}(t)] | \varphi_0 \rangle$ depends only on $t - t'$, we recover (2.5).

2.1.3 Response to a periodic excitation

Every function $F(t)$ can be expanded in Fourier series

$$F(t) = \frac{1}{2\pi} \int_{-\infty}^{+\infty} d\omega e^{(-i\omega + \eta)t} F(\omega)$$

As $F(t)$ is a real function, we deduce that $F(-\omega) = [F(\omega)]^*$. Since we have limited ourselves to linear effects, we shall obtain the total response by adding the responses to each Fourier component. This lead us to study the perturbation

$$F(t) = e^{(-i\omega + \eta)t}$$

(which makes sense physically only if we combine it with its complex conjugate of frequency $-\omega$). By putting this expression in Eq. (2.7), we obtain

$$\begin{cases} \langle B \rangle - B_0 = \chi_{AB}(\omega) \exp\left[(-i\omega + \eta)\,t\right] \\ \chi_{AB}(\omega) = \int_0^\infty dt' \varphi_{AB}(t') \exp\left[(-i\omega + \eta)\,t'\right] \end{cases} \tag{2.8}$$

where $\chi_{AB}(\omega)$ is a complex quantity whose modulus and argument describe, respectively, the amplitude and the phase of the response.

Since we assumed B Hermitian, $\langle B \rangle$ must be real, so

$$\chi_{AB}(\omega) = \left[\chi_{AB}(-\omega)\right]^*$$

and $\chi_{AB}(\omega)$ is called *admittance* of the system.

Physical examples of admittance are numerous, but the most involved in this context is the dielectric constant.

We know in general that these quantities depend on frequency: we therefore say that the system is dispersive. It is easy to express the response to any perturbation $F(t)$ whatsoever by means of the admittance $\chi_{AB}(\omega)$. We have

$$\langle B \rangle - B_0 = \frac{1}{2\pi} \int_{-\infty}^{+\infty} d\omega \exp\left[(-i\omega + \eta)\,t\right] F(\omega)\,\chi_{AB}(\omega)$$

Now we want to explicit the quantities $\varphi_{AB}(t)$ and $\chi_{AB}(\omega)$. We utilize for this the complete set of eigenfunctions $|\varphi_n\rangle$ of the isolated system Hamiltonian H_0, of energy E_n. In order to simplify the writings we put

$$E_n - E_0 = \omega_{n0}$$

$$\langle \varphi_0 | A | \varphi_n \rangle = A_{0n}$$

A glance at (2.6) shows that

$$\varphi_{AB}(t) = \begin{cases} 0 & \text{for } t < 0 \\ i \sum_n \left[A_{0n} B_{n0} \exp(i\omega_{n0}t) - B_{0n} A_{n0} \exp(-i\omega_{n0}t)\right] & \text{for } t > 0 \end{cases} \tag{2.9}$$

and from Eq. (2.9) we see that $\varphi_{AB}(t)$ is a real function. Inserting (2.9) into (2.8), we obtain

$$\chi_{AB}(\omega) = \sum_n \left\{ \frac{B_{0n} A_{n0}}{\omega - \omega_{n0} + i\eta} - \frac{A_{0n} B_{n0}}{\omega + \omega_{n0} + i\eta} \right\} \tag{2.10}$$

where we can see that $\chi_{AB}(\omega)$ is an analytic function of ω in the upper-half plane. When $\omega \to \infty$ the expression for $\chi_{AB}(\omega)$ becomes very simple

$$\lim_{\omega \to \infty} \chi_{AB}(\omega) = \frac{1}{\omega} \langle \varphi_0 | [B, A] | \varphi_0 \rangle \tag{2.11}$$

2.1.4 An example: the dielectric constant of an electron gas

To illustrate the preceding discussion, we shall develop an example that will be necessary for the introduction of some important physical quantities for the study of scattering processes in condensed matter: the longitudinal dielectric constant of a gas of particles that carry an electric charge e.

Let us introduce into this system of charged particles an eleciric charge distribution playing the role of a perturbation. To simplify, we suppose these charges to be periodic in time (frequency ω) and in space (wave vector $\mathbf{q}$). The density of charge introduced is written as

$$Q\left(\mathbf{r}, t\right) = er_q \cos\left(\mathbf{q} \cdot \mathbf{r}\right) \cos\left(\omega t\right)$$

where r_q is a real number sufficiently small so that the response remains linear. This distribution produces a longitudinal electric field equal to

$$\mathbf{E}\left(\mathbf{r}, t\right) = \frac{4\pi e\mathbf{q}}{q^2} r_q \sin\left(\mathbf{q} \cdot \mathbf{r}\right) \cos\left(\omega t\right) \tag{2.12}$$

Under the influence of this electric field, the distribution of electrons readjusts itself in such a way to screen the charges introduced. It is this shielding effect that we wish to study.

The vector defined by (2.12) is in fact the electric displacement $\mathbf{D}$. The local electric field $\mathbf{E}_L$ is given by Poisson's equation

$$\nabla \cdot \mathbf{E}_L = 4\pi\left(Q + Q_e\right)$$

where Q_e is the density of electronic charge resulting from polarization of the medium (we assume that at the equilibrium the system is neutral, the charge of the electrons being compensated by a uniform positive charge). In general, Q_e is out of phase with Q. In order to take into account this dephasing, we resort to the usual artifice, and we study the response to the fictious perturbation

$$Q\left(\omega\right) = er_q \cos\left(\mathbf{q} \cdot \mathbf{r}\right) \exp\left(-i\omega t\right)$$

The dielectric constant $\varepsilon\left(\mathbf{q}, \omega\right)$ is then defined by

$$\varepsilon\left(\mathbf{q}, \omega\right) = \frac{D\left(\omega\right)}{E_L\left(\omega\right)} = \frac{Q\left(\omega\right)}{Q\left(\omega\right) + Q_e\left(\omega\right)}$$

which we can rewrite in the following form

$$\frac{1}{\varepsilon\left(\mathbf{q}, \omega\right)} - 1 = \frac{Q_e\left(\omega\right)}{Q\left(\omega\right)}$$

and Q_e is equal to the average value of the operator $e\rho\left(\mathbf{r}\right)$, where $\rho\left(\mathbf{r}\right)$ is the density of electrons at the point $\mathbf{r}$,

$$\rho\left(\mathbf{r}\right) = \sum_i \delta\left(\mathbf{r} - \mathbf{r}_i\right)$$

($\mathbf{r}_i$ being the position of the ith electron). It is convenient to express $\rho\left(\mathbf{r}\right)$ in terms of its Fourier components

$$\rho_{\mathbf{q}} = \int d^3 r \exp\left(-i\mathbf{q} \cdot \mathbf{r}\right) \rho\left(\mathbf{r}\right) = \sum_i \exp\left(-i\mathbf{q} \cdot \mathbf{r}_i\right)$$

For this purpose, let us enclose the system in a box of volume Ω, so as to quantize the values of $\mathbf{q}$. It is easy to verify that

$$\delta\left(\mathbf{r} - \mathbf{r}_i\right) = \frac{1}{\Omega} \sum_{\mathbf{q}'} \exp\left[-i\mathbf{q}' \cdot \left(\mathbf{r} - \mathbf{r}_i\right)\right]$$

It follows that Q_e can be written as

$$Q_e = \frac{e}{\Omega} \sum_{\mathbf{q}'} \langle \rho_{\mathbf{q}'} \rangle \exp\left(i\mathbf{q}' \cdot \mathbf{r}\right)$$

Let us limit ourselves to a homogeneous and isotropic system: it is clear that the polarization is going to contain the same factor $\cos\left(\mathbf{q} \cdot \mathbf{r}\right)$ as the external charge. Consequently only the Fourier components $\mathbf{q}' = \pm\mathbf{q}$ will contribute to Q_e. We can therefore write

$$\begin{cases} Q_e = \frac{2e}{\Omega} \langle \rho_{\mathbf{q}} \rangle \cos\left(\mathbf{q} \cdot \mathbf{r}\right) \\ \langle \rho_{\mathbf{q}} \rangle = \langle \rho_{-\mathbf{q}} \rangle \end{cases}$$

The above formula makes possible to simplify the definition of $\varepsilon\left(\mathbf{q}, \omega\right)$, which becomes

$$\frac{1}{\varepsilon} - 1 = \frac{2\langle \rho_{\mathbf{q}} \rangle}{\Omega r_q \exp\left(-i\omega t\right)} \tag{2.13}$$

We are thus led to the calculation of the average value of $\rho_{\mathbf{q}}$ in the presence of perturbation. In order to apply the results of the preceding Section, we need the interaction Hamiltonian between the electrons and the external charges. The latter creates at each point an electrostatic potential

$$V\left(\mathbf{r}, t\right) = \frac{4\pi e^2}{q^2} r_q \cos\left(\mathbf{q} \cdot \mathbf{r}\right) \exp\left(-i\omega t\right)$$

The interaction energy can be written as

$$\sum_i eV\left(\mathbf{r}_i, t\right)$$

By returning to the definition of $\rho_{\mathbf{q}}$ given above, we see that the operator A defined in Subsection 2.1.3 is in this case equal to

$$A = \frac{4\pi e^2}{q^2} \frac{r_q}{2} \left(\rho_{\mathbf{q}} + \rho_{-\mathbf{q}} \right)$$

We are now ready to apply the general formulas (2.8). In the expression for $\varphi_{AB}(t)$, the commutator $[\rho_{\mathbf{q}}, \rho_{\mathbf{q}}(t)]$ has an average value of zero for obvious reasons of translational invariance. Only the term $\rho_{-\mathbf{q}}$ in A contributes. Under these conditions, Eqs. (2.8) and (2.10) give us

$$\langle \rho_{\mathbf{q}} \rangle = \frac{4\pi e^2}{q^2} \frac{r_q}{2} \exp\left(-i\omega t\right) \sum_n \left\{ \frac{|(\rho_{\mathbf{q}})_{0n}|^2}{\omega - \omega_{no} + i\eta} - \frac{|(\rho_{-\mathbf{q}})_{0n}|^2}{\omega + \omega_{no} + i\eta} \right\}$$

We can simplify the above expression by noticing that, for symmetry reasons, to each state n of the first term of it there corresponds a state m of the second term, obtained by reflection, such that

$$\begin{cases} |(\rho_{\mathbf{q}})_{0n}|^2 = |(\rho_{-\mathbf{q}})_{0m}|^2 \\ \omega_{n0} = \omega_{m0} \end{cases}$$

We can therefore write

$$\langle \rho_{\mathbf{q}} \rangle = \frac{4\pi e^2}{q^2} \frac{r_q}{2} \exp\left(-i\omega t\right) \sum_n |(\rho_{\mathbf{q}})_{0n}|^2 \frac{2\omega_{n0}}{(\omega - \omega_{no} + i\eta)(\omega + \omega_{no} + i\eta)} \qquad (2.14)$$

(and at the same time, this discussion shows that $\langle \rho_{\mathbf{q}} \rangle = \langle \rho_{-\mathbf{q}} \rangle$). By comparing this result with the definition (2.13) we finally obtain the following expression for the dielectric constant

$$\frac{1}{\varepsilon(\mathbf{q}, \omega)} - 1 = \frac{4\pi e^2}{\Omega q^2} \sum_n \frac{2\omega_{n0}|(\rho_{\mathbf{q}})_{0n}|^2}{(\omega + i\eta)^2 - \omega_{n0}^2} \qquad (2.15)$$

which can also be written in an extended form as

$$\frac{1}{\varepsilon(\mathbf{q}, \omega)} = 1 + \frac{4\pi e^2}{\Omega q^2} \sum_n |(\rho_{\mathbf{q}})_{0n}|^2 \left\{ \frac{1}{\omega - \omega_{no} + i\eta} - \frac{1}{\omega + \omega_{no} + i\eta} \right\}$$

In order to separate the real and imaginary part of $1/\varepsilon$, we remark that

$$\lim_{\eta \to 0} \frac{1}{\omega \pm i\eta} = \wp\left(\frac{1}{\omega}\right) \mp i\pi\delta(\omega)$$

Upon comparison with (2.15) we obtain

$$\begin{cases} \Re e\left(\frac{1}{\varepsilon(\mathbf{q}, \omega)}\right) = 1 + \frac{4\pi e^2}{\Omega q^2} \sum_n 2\omega_{no} |(\rho_{\mathbf{q}})_{0n}|^2 \wp\left(\frac{1}{\omega^2 - \omega_{mo}^2}\right) \\ \Im m\left(\frac{1}{\varepsilon(\mathbf{q}, \omega)}\right) = \frac{4i\pi e^2}{\Omega q^2} \sum_n |(\rho_{\mathbf{q}})_{0n}|^2 \left[\delta(\omega + \omega_{n0}) - \delta(\omega - \omega_{n0})\right] \end{cases} \qquad (2.16)$$

The functions $\Re e\,(1/\varepsilon)$ and $\Im m\,(1/\varepsilon)$ are, respectively, even and odd function of ω. The real part of $1/\varepsilon$ corresponds to an introduced charge in phase with Q, that is to say, to a current of electrons $\pi/2$ out of phase with the electric field: we thus have polarization current, purely reactive, not giving rise to any transfer of energy. On the other hand, $\Im m\,(1/\varepsilon)$ corresponds to a current of electrons in phase with the electric field. The presence of the Dirac delta function in $\Im m\,(1/\varepsilon)$ furthermore shows directly that this term describes real transitions, for which the energy of the system varies by $\pm\hbar\omega$.

When $\omega \to \infty$, $(1/\varepsilon) - 1$ is of order $1/\omega^2$. Its limiting value is given by Eq. (2.11), which is written here

$$\frac{1}{\varepsilon} - 1 \to -\frac{4\pi e^2}{\Omega q^2} \langle\varphi_0|\,[[H_0, \rho_{-\mathbf{q}}]\,, \rho_{\mathbf{q}}]\,|\varphi_0\rangle \tag{2.17}$$

This commutator can be calculated explicitly if we assume that the law of interaction between particles of the system depends only on the distance between them. We can then write

$$H_0 = \sum_i \frac{\mathbf{p}_i^2}{2m} + \frac{1}{2}\sum_{i\neq j} V\,(\mathbf{r}_i-\mathbf{r}_j)$$

(where m is the mass of an electron). The operator $\rho_{\mathbf{q}}$ commutes with V: the only contribution arises from the kinetic energy, which gives

$$[H_0, \rho_{-\mathbf{q}}] = \sum_i \left(-\frac{\mathbf{q}\cdot\mathbf{p}_i}{m} + \frac{\mathbf{q}^2}{2m}\right)\exp\,(i\mathbf{q}\cdot\mathbf{r}_i)$$

$$[[H_0, \rho_{-\mathbf{q}}]\,, \rho_{\mathbf{q}}] = \sum_i \left(\frac{-\mathbf{q}^2}{m}\right) = -\frac{N\mathbf{q}^2}{m}$$

where N is the total number of electrons. Eq. (2.17) is therefore written as

$$\frac{1}{\varepsilon} - 1 \to \frac{4\pi N e^2}{m\Omega\omega^2}$$

In other words, at high frequencies, the response of the system becomes independent of the law of interaction. Only the inertia of electrons and their density N/Ω come into play.

2.1.5 Inelastic scattering processes: differential cross section and *the dynamic form factor*

In the preceding Section we studied the response of the system to a macroscopic excitation. Now, to prepare us to the study of charged particle interaction in condensed matter, we deal with the most interesting case (in the context of this work) that is the excitation of the system by a beam of fast incident particles[3].

---

[3]In the context of this work, we shall limit ourselves exclusively to problems which can be treated within the first Born approximation.

Let us consider an incident particle, of mass M. Let us assume that it interacts with each of the particles of the system through a potential $V(r)$ depending uniquely on the distance separating them (as in the case of a charged incoming particle via Coulomb interaction). The Hamiltonian of the system plus particle can be written as

$$H = H_0 + \frac{\mathbf{P}^2}{2M} + \sum_i V(\mathbf{R} - \mathbf{r}_i)$$

where $\mathbf{R}$ and $\mathbf{P}$ are the position and momentum of the incident particle. It is convenient to expand the potential in a Fourier series, which gives

$$H = H_0 + \frac{P^2}{2M} + \sum_{\mathbf{q}} \frac{V_{\mathbf{q}} \exp(i\mathbf{q} \cdot \mathbf{R})}{\Omega} \rho_{\mathbf{q}}$$

where the component $V_{\mathbf{q}}$ is defined by

$$V_{\mathbf{q}} = \int d^3 R \exp(i\mathbf{q} \cdot \mathbf{R}) V(\mathbf{R})$$

A typical collision will have the effect of making the system go from its ground state $|\varphi_0\rangle$ to the excited state $|\varphi_n\rangle$, that is a *transition*, and the incident particle from the state with $\mathbf{P}_0$ to the state with $(\mathbf{P}_0 - \mathbf{q})$ (this means an energy loss by the particle with an amount of energy equal to that necessary for the transition of the system). Thus there is transferred to the system an energy $\omega = \omega_{n0}$ and a momentum $\mathbf{q}$. The particle is deflected through an angle θ, in the direction indicated by Fig. 2.1.
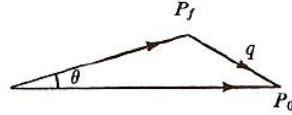
Figure 2.1: Geometry of momentum vectors.

According to the *golden rule*, the *probability per unit time* that a certain collision takes place is given by

$$W_{nq} = 2\pi \frac{|V_{\mathbf{q}}|^2}{\Omega^2} |(\rho_{\mathbf{q}})_{0n}|^2 \delta\left(\omega_{n0} + \frac{q^2}{2M} - \frac{\mathbf{q} \cdot \mathbf{P}_0}{M}\right) \tag{2.18}$$

In practice we are interested only in the final state of the incident particle. The *total probability* (per unit time) that the latter will go into the state with momentum $\mathbf{P_0} - \mathbf{q}$ is

$$W_{\mathbf{q}} = \sum_n W_{n\mathbf{q}}$$

40

In general, experimental results are expressed in terms of a doubly differential cross section $d^2\sigma/d\gamma d\omega$ for scattering into the solid angle $d\gamma$ with an energy transfer of an amount between ω and $\omega + d\omega$. These conditions restrict the momentum transfer $\mathbf{q}$ to the shaded region in Fig. 2.2.
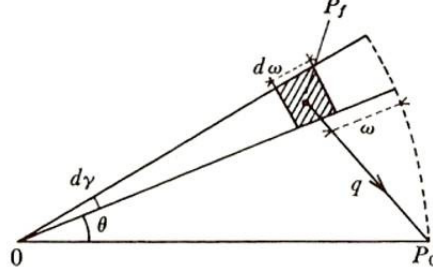
Figure 2.2: Region of restriction for momentum transfer $\mathbf{q}$.

To obtain the (doubly) *differential cross section*, it is sufficient to sum $W_{\mathbf{q}}$ over the value of $\mathbf{q}$ included in this region.
We thus find

$$\frac{d^2\sigma}{d\gamma d\omega} = \left(\frac{\Omega M}{P_0}\right)\frac{d^2 W}{d\gamma d\omega} = \frac{M^2\Omega^2}{(2\pi)^3}\frac{P_f}{P_0}\cdot W_{\mathbf{q}} \qquad (2.19)$$

where P_f is the magnitude of the final momentum.
By combining Eq. (2.18) and (2.19), we see that we can write the differential cross section[4] in the form

$$\frac{d^2\sigma}{d\gamma d\omega} = A S(\mathbf{q},\omega) \qquad (2.20)$$

where the factors A and S are defined as follows

$$A = \frac{M^2\Omega}{8\pi^3}\frac{P_f}{P_0}|V_{\mathbf{q}}|^2 \qquad (2.21)$$

and

$$S(\mathbf{q},\omega) = \sum_n |(\rho_{\mathbf{q}})_{0n}|^2\delta(\omega_{n0}-\omega)\frac{2\pi}{\Omega} \qquad (2.22)$$

The value of $\mathbf{q}$ is known once the direction γ and the frequency ω have been fixed (see Fig. 2.2). The factor A contains all the elements relative to the incident particle: mass, initial and final momentum, law of interaction with the system. Conversely, S is entirely characteristic of the system itself and it is called the *dynamic form factor*. If the particle is changed, S remains the same; only A varies. We thus see the great generality of Eqs. (2.21) and (2.22): it is sufficient to study

---

[4]We will return on this formula, expressed in a different form through the macroscopic cross section Σ, in Section 2.4 when dealing with electron and proton cross sections.

the function $S(\mathbf{q}, \omega)$ once to describe the scattering in the Born approximation for any particle whatsoever.

When we know the energy of the scattered particles, we obtain directly the cross section $d^2\sigma/d\gamma d\omega$ and the formula (2.19) can be applied without further comments. Actually, we are often obliged to limit ourselves to a measurement of $d\sigma/d\gamma$, without determination of energy. Then it is necessary to integrate (2.20) over ω. In general this is not a simple operation, for $\mathbf{q}$ depends on ω. If, however, the velocity of the incident particle is raised (but remaining in the regime of applicability of the Born approximation), so that

$$\frac{|\mathbf{q}|P_0}{M} \gg \langle \omega_{n0} \rangle \tag{2.23}$$

the problem is considerably simplified. In fact, in this case, conservation of energy requires $\mathbf{q}$ to be practically perpendicular to $\mathbf{P}_0$, the angle of deflection θ remaining small. Under these conditions, q is practically independent of ω, and we can write

$$\frac{d\sigma}{d\gamma} = A \int_{-\infty}^{+\infty} d\omega S(\mathbf{q}, \omega) = 2\pi A S(\mathbf{q}) \tag{2.49}$$

valid if (2.23) is true. The function $S(\mathbf{q}, \omega)$ is real; it is zero for negative values of ω. Let us calculate its Fourier transform with respect to ω,

$$S(\mathbf{q}, t) = \frac{1}{2\pi} \int_{-\infty}^{+\infty} d\omega \exp(-i\omega t) S(\mathbf{q}, \omega)$$

By comparison with (2.2) we see that

$$S(\mathbf{q}, t) = \frac{1}{\Omega} \sum_n |(\rho_\mathbf{q})_{0n}|^2 \exp(-i\omega_{n0}t) = \frac{1}{\Omega} \langle \varphi_0 | \rho_\mathbf{q}(t) \rho_{-\mathbf{q}} | \varphi_0 \rangle$$

(we adopt Heisenberg picture for the isolated system). In this expression the resemblance between S and the admittance defined above becomes evident. We shall return on this expression later.

Let us now take the Fourier transform with respect to $\mathbf{q}$, by defining

$$S(\mathbf{r}, t) = \frac{1}{\Omega} \sum_\mathbf{q} S(\mathbf{q}, t) \exp(i\mathbf{q} \cdot r)$$

Let us return to the definition of $\rho_\mathbf{q}$. We can write

$$S(\mathbf{r}, t) = \frac{1}{\Omega^2} \sum_\mathbf{q} \int d^3 r' \int d^3 r'' \exp[i\mathbf{q} \cdot (\mathbf{r} - \mathbf{r}' + \mathbf{r}'')] \langle \varphi_0 | \rho(\mathbf{r}', t) \rho(\mathbf{r}'', 0) | \varphi_0 \rangle$$

The summation over $\mathbf{q}$ is simple - it gives a $\delta-$function - and we finally obtain

$$S(\mathbf{r}, t) = \frac{1}{\Omega} \int d^3 r' \langle \varphi_0 | \rho(\mathbf{r}', t) \rho(\mathbf{r}' - \mathbf{r}, 0) | \varphi_0 \rangle \tag{2.25}$$

which, because of translational invariance, can be transformed into

$$S(\mathbf{r}, t) = \langle \varphi_0 | \rho(\mathbf{r}, t) \rho(\mathbf{0}, 0) | \varphi_0 \rangle \tag{2.26}$$

The quantity $S(\mathbf{r}, t)$ is called the *correlation function* between the density at $(\mathbf{r}, t)$ and that at $(\mathbf{0}, 0)$. It is intimately related to the probability of finding a particle at $(\mathbf{r}, t)$ when we know that there is one at $(\mathbf{0}, 0)$, and being a real function we deduce that

$$\begin{cases} S(\mathbf{q}, t) = S(\mathbf{q}, -t)^* \\ S(\mathbf{r}, t) = S(-\mathbf{r}, -t)^* \end{cases}$$

When $\mathbf{r}$ and t tend to infinity, it is obvious that the correlation plays no role. We see from (2.26) that $S(\mathbf{r}, t)$ should tend to the square of the average density,

$$S(\mathbf{r}, t) \to N^2 / \Omega^2 \quad \text{if } \mathbf{r} \text{ or } t \to \infty$$

It is frequently convenient to subtract from $S(\mathbf{r}, t)$ this limiting value by defining

$$S'(\mathbf{r}, t) = S(\mathbf{r}, t) - N^2 / \Omega^2$$

S' tends to zero at infinity and uniquely describes the corrections to S due to the interaction between the particles of the system. The limiting value N^2 / Ω^2 is of no physical interest whatever, as it gives contribution to $S(\mathbf{q}, \omega)$ proportional to $\delta(\omega) \delta(\mathbf{q})$, corresponding to an elastic-scattering process without deflection: such a scattering cannot be separated from the incident beam.

2.1.6 Some properties of the dielectric response function

With the formuls shown above, one may derive a spectral representation of $1/\varepsilon$

$$\frac{1}{\varepsilon(\mathbf{q}, \omega)} = 1 + \frac{4\pi e^2}{\Omega q^2} \int_0^\infty d\omega' S(\mathbf{q}, \omega') \left\{ \frac{1}{\omega - \omega_{no} + i\eta} - \frac{1}{\omega + \omega_{no} + i\eta} \right\}$$

In this way the dynamic form factor $S(\mathbf{q}, \omega)$ thus serves as a spectral density for $1/\varepsilon$.

In conclusion, it remains for us to relate these results to the dielectric constant which we studied in the preceding Section. Let us compare (2.16) and Eq. (2.21) and (2.22). We see that

$$\Im m \left(\frac{1}{\varepsilon(\mathbf{q}, \omega)} \right) = \frac{2\pi i e^2}{q^2} [S(\mathbf{q}, -\omega) - S(\mathbf{q}, \omega)]$$

This relation permits, knowing the properties of $S(\mathbf{q}, \omega)$, with few simple calculations to express[5] the doubly differential cross section $d^2\sigma/d\gamma d\omega$ (Eq. (2.20)) directly in terms of the imaginary part of $1/\varepsilon$.

---

[5]The expression that relates the doubly differential cross section in terms of the imaginary

2.2 Quantum theory of stopping power

Recalling the definition of stopping power given in Chapter 1, to proceed with a detailed calculation we shall adopt the hypothesis of *independent successive pair collisions* of a particle with atoms of the medium. When our medium is a gas, such hypothesis seems quite valid, but the situation, however, is much more complicated if the particle passes through a condensed medium. The limitations of this hypothesis are especially clear when one considers the passage of charged particles through liquid or crystals. So, we shall adopt the hypothes of independent pair collisions as a first approximation, and at the same time we shall consider the medium through which the particle passes to be homogeneous and totally disordered. The succesive step will be the extension of the theory to take into consideration the collective response of the condensed medium. For this case we will describe the theory of stopping power recalling the dielectric theory. To reveal the essence of the elementary interaction processes of a particle with the atoms of a material it is necessary to know the structure of the atom and its characteristics, for istance, the spectrum of its energy levels.
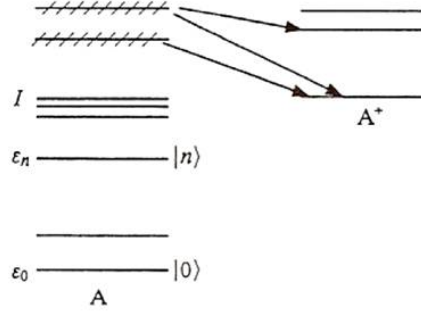
Figure 2.3: Arrangement of discrete and continuous levels of an atom (I is the ionization potential).

Fig. 2.3 presents a schematic picture of such a spectrum. While the excitation energy of the atom is lower than its ionization potential I, the spectrum of atomic levels remains discrete. Then comes the continuous spectrum, within the range of which certain individual spontaneously decaying (autoionization) states are encountered. We shall denote these states pertaining to the discrete spectrum of an atom by the usual notation $|n\rangle$ and write the corresponding wave functions in the form $\varphi_n(\xi) = \varphi_n(r_1\sigma_1, ..., r_z\sigma_z)$, where ξ represents the space and spin variables of all the Z electrons of the atom.

The states $|n\rangle$ are orthonormalized

$$\langle n|n'\rangle = \delta_{nn'} \tag{2.28}$$

part of the dielectric constant will be used in Section 2.4 and will be the starting point for the application to electron and heavy chaged particle (protons and heavy ion) interaction with condensed water.

and together with the states of the continuum they constitute a complete set

$$\sum_n \varphi_n(\xi) \varphi_n^*(\xi') + \ldots = \delta(\xi - \xi') \tag{2.29}$$

(here, the dots stand for the integral over the continuum).
We shall also write the completeness condition (2.29) in the symbolic form

$$\sum_n |n\rangle\langle n| + \ldots = \widehat{I} \tag{2.30}$$

where $\widehat{I}$ is the unit operator in the Hilbert space of atomic states.

Now, consider the passage af a charged particle **a** through a material, and let its mass significantly exceed the electron mass

$$m_a \gg m_e \tag{2.31}$$

From a formal point of view our approach is valid for particles of abitrary charge Z_a, but in the case of multicharge ions $(Z_a \gg 1)$ one should actually take into account a number of special physical processes, which we shall not do for the present (see Subsection 2.4). Thus, we shall assume **a** represents one of the following: a proton p, an α particle, the nuclei of the lightest elements. Generally, when a particle undergoes collision with an atom **A**, various reaction channels may be realized
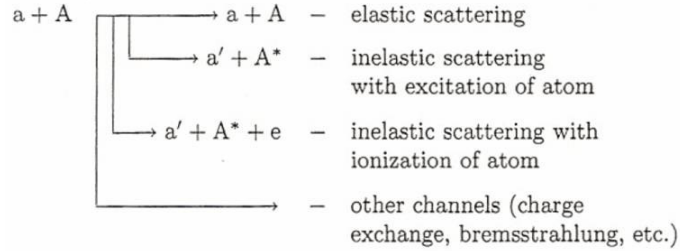
Figure 2.4: Scheme for general reaction channels.

We shall characterize the probability of a collision **a + A** occuring by the *total effective cross section* σ; it is the sum of the total elastic scattering cross section and the total cross section of inelastic processes

$$\sigma = \sigma_{el} + \sigma_{inel} \tag{2.32}$$

We shall call the effective cross sections σ_n of processes **a + A→a' + A$_n^*$**, corresponding to the excitation of some particular levels of the atom, *partial inelastic scattering cross sections*. If charge exchange, bremsstralung, and other less important channels are not taken into account, the total cross section for inelastic processes may be written as

$$\sigma_{inel} = \sum_{n \neq 0} \sigma_n + \ldots \tag{2.33}$$

where the sum over n embraces all the excited discrete levels of the atom, and the dots imply integration over the continuum. We shall further write the relationsip (2.33) [and all relations similar to it, for example, (2.29) or (2.30)] simply in the form

$$\sigma_{inel} = \sum_{n \neq 0} \sigma_n \qquad (2.34)$$

implying summation over n to include, also, integration over the continuum. When it is necessary to distinguish between excitation processes of discrete levels and ionization of the atom, we shall explicitly decompose the inelastic scattering cross section into the respective terms

$$\sigma_{inel} = \sigma_{excit} + \sigma_{ioniz} \qquad (2.35)$$

Having introduced the characteristics of the elementary collision process a + A, we shall go back to our task of expressing the stopping power of a material in terms of these characteristics. Now, consider the passage of particle a through
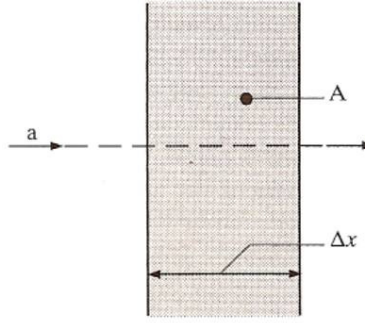
Figure 2.5: Passage of a fast charged particle through a layer Δx of a substance.

a thin material layer consisting of atoms of sort A (Fig. 2.5). According to the adopted hypothesis of independent successive collisions, the ionization losses of the particle equal the sum of losses due to the excitation (ionization) of individual atoms. If a certain collision causes an atom to undergo a transition $|0\rangle \rightarrow |n\rangle$, then each of such collisions results in the particle losing an amount of energy equal to $E_n - E_0$ (strictly speaking, a small amount of the particle's energy is spent on the recoil of the atom as a whole, but this energy can usually be neglected). Consequently, if ΔN_n is the mean number of collisions undergone by the particle with atoms of the material in a layer Δx and resulting in a transition $|0\rangle \rightarrow |n\rangle$, then the mean change in the energy of the particle upon passage through the layer Δx is

$$\Delta E = -\sum_n (\varepsilon_n - \varepsilon_0) \Delta N_n \qquad (2.36)$$

It now remains for us to express ΔN_n in terms of the partial cross sections σ_n (independent of energy)

46

$$\Delta N_n = n_0 \sigma_n \Delta x \tag{2.37}$$

here n_0 is the number of atoms of sort A in a unit volume of the material. Substituting (2.37) into (2.36) and going to the limit $\Delta x \to 0$, we obtain

$$-\frac{dE}{dx} = n_0 \sum_n \left(\varepsilon_n - \varepsilon_0 \right) \sigma_n \tag{2.38}$$

Thus, the stopping power $-dE/dx$ is the product of two factors. One of them, the number n_0 of atoms of sort A per unit volume, is in no way related to the properties and parameters of the particle we are interested in. On the contrary, the other factor is independent of the density of the material but contains all the information concerning the interaction of particles a and A. Its standard notation is

$$S\left(E\right) \equiv \sum_n \left(\varepsilon_n - \varepsilon_0 \right) \sigma_n \tag{2.39}$$

This is the so-called *effective stopping*. According to (2.38) the effective stopping $S(E)$ is the stopping power of a material reduced to the unit density of the number of atoms in the material

$$-\frac{dE}{dx} = n_0 S\left(E\right) \tag{2.40}$$

The stopping represents only one aspect of the passage of a particle through matter. At the same time, each collision event is accompanied by some change in the direction of motion of the particle.

Let us consider how a particle beam initially having a certain direction 'spreads out' due to multiple collisions of each of the beam particles with atoms of the material. We shall introduce two characteristics and, consequently, two different notations: Θ_i, the deviation angle of the particle from the initial direction after the ith collision; ϑ_i the scattering angle resulting from the$i$th collision.

Let $\mathbf{v}_i$ be the velocity vector of the particle after the ith collision (accordingly, $\mathbf{v}_{i-1}$ is the velocity vector before the ith collision, i.e., after the $(i-1)$th collision). All these quantities are shown in Fig. 2.6. Let vector $\mathbf{v}_{i-1}$ lie in the plane of the picture, then vector $\mathbf{v}_i$ will not, generally speaking, be in this plane, and, consequently, its position will be characterized by the azimuthal angle φ_i as well as by the scattering angle ϑ_i.

From geometry it follows that

$$\cos \Theta_i = \cos \Theta_{i-1} \cos \vartheta_i + \sin \Theta_{i-1} \sin \vartheta_i \cos \varphi_i \tag{2.41}$$

Thus, we have expressed the deviation angle of the particle from the initial direction after the ith collision via the deviation angle Θ_{i-1} after the preceding collision, the scattering angle ϑ_i in the ith collision, and the azimuthal angle φ_i corresponding to it.
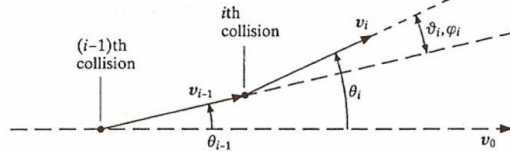
Figure 2.6: Direction of motion of a particle after the $(i-1)$th and ith collisions.

Now, we shall calculate the quantity $\cos\Theta_i$ averaged over a large number of particles passing through the material

$$\langle\cos\Theta_i\rangle = \langle\cos\Theta_{i-1}\cos\vartheta_i\rangle + \langle\sin\Theta_{i-1}\sin\vartheta_i\cos\varphi_i\rangle \tag{2.42}$$

Since, according to the hypothesis of independent successive collisions each collision takes place independently of the preceding one, the medium through which the particle passes is not ordered (i.e., it exhibits no particular directions), the distribution of collisions over the azimuthal angle φ_i is uniform. This means that $\langle\cos\Theta_i\rangle = 0$, i.e., the second term in (2.42) approaches zero, when averaging is performed over a large number of events. A consequence of the same hypothesis of independent pair collisions is that the mean product of the cosines in (2.42) can be replaced by the product of the corresponding mean quantities. As a result we obtain, upon averaging,

$$\langle\cos\Theta_i\rangle = \langle\cos\Theta_{i-1}\rangle\langle\cos\vartheta_i\rangle \tag{2.43}$$

Further, we shall consider only the case of fast heavy particles, in which multiple collisions of the particle with atoms of the medium result in the mean deviation angle being small. Then, taking advantage of the known expansion $\cos x \approx 1 - \frac{1}{2}x^2 + ...$, we obtain, instead of (2.43), the following

$$\langle\Theta_i^2\rangle = \langle\Theta_{i-1}^2\rangle + \langle\vartheta_i^2\rangle \tag{2.44}$$

This recurrent relation shows that the mean square of the particle's deviation angle increases linearly with the average number of collisions

$$\langle\Theta^2\rangle = N\langle\vartheta^2\rangle \tag{2.45}$$

Now, let us once again turn to Fig. 2.6 and formula (2.37). The average number of alI collisions experienced by the particle upon passage through a thin layer of matter of thickness x is

$$N = n_0\sigma x \tag{2.46}$$

where σ is the total effective cross section of its interaction with an atom of the material. Before substituting this expression into $\langle\Theta^2\rangle$, we shall consider the second factor in (2.45) and express the mean square scattering angle $\langle\vartheta^2\rangle$ of the particle scattered from atom in terms of the differential cross section $d\sigma/d\Omega$, which reflects the angular distribution of particles a due to the scattering process

$$\langle \vartheta^2 \rangle = \left(\int d\Omega \vartheta^2 \frac{d\sigma}{d\Omega} \right) / \left(\int d\Omega \frac{d\sigma}{d\Omega} \right) \tag{2.47}$$

The quantity $d\sigma/d\Omega$ present here gives the probability of particle `a` undergoing scattering at an angle ϑ independently of whether the actual collision event turns out to be elastic or inelastic. In other words, the quantity $d\sigma/d\Omega$ occurring in (2.47) is the sum of differential cross sections of elastic and inelastic scattering

$$\frac{d\sigma}{d\Omega} = \left(\frac{d\sigma}{d\Omega} \right)_{el} + \left(\frac{d\sigma}{d\Omega} \right)_{inel} \tag{2.48}$$

Here [see (2.32)]

$$\int d\Omega \frac{d\sigma}{d\Omega} = \sigma \qquad \int d\Omega \left(\frac{d\sigma}{d\Omega} \right)_{el} = \sigma_{el} \qquad \int d\Omega \left(\frac{d\sigma}{d\Omega} \right)_{inel} = \sigma_{inel} \tag{2.49}$$

Thus, by substitution of (2.46) and (2.47) into (2.45) we obtain

$$\langle \Theta^2 \rangle = n_0 x \int d\Omega \vartheta^2 \frac{d\sigma}{d\Omega} \tag{2.50}$$

the mean square deviation angle of a particle (the divergence of the particle beam) increases proportionally with the thickness of the layer of material covered. Relation (2.50) is the main formula of multiple scattering theory for particles passing through matter. Often, the quantity $\Theta = \sqrt{\langle \Theta^2 \rangle}$ is used; it is called the *mean angle of multiple scattering*.

In deriving formulae (2.40) and (2.50) assumptions were made restricting us to considering fast particles [see the arguments presented in obtaining relations (2.36) or (2.44)]. We now have to decide what particles can be considered 'fast'. Apparently, it is necessary that the velocity or kinetic energy of a particle passing through a medium is much greater than some quantity of the corresponding dimensionality characterizing either the medium itself or the interaction of our particle with an atom of the medium.

We shall apply two inequalities.

a) The velocity of particle `a` is much greater than the mean speed of electrons in an atom of the medium

$$v_a \gg \langle v_e \rangle \tag{2.51a}$$

(b) The kinetic energy of particle a is much greater than the average potential energy of an interaction within the system `a + A`

$$E_a \gg |\langle V_{inter} \rangle| \tag{2.51b}$$

Let us estimate what this means in figures, say, in the case of protons interacting with matter. From atomic physics we know that the mean energy of an

electron on the nl orbit of a hydrogen atom or of a hydrogen-like ion is expressed through the Bohr velocity $v_B = \alpha c \approx 2 \times 10^8$ cm/s by the formula

$$\langle v_e \rangle_{nl} = v_B \frac{Z}{n} \tag{2.52}$$

where n is the principal quantum number, Z is the charge of the nucleus, and $\alpha = 1/137$ is the fine structure constant. If applied in the case of a multielectron atom, formula (2.52) can be used only for approximate estimates by substituting the effective charge of the corresponding electron shell Z_{nl}^{eff} for Z; the mean velocity of an electron in an atom depends on the shell it occupies: the farther the electron shell considered is from the nucleus, the lower is the energy of the electron. Often, the Thomas-Fermi model is used for estimation of the electron energy averaged over all the shells of the atom

$$\langle v_e \rangle_{T-F} \approx 0.7 v_B Z^{2/3} \tag{2.53}$$

Consider the example of a proton passing through gaseous helium. In this case, the mean velocity of the electrons in the atom amounts to approximately 0.01 c, and calculations readily reveal that the inequality $E_p \gg 50$ keV corresponds to conditions (2.51). Thus, according to condition (2.51a), protons having kinetic energies of several MeV may surely be considered fast in a helium medium, so the above results can be applied in such a case.

In this Section, our task will now consist in finding the characteristics of the particle's interaction with the atoms of the medium: the effective stopping $S(E)$ and the differential scattering cross section $d\sigma/d\Omega$ in the framework of quantum mechanics. In quantum theory, the differential cross section of elastic scattering, in which the atom remains in its initial state, or of inelastic scattering (the most important in this context), which is accompained by $|0\rangle \rightarrow |n\rangle$ transitions from one atomic state to another, are expressed through the corresponding scattering amplitude

$$\left(\frac{d\sigma}{d\Omega} \right)_{el} = |F_{el}(E, \vartheta)|^2 \tag{2.54}$$

$$\left(\frac{d\sigma_n}{d\Omega} \right) = \frac{k'}{k} |F_{0 \rightarrow n}(E, \vartheta)|^2 \tag{2.55}$$

where E is the energy of the incident particle and ϑ is the scattering angle. For determining the scattering amplitude it is generally necessary to solve a certain wave equation (or even a set of coupled equations) and to extract these amplitudes from the asymptotes of the corresponding wawe functions. Hovever, if the kinetic energy of the incident particle is much greater than its average energy of interaction with the atoms or molecules (and, in accordance with (2.51b), this is precisely the case of the fast particles we are interested in), the Born approximation can be used, within the framework of which the problem is essentially simplified.

2.2.1 Elastic scattering cross section

The Born amplitude for the elastic scattering process a+A→a+A is simply the integral

$$\mathbf{F}_{el}^{(Born)}(E, \vartheta) = -\frac{m_a}{2\pi\hbar^2} \int d^3 r\, e^{i\mathbf{k}'\cdot\mathbf{r}} V(\mathbf{r})\, e^{i\mathbf{k}\cdot\mathbf{r}} \qquad (2.56)$$

which contains the plane wave $\varphi_{\mathbf{k}} = e^{i\mathbf{k}\cdot\mathbf{r}}$ describing free motion of a particle a in the initial state, the wave function of the particle in the final state, $\varphi_{\mathbf{k}'} = e^{i\mathbf{k}'\cdot\mathbf{r}}$, and the interaction potential of the atom with the particle averaged over its ground state $|0\rangle$

$$V(\mathbf{r}) = \frac{Z_a Z e^2}{r} - \langle 0| \sum_{j=1} \frac{Z_a e^2}{|\mathbf{r} - \mathbf{r}_j|} |0\rangle \qquad (2.57)$$

[to be precise the mass of the incident particle, it is the reduced mass of the a+A system, $\mu = m_a - m_A/m_a + m_A$, that actually occurs in (2.56)]. The wave vectors $\mathbf{k}$ and $\mathbf{k}'$ in (2.56) represent, with an accuracy up to Planck constant, the momenta of the incident and scattered particles, respectively: $\mathbf{k} = \mathbf{p}/\hbar$; $\mathbf{k}' = \mathbf{p}'/\hbar$; below we shall just call vector $\mathbf{k}$ or $\mathbf{k}'$ the particle momentum. From (2.56) it is seeen that in the Born approximation the elastic scattering amplitude is the sum of two terms: the scattering amplitude due to interaction of particle a with the atomic nucleus and the scattering amplitude due to the interaction with the atomic electrons; the whole scattering pattern depends on the interference of these two amplitudes. The first summand is calculated by straightforward integration

$$\mathbf{F}_{el,nucl}^{(Born)}(E, \vartheta) = -\frac{\mu}{2\pi\hbar^2} \int d^3 r \frac{Z_a Z e^2}{r} e^{i(\mathbf{k}-\mathbf{k}')\cdot\mathbf{r}} = \frac{2\mu Z_a Z e^2}{\hbar^2 q^2} \qquad (2.58)$$

where we have introduced the *momentum transfer* $\mathbf{q}$ defined by

$$\mathbf{q} = \mathbf{k} - \mathbf{k}' \qquad (2.59)$$

and this is the only kinematic variable upon which the Born scattering amplitude depends. For calculating the second term in the elastic scattering amplitude, we shall introduce the electron density

$$\rho_{elec}(\mathbf{r}) = \langle 0| \sum_{j=1}^{Z} \delta(\mathbf{r} - \mathbf{r}_j) |0\rangle \qquad (2.60)$$

in terms of which we shall express the average interaction potential of the particle with the electron shell

$$\langle 0| \sum_{j=1}^{Z} \frac{Z_a e^2}{|\mathbf{r} - \mathbf{r}_j|} |0\rangle = \int d^3 r' \frac{Z_a e^2}{|\mathbf{r} - \mathbf{r}'|} \rho_{elec}(\mathbf{r}') \qquad (2.61)$$

Subtitution of (2.61) into (2.57) and use of (2.59) gives

$$\mathbf{F}_{el,nucl}^{(Born)}\left(E,\vartheta\right) = \frac{2\mu Z_a e^2}{\hbar^2 q^2} \int d^3 r \rho_{elec}\left(\mathbf{r}\right) e^{i\mathbf{q}\cdot\mathbf{r}} \tag{2.62}$$

At small q the integral present here can be readily seen to tend toward Z. At $q \gg 1/a$, where a is of the same order of magnitude as the size of the atom, it decays rapidly owing to oscillations of the exponential factor $e^{i\mathbf{q}\cdot\mathbf{r}}$. In the $0 < q < 1/a$ region, th edependence of this integral on q is determined by the shape of the electron density distribution, $\rho_{elec}\left(\mathbf{r}\right)$. Let us now introduce the *electron density form factor* of the atom,

$$\mathcal{F}_{elec}\left(\mathbf{q}\right) = \frac{1}{Z} \int d^3 r \rho_{elec}\left(\mathbf{r}\right) e^{i\mathbf{q}\cdot\mathbf{r}} = \frac{1}{Z} \langle 0| \sum_{j=1}^{Z} e^{i\mathbf{q}\cdot\mathbf{r}_j} |0\rangle \tag{2.63}$$

which, up to the factor $1/Z$ is the Fourier transform of the electron density. Upon collecting the summands in (2.58) and (2.62), we express the elastic scattering amplitude of the electron on the atom through $\mathcal{F}_{elec}\left(\mathbf{q}\right)$

$$\mathbf{F}_{el}\left(E,\vartheta\right) = -\frac{2\mu Z_a Z e^2}{\hbar^2 q^2}\left[1 - \mathcal{F}_{elec}\left(\mathbf{q}\right)\right] \tag{2.64}$$

Here and below, we shall drop the index 'Born', although we shall remember that this expression is not exact, but has been obtained in the Born approximation.

Thus the differential elastic cross section has the form

$$\left(\frac{d\sigma}{d\Omega}\right)_{el} = \frac{4\mu^2 Z_a^2 Z^2 e^4}{\hbar^4 q^4} |1 - \mathcal{F}_{elec}\left(\mathbf{q}\right)|^2 \tag{2.65}$$

When $q \gg 1$, it transforms into the scattering cross section of a particle of charge Z_a on a point-like center of charge Z and is described by Rutherford formula

$$\left.\left(\frac{d\sigma}{d\Omega}\right)\right|_{el}\Big|_{q\gg 1/a} \rightarrow \left(\frac{d\sigma}{d\Omega}\right)_{Ruth} \tag{2.66}$$

We shall use $(d\sigma/d\Omega)_R$ for the Rutherford cross section corresponding to the scattering of a particle of charge Z_a from a unit point charge $(Z = 1)$

$$\left(\frac{d\sigma}{d\Omega}\right)_{Ruth} \equiv \frac{4\mu^2 Z_a^2 e^4}{\hbar^4 q^4} = \frac{Z_a^2 e^4}{16 E^2 \sin^4 \frac{\vartheta}{2}} \tag{2.67}$$

In this notation the differential elastic scattering cross section of particle a scattering from the atoms assumes the form

$$\left(\frac{d\sigma}{d\Omega}\right)_{el} = Z^2 \left(\frac{d\sigma}{d\Omega}\right)_{Ruth} |1 - \mathcal{F}_{elec}\left(\mathbf{q}\right)|^2 \tag{2.68}$$

From the formula obtained it can be seen that at large momentum transfer $q \gg 1/a$, i.e., when the particle undergoes large-angle deviations, the scattered particle does not feel the electron shell of the atom and undergoes scattering the bare nucleus. On the contrary, when $q \ll 1/a$ (extremely small scattering angles),

the electron shell screens the nucleus, and the scattering cross section turns out to be essentially smaller than the Rutherford cross section.

2.2.2 Inelastic scattering cross section and stopping power formula

In the Born approximation, the cross section of inelastic scattering $\mathtt{a+A \rightarrow a'+A_n^*}$ is calculated as above for the case of elastic scattering and is expressed for each partial transition $|0\rangle \rightarrow |n\rangle$ in terms of the so called *transition*, or *inelastic, form factor* $\mathcal{F}_{0 \rightarrow n}(\mathbf{q})$

$$\frac{d\sigma_n}{d\Omega} = \frac{k'}{k} \left(\frac{d\sigma}{d\Omega} \right)_{Ruth} |\mathcal{F}_{0 \rightarrow n}(\mathbf{q})|^2 \tag{2.69}$$

$$\mathcal{F}_{0 \rightarrow n}(\mathbf{q}) = \langle n| \sum_{j=1}^{Z} e^{i\mathbf{q} \cdot \mathbf{r}_j} |0\rangle \tag{2.70}$$

Note that if the energy of the incident particles is much higher than the excitation energy of the atom (or molecule), the kinematic factor k'/k occurring in (2.69) pratically coincides with unity

$$\frac{k'}{k} = \sqrt{1 - \frac{\varepsilon_n - \varepsilon_0}{E}} \rightarrow 1 \tag{2.71}$$

We have thus prepeared all the necessary intermediate products from quantum collision theory necessary for our quantum-machanical examination of stopping of fast charged particles. Let us proceed to calculate the effective stopping, that is

$$S(E) \equiv \sum_n (\varepsilon_n - \varepsilon_0) \sigma_n \tag{2.72}$$

for which we shall first calculate the integral partial cross sections of inelastic scattering

$$\sigma_n = \int d\Omega \frac{d\sigma_n}{d\Omega} \tag{2.73}$$

Since when $k'/k \rightarrow 1$ the differential cross section $d\sigma_n/d\Omega$ depends on only one kinematic variable q, it is convenient to pass in (2.73) from integration over the scattering angle ϑ to integration over q. When the scattering angle ϑ varies from 0 up to π, the momentum transfer varies from $q_{min} = k - k'$ up to $q_{max} = k + k'$ in accordance with the law

$$q^2 = k^2 + k'^2 - 2kk' \cos \vartheta \tag{2.74}$$

We shall take into account the law of energy conservation

$$E - E' = \varepsilon_n - \varepsilon_0 \tag{2.75}$$

as well as the fact that the excitation energy is negligible as compared with the energy of the incident particles,

$$E - E' \ll E \tag{2.76}$$

Then, with good precision, we shall have

$$q_{\min} = \frac{k^2 - k'^2}{k + k'} \approx \frac{\varepsilon_n - \varepsilon_0}{\hbar v_a} \qquad q_{\max} \approx 2k \tag{2.77}$$

Moreover, taking into account (2.74), we have

$$d\Omega = 2\pi \sin \vartheta d\vartheta = 2\pi \frac{qdq}{kk'} \approx \frac{2\pi qdq}{k^2} \tag{2.78}$$

Thus, the partial cross section can be calculated by the formula

$$\sigma_n = \frac{2\pi}{k^2} \int_{q_{\min}}^{q_{\max}} dq q \frac{d\sigma_n}{d\Omega} \tag{2.79}$$

Now we substitute this expression into (2.72) and take $d\sigma_n/d\Omega$ from (2.69) $(k'/k \to 1)$

$$S(E) = \frac{2\pi}{k^2} \sum_n (\varepsilon_n - \varepsilon_0) \int_{q_{\min}}^{q_{\max}} dq q \frac{d\sigma_n}{d\Omega} =$$

$$= \frac{2\pi}{k^2} \frac{4\mu^2 Z_a^2 e^4}{\hbar^4} \sum_n (\varepsilon_n - \varepsilon_0) \int_{q_{\min}}^{q_{\max}} \frac{dq q}{q^4} |\langle n| \sum_{j=1}^{Z} e^{i\mathbf{q} \cdot \mathbf{r}_j} |0\rangle|^2 \tag{2.80}$$

In quantum mechanics, the validity of the following formula is proven

$$\sum_n (\varepsilon_n - \varepsilon_0) |\langle n| \sum_{j=1}^{Z} e^{i\mathbf{q} \cdot \mathbf{r}_j} |0\rangle|^2 = Z \frac{\hbar^2 q^2}{2m_e} \tag{2.81}$$

with the aid of which the infinite sum over all excited states of the atom is reduced exactly to a simple analytical expression. Regretfully we cannot apply it directly to (2.80), since the lower integration limit $q_{\min}$ depends on n itself [see (2.77)]. Therefore, we shall replace the lower limit in (2.80) by its mean value

$$q_{\min} \to \overline{q}_{\min} = \frac{\overline{(\varepsilon_n - \varepsilon_0)}}{\hbar v_a} \equiv \frac{I}{\hbar v_a} \tag{2.82}$$

We may now transpose the orders of summation and integration in (2.80). As a result we obtain

$$S(E) = \frac{2\pi}{k^2} \frac{4\mu^2 Z_a^2 e^4}{\hbar^4} \int_{q_{\min}}^{q_{\max}} \frac{dq}{q^3} \sum_n (\varepsilon_n - \varepsilon_0) |\langle n| \sum_{j=1}^{Z} e^{i\mathbf{q} \cdot \mathbf{r}_j} |0\rangle|^2 =$$

$$= \frac{4\pi Z_a^2 e^4 Z}{m_e v_a^2} \ln \frac{q_{\max} \hbar v_a}{I} \tag{2.83}$$

54

One can see here the parameter I, which is the mean excitation energy of the atom (or molecule) brought about by the passing particle. A consistent caluclation will be perfirmed in Section 2.3, and therein the following formula will also be obtained, which express I through the well known *transition oscillator strengths* f_{n0}

$$\ln I = \frac{1}{Z} \sum_n f_{n0} \ln (\varepsilon_n - \varepsilon_0) \tag{2.84}$$

Application of this formula in the case of hydrogen, for example, yelds $I = 14.9$ eV. This exceed the ionization potential $I_{ioniz} = 13.6$ eV. Thus, the main contribution to the stopping of a particle is indeed, due to ionization of the atom or molecule, and not to excitation of its discrete levels. Now, let us again turn to the above expression (2.83) for effective stopping, in which we have not yet revealed the meaning of the symbol q_{max}. Formally, $q_{max} = 2k$, and this value is attained when the incident particle scatters from the atom backwards. However, this may happen very rarely and even then, only when our heavy incident particle interacts with a particle that is also heavy, i.e. with the nucleus of an atom. But at present we are interested in the excitation or ionization process of the atom, when energy is transferred directly from the incident particle to the atomic electron. Therefore, q_{max} in (2.83) is actually determined by the collision kinematics of the collision between a heavy particle and an electron. If this electron were at rest before the collision, then from the kinematics of an elastic collision, a+e→a+e, it would be easy to calculate the maximum momentum of the electron after the collision: with high precision, it is $2m_e v_a$, where v_a is the velocity of the incident particle. In our conditions [remember relation (2.51)] the quantity $2m_e v_a$ is significantly greater than the average momentum of an electron in the atom before it undergoes interaction with the heavy particle. Therefore the motion of the electron in the atom can be neglected, and the value obtained may be used in estimating the maximum momentum transferred by the incident particle to the atomic electron

$$\hbar q_{max} = 2m_e v_a \tag{2.85}$$

It now remains for us to sobstitute (2.85) into (2.83)

$$S(E) = \frac{4\pi Z_a^2 e^4 Z}{m_e v_a^2} \ln \frac{2m_e v_a^2}{I} \tag{2.86}$$

We now multiply this expression by the concentration of atoms in the medium and obtain the stopping power of the medium

$$-\frac{dE}{dx} = \underbrace{\left(\frac{4\pi Z_a^2 e^4}{m_e v_a^2}\right)}_{\substack{\text{main dependence} \\ \text{on particle velocity}}} \times \underbrace{(Z n_0)}_{\substack{\text{main dependence} \\ \text{on medium properties}}} \times \underbrace{\left(\ln \frac{2m_e v_a^2}{I}\right)}_{\substack{\text{weak dependence} \\ \text{on particle velocity} \\ \text{and medium properties}}} \tag{2.87}$$

This final formula, obtained within the framework of the quantum approach, exhibits the same principal features of energy loss of a charged particle. It is

clearly seen that the experimentally established dependence of the stopping power on the particle velocity (energy), if considered throughout the entire range of these variables, is significantly more complicated than what follows from our formula (2.87). In Subsection 2.3.3 we shall discuss various corrections to this dependence, but for the time being we shall note only that, for example for protons, a significant part of the $-dE/dx$ curve, corresponding to energies of approximately hundreds of keV up to a hundred MeV, the simple law $-dE/dx \sim 1/v_a^2$ is obeyed, and for this reason we could take advantage of it for obtaining qualitative estimates.

2.3 Dielectric theory of stopping power

The assumption that in passing through a medium a particle undergoes independent pair collisions with individual atoms turns out to be too inaccurate for examining the passage of particles through dense media, for example water, used as target model in radiation biology. One of the effects not taken into account in this approximation is the *polarization effect* of the atoms of the medium under the influence of the electric field of the passing charged particle. Polarization of the medium weakens the influence of the electric field of the particle on the atomic electrons, so the energy transferred to them from the particle and, consequently, the stopping power of the medium is *reduced*. Hence it is seen that the stopping mechanism of charged particles in various media is somehow related to the *dielectric properties* of the medium. It is no chance that in studies of ionization stopping in biological material such as liquid water, a significant place is occupied by the dielectric theory of this phenomenon, which was described in Section 2.1. Let us consider its main points.

Consider a heavy charged particle a travelling at a velocity v ($v \ll c$) in a medium with a dielectric constant ε; the dispersion law $\varepsilon = \varepsilon(\omega)$, where ω is the angular frequency of the electric field, will be considered known. Thus, from optics and atomic physics we know that in a rarefied medium $\varepsilon(\omega)$ obeys the dispersion formula

$$\varepsilon(\omega) = 1 + \frac{4\pi e^2 n_0}{m_e} \sum_\nu \frac{f_\nu}{\omega_\nu^2 - \omega^2 - i\omega\gamma_\nu} \tag{2.88}$$

where n_0 is the number of atoms per unit volume of the medium, ω_ν are the natural frequencies of the atoms of the medium, f_ν are the 'weights' (or oscillator strengths) of the respective transitions, and γ_ν are the damping coefficients of natural oscillations. The potential created by a moving particle a is found from the general equations of electrodynamics

$$\Delta\varphi(\mathbf{r}, t) = -4\pi\rho(\mathbf{r}, t) \tag{2.89}$$

where the charge density, according to our condition, has the form

$$\rho(\mathbf{r}, t) = Z_0 e\delta(\mathbf{r} - \mathbf{v}t) \tag{2.90}$$

It is easy to check by substitution that the following is the solution of (2.89)

$$\varphi\left(\mathbf{r},t\right)=\frac{1}{\left(2\pi\right)^{3}}\int d^{3}k\frac{4\pi Z_{a}e}{k^{2}}e^{i\mathbf{k}\cdot\left(\mathbf{r}-\mathbf{v}t\right)} \tag{2.91}$$

Hence it is seen that the electric field caused by the particle can be represented as a continuous set of monochromatic waves with frequencies calculated by the formula

$$\omega=\mathbf{k}\cdot\mathbf{v} \tag{2.92}$$

If our particle a were moving in empty space, the electric field strength created by it could be found from

$$\mathbf{E}_{0}\left(\mathbf{r},t\right)=\nabla\varphi\left(\mathbf{r},t\right)=-\frac{1}{\left(2\pi\right)^{3}}\int d^{3}k\frac{4\pi Z_{a}e}{k^{2}}i\mathbf{k}e^{i\mathbf{k}\cdot\left(\mathbf{r}-\mathbf{v}t\right)} \tag{2.93}$$

When the particle travels in a dielectric medium, this formula is changed in

$$\mathbf{E}_{0}\left(\mathbf{r},t\right)\rightarrow\mathbf{E}\left(\mathbf{r},t\right)=\frac{1}{\left(2\pi\right)^{3}}\int d^{3}k\left(\frac{1}{\varepsilon\left(\omega\right)}\right)\frac{4\pi Z_{a}e}{k^{2}}i\mathbf{k}e^{i\mathbf{k}\cdot\left(\mathbf{r}-\mathbf{v}t\right)} \tag{2.94}$$

The stopping force exerted by the medium of the particle is the difference effect, that is

$$F\left(\mathbf{r}=\mathbf{v}t\right)=Z_{a}e\left[\mathbf{E}\left(\mathbf{r},t\right)-\mathbf{E}_{0}\left(\mathbf{r},t\right)\right]_{r=vt}=$$
$$=-i\frac{1}{\left(2\pi\right)^{3}}\int d^{3}k\frac{4\pi Z_{a}e}{k^{2}}\mathbf{k}\left(\frac{1}{\varepsilon\left(\omega\right)}-1\right) \tag{2.95}$$

To simplify this integral we write down the differential as

$$d^{3}k=k^{2}dk\sin\vartheta d\vartheta d\varphi$$

(where ϑ is the angle between vectors $\mathbf{k}$ and $\mathbf{v}$, and φ is the corresponding azimuthal angle), and using (2.92) we express ω through ϑ as $\omega=kv\cos\vartheta$. Then, integration over ϑ within the limits of 0 and π may be replaced by integration over ω from $\omega=kv$ to $\omega=-kv$; here, $d\omega=-kv\sin\vartheta d\vartheta$. As a result, we find that the force $F(\mathbf{r}=\mathbf{v}t)$ has only a longitudinal component along the direction of motion of the particle, $\mathbf{v}$, and its value is given by the expression

$$F\left(\mathbf{r}=\mathbf{v}t\right)=-i\frac{Z_{a}^{2}e^{2}}{\pi v^{2}}\int_{0}^{\infty}\frac{dk}{k}\int_{-kv}^{+kv}\left(\frac{1}{\varepsilon\left(\omega\right)}-1\right)\omega d\omega \tag{2.96}$$

For computing the integral (2.96) it is necessary to know the dielectric constant of the medium, $\varepsilon\left(\omega\right)$ as a function of the frequency not only for positive but also for negative values of ω, i.e., including the nonphysical range of ω values. To this end one may take advantage of the general relationships known from optics for the

real and imaginary parts of the dielectric constant $\varepsilon\left(\omega\right)$ as an analytic function of ω

$$\begin{aligned}
\Re e\left[\varepsilon\left(\omega\right)\right] &= \Re e\left[\varepsilon\left(-\omega\right)\right] \\
\Im m\left[\varepsilon\left(\omega\right)\right] &= -\Im m\left[\varepsilon\left(-\omega\right)\right]
\end{aligned}$$

With these relations taken into account it can be seen that the stopping force (2.96) or, which is the same, the stopping power of the medium, $-dE/dx = |F\left(\mathbf{r}=\mathbf{v}t\right)|$, is fully determined by the imaginary part of the dielectric constant, that is

$$-\frac{dE}{dx} = \frac{Z_a^2 e^2}{\pi v^2}\Im m\left[\int_0^\infty \frac{dk}{k}\int_{-kv}^{+kv} d\omega\frac{1}{\varepsilon\left(\omega\right)}\omega\right] \tag{2.97}$$

2.3.1 Application of the dielectric theory: stopping power in a rarefied gas

Let us calculate the stopping power of a rarefied gas. From (2.88) it is seen that, in the case of a sufficiently low concentration of atoms, n_0, the dielectric constant $\varepsilon\left(\omega\right)$ differs little from unity. This means that the approximate expression given by

$$\frac{1}{\varepsilon\left(\omega\right)} \approx 1 - \frac{4\pi e^2 n_0}{m_e}\sum_\nu\frac{f_\nu}{\omega_\nu^2-\omega^2-i\omega\gamma_\nu} \tag{2.98}$$

can be substituted for $1/\varepsilon\left(\omega\right)$ in (3.11). As a result, we obtain

$$-\frac{dE}{dx} \approx \frac{4\pi Z_a^2 e^4 n_0}{m_e v^2}\sum_\nu f_\nu\int_{\omega_\nu/v}\frac{dk}{k} \tag{2.99}$$

Here we took advantage of the relation

$$\int_{-kv}^{+kv} d\omega\omega\frac{\omega\gamma}{\left(\omega_\nu^2-\omega^2\right)^2+\omega^2\gamma^2}\bigg|_{\gamma\to 0} = 0, \quad\text{if}\quad kv<\omega_\nu \tag{2.100}$$

with the aid of which the lower limit of the integral over the variabie k is determined. The physicai meaning of this variable is the transfer of momentum to the atom of the medium resulting from the influence of the electric field of the moving charge. Formally, the integral $\int dk/k$ in (2.99) is taken from $k_{\min}=\omega_0/v$ up to infinity. Actually, the momentum transferred to the atom in an inelastic collision is limited: $\hbar k_{\max}\approx 2m_e v$.

Substitution of this value into (2.99) yields

$$-\frac{dE}{dx} = \frac{4\pi Z_a^2 e^4 n_0}{m_e v^2}\sum_\nu f_\nu\int_{\omega_\nu/v}^{2m_e v/\hbar}\frac{dk}{k} = \frac{4\pi Z_a^2 e^4 n_0}{m_e v^2}\sum_\nu f_\nu\ln\frac{2m_e v^2}{\hbar\omega_\nu} \tag{2.101}$$

Now, we shall apply the sum rule, known from atomic physics, for the oscillator strengths

$$\sum_{\nu} f_{\nu} = Z \tag{2.102}$$

where, Z is the number of electrons in the atom. We define the mean excitation energy of the atom, I, by the relation

$$\ln I \equiv \frac{1}{Z} \sum_{\nu} f_{\nu} \ln \left(\hbar \omega_{\nu} \right) \tag{2.103}$$

and use it to express the stopping power of the medium

$$-\frac{dE}{dx} = \frac{4\pi Z_a^2 e^4 n_0}{m_e v^2} Z n_0 \ln \frac{2 m_e v^2}{I} \tag{2.104}$$

Formally, (2.104) is identical to (2.87), derived above within the framework of the quantum theory of ionization stopping. The mean excitation energy of the atom, I, occurring in (2.87) remained undetermined; on the contrary, here it is given by relation (2.103) and, consequently, can be calculated in a straightforward manner if the distribution of the oscillator strengths in an atom of the medium is known[6]. In Section 2.2 it has already been noted that calculations performed for various atoms always reveal the mean energy I to be higher than the ionization potential of the atom.

2.3.2 Stopping of a charged particle in a degenerate electron gas

The problem, we are about to consider is widely applied in theoretical studies of the passage of charged particles through plasma and condensed media. In this aspect it is quite the opposite of the problem we have just dealtwith in Subsection 2.3.1: therein we diverted our attention from any collective effects relevant to the passage of particles through matter, whereas now the collective stopping mechanism will occupy a most important place.

From atomic physics it is known that the main characteristics of a degenerate electron gas are the Fermi boundary (defined as the limit energy of an electron ε_F or its momentum k_F) and the frequency of collective (*plasma*) oscillations, ω_0, the *plasma frequency*. Both these characteristics are expressed in terms of the electron density n_e

$$k_F = \left(3\pi^2 n_e \right)^{1/3} \tag{2.105}$$

$$\omega_0 = \sqrt{\frac{4\pi e^2 n_e}{m_e}} \tag{2.106}$$

---

[6]Problems rise when the calculation of oscillator strengths regards complex atoms or molecules through the determination of eigenstates expressions.

For orientation, we note that the average electron density n_e in metals is of the order of 10^{23} cm^{-3}, i.e., of the order of unity in atomic units. From (2.105) and (2.106) it follows that, in this case, k_F and ω_0 are also of the order of several atomic units, i.e., k_F and ω_0 are of the order of 10 eV. According to the dielectric theory, the stopping power of any substance is determined by its dielectric constant. We shall not derive the dependence $\varepsilon(\omega)$ on parameters characterizing the state of an electron gas and the charged particle passing through it. We shall, however, note the main points in obtaining the final formula. In Section 2.3 it was shown that a charged particle carries with it a 'packet' of photons exhibiting special properties in relation to the quanta of the free electromagnetic field: the frequency ω and wave vector k are not related to each other by the usuail relation $\omega = kc$. These are so-called *virtual photons*. For them, however, like for ordinary photons, the law of momentum conservation is obeyed in interactions with electrons of the medium

$$\mathbf{k}'_e = \mathbf{k}_e + \mathbf{k} \tag{2.107}$$

where $\mathbf{k}_e$ and $\mathbf{k}'_e$ are the initial and final momenta of a free electron of the medium. Hence the energy transferred from a particle to the medium, when a virtual photon with a wave vector $\mathbf{k}$ is absorbed by an electron with an initial momentum $\mathbf{k}_e$, is

$$\Delta E = \frac{\hbar^2 k_e'^2}{2m_e} - \frac{\hbar^2 k_e^2}{2m_e} = \frac{\hbar^2}{2m_e}\left[(\mathbf{k}_e + \mathbf{k})^2 - \mathbf{k}_e^2\right] \tag{2.108}$$

(by the way, note that absorption of an ordinary, real photon by a free electron is impossible, since the laws of momentum and energy conservation cannot be satisfied simultaneously in this case). Here, we must recall the Pauli principle: an electron in a degenerate electron gas can undergo transition from an initial state $|\mathbf{k}_e\rangle$ to another state $|\mathbf{k}'_e\rangle$ only if this final state lies beyond the Fermi sphere, i.e., if $k'_e > k_F$. We now turn to the general formula for the dielectric constant, (2.88). In applying it to the case of a degenerate electron gas, we substitute a continuous set of values $\Delta E/\hbar$, where ΔE is taken from (2.108), for the spectrum of eigenfrequencies ω_ν; the electron density is substituted for the number of atoms, n_0, per unit volume of the medium, and the corresponding *probabilities of one-electron transitions*, $f(\mathbf{k}_e \rightarrow \mathbf{k}'_e)$ are substituted for the oscillator strengths f_ν. Here, summation over ν is replaced by integration over all the initial electron states, i.e., over all the states inside the Fermi sphere. Taking the conservation law (2.107) and the Pauli principle,

$$\varepsilon(k,\omega) = 1 + \frac{4\pi e^2 n_0}{m_e}\int d^3 k_e \frac{f(\mathbf{k}_e \rightarrow \mathbf{k}_e + \mathbf{k})}{\frac{\hbar^2}{4m_e^2}\left|(\mathbf{k}_e + \mathbf{k})^2 - \mathbf{k}_e^2\right|^2 - \omega^2 - i\omega\gamma}\Bigg|_{\mathbf{k}_e \leq \mathbf{k}_F\ ;\ |\mathbf{k}_e + \mathbf{k}| > k_F} \tag{2.109}$$

into account provides for all possible final states being taken into account also [note that the whole combination of factors before the integral is nothing but the

60

square of the plasma frequency]. It remains for us to substitute here the appropriate expression for the probability of an one-electron transition, $f\left(\mathbf{k}_e \to \mathbf{k}'_e\right)$ (it is given by quantum electrodynamics), to perform integration over $d^3 k_e$ taking the restrictions indicated into account, and then to substitute the expression obtained for the dielectric function $\varepsilon\left(k, \omega\right)$ into the integral in (2.97). Generally, this entire integration procedure can be fulfilled only numerically. As to the analytical formuls, they can be obtained only approximately and, even in such cases, only if certain relations exist between various parameters of the problem. Thus, if the velocity of the passing particle is much greater that the velocity of an electron on the Fermi surface, i.e., $v \gg v_F = \hbar k_F / m_e$, the stopping power of the degenerate electron gas is calculated by

$$-\frac{dE}{dx} = \frac{4\pi Z_a^2 e^4}{m_e v^2} n_e \left[\ln \frac{2 m_e v^2}{\hbar \omega_0} - \frac{3}{5}\left(\frac{v_F}{v}\right)^2 - \frac{3}{14}\left(\frac{v_F}{v}\right)^4 + \ldots\right] \qquad (2.110)$$

where higher-order terms are omitted.

We have on hand a close resemblance between the obtained expression and the already familiar formuls for the stopping power of a medium. Comparing it, far instance, with (2.87) we see that the energy of plasma oscillations, $\hbar \omega_0$, plays the same part in (2.110) as the mean excitation energy of an atom, I, does in formula (2.87). The simple physical meaning of the result presented is revealed: *a fast charged particle passing through a degenerate electron gas is slowed down owing to the excitation of collective plasma oscillations in the gas.* One must not forget that (2.110) is valid only under the condition that $v \gg v_F$. If this condition is not fulfilled we write the stopping power of a degenerate electron gas in the form suggested by expression (2.87)

$$-\frac{dE}{dx} = \frac{4\pi Z_a^2 e^4}{m_e v^2} n_e \mathcal{L}\left[n_e, v\right] \qquad (2.111)$$

By explicitly writing out the arguments n_e and v in the last factor $\mathcal{L} = \mathcal{L}\left[n_e, v\right]$ we stress that the electron gas density n_e enters into $-dE/dx$ not only as a trivial proportionality factor, but also, in a more complex way, via $\mathcal{L}\left[n_e, v\right]$ and, far instance, via the plasma frequency $\omega_0 = \omega_0\left(n_e\right)$

$$\mathcal{L}\left[n_e, v\right] \approx \ln \frac{2 m_e v^2}{\hbar \omega_0} \qquad (2.112)$$

Note that the dependence of the factor $\mathcal{L}\left[n_e, v\right]$ upon the electron density *weakens* the rise of the stopping power of matter as n_e increases.

2.3.3 Relativistic effects: the Bethe-Bloch formula

According to the nonrelativistic theory of ionization stopping, the maximum momentum that can be transferred from a heavy particle of mass $m_a \gg m_e$ to an electron is $2 m_e v$. Relativistic kinematics gives another result for this quantity

$$(p_e)_{\text{max}} = \frac{2m_e v}{\sqrt{1 - \beta^2}} \tag{2.113}$$

i.e., the region of integration over the momentum transferred, when the effective stopping $S(E)$ is calculated, is extended in comparison with what is given by (2.80-2.86), and taking relativism into account leads to enhancement of the effective stopping as compared with predictions of nonrelativistic theory. The physical reason for such an enhancement is the effect of relativistic *compression* of the electric field of a passing particle: in the direction of flight of the particle the field is reduced by a factor of $(1 - \beta^2)$, whereas in the transverse direction it is enhanced by a factor of $1/\sqrt{1 - \beta^2}$, and thus influences a greater number of the electrons of the medium than would be possible if the field were spherically symmetric. Taking relativism into account consistently yields the following result for the stopping power

$$-\frac{dE}{dx} = \frac{4\pi Z_a^2 e^4}{m_e v^2} Z n_0 \left[\ln\left(\frac{2m_e v^2}{I}\right) + \ln\left(\frac{1}{1 - \beta^2}\right) - \beta^2 \right] \tag{2.114}$$

At $v \ll c$ this formula transforms into (2.87), and in the relativistic limit of $v \to c$ it exhibits a constant, although slow, rise in the stopping power. Actually, such an infinite rise is not observed: it is hindered by the *density effect*, the screening of the influence the field of the passing particle has on the distant atoms of the medium, which is due to the atoms nearest to the particle being polarized. To take the density effect into account, one more correction is introduced in formula (2.114)

$$-\frac{dE}{dx} = \frac{4\pi Z_a^2 e^4}{m_e v^2} Z n_0 \left[\ln\left(\frac{2m_e v^2}{I}\right) + \ln\left(\frac{1}{1 - \beta^2}\right) - \beta^2 + \delta \right] \tag{2.115}$$

The term δ, the explicit dependence of which on the parameters is given by different authors differently, reflects the restrictive action of the polarization of the medium.

This effect is insignificant in gases, and the logarithmic rise in the energy dependence of the stopping power is observed up to extremely high energies. In solids and liquids, where the electron density is high, the polarization effect is more pronounced. In condensed media, the $-dE/dx$, expressed equivalently as mass stopping power, curve reaches a minimum at approximately $E = m_a c^2$, and then undergoes an insignificant rise practically reaching a plateau. Formula (2.115), the main formula in the theory of ionization stopping of heavy fast charged particles, is called the *Bethe-Bloch formula*.

2.4 Ion charge-changing effects and the effective charge

Consider a fast particle a of charge $Z_a \gg 1$ passing through a medium. The familiar processes of excitation and ionization of the atoms of a medium, taking place when such a particle interacts with the atomic electrons, are accompanied by intense capture processes of these electrons. If $Z_a \gg 1$, such states of the a+e system will always be found, transition to which (at least of the outer electrons of the atoms of the medium) is favored from the point of view of energy (see Fig. 2.7). The probability of resonance processes ($\varepsilon_f \approx \varepsilon_i$) is also significant when capture proceeds not to the ground or any other low-lying state but to highly excited states of the a+e system.
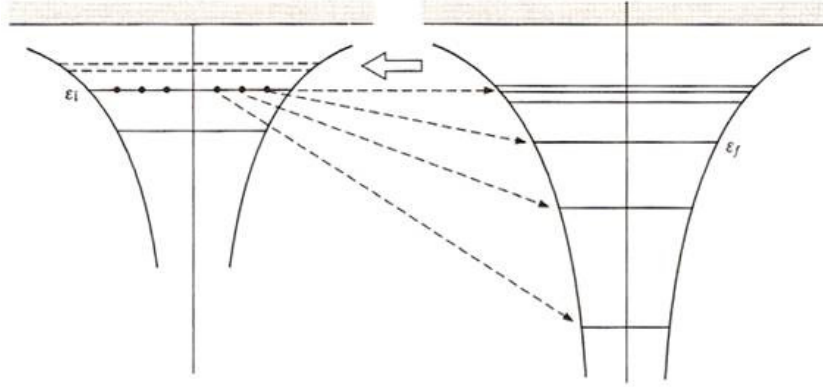
Figure 2.7: Scheme of charge exchange occurring when an ion passes through substance: on the *left* are the energy levels of the external electrons in the atom of the substance, on the *right* are the energy levels of the ion-electron system.

The process described results in alteration of the charge state of the particle passing by, and it is conventionally called *charge exchange*. Imagine the particle starting its motion in the medium as a 'bare' ion of charge Z_a. Owing to charge exchange, a cloud of bound electrons gradually grows up around it. As the number of such electrons increases, they occupy more and more orbits in the field of the charge Z_a, which results in the inverse process - the passing ion losing a part of the acquired electrons (so called *stripping*) - becoming more significant. The combination of capture and stripping makes the charge exchange process exhibit a dynamic character in the case of multicharge ions, and when a beam of such ions passes through a medium we always have to deal with a whole set of various charge states of the ion.

Let the quantity $N(Z_a', x)$ characterize the intensity of the fraction of charge Z_a' in this composite beam at a distance x from the entrance of the beam to the medium. The distribution of various charge states in the beam may be characterized by weight coefficients

63

$$p\left(Z'_a, x\right) = \frac{N\left(Z'_a, x\right)}{\sum_{Z'_a} N\left(Z'_a, x\right)}$$

and via these coefficients it is possible to determine the mean charge and the dispersion of the charge distribution by the relations

$$\overline{Z}_a(x) = \sum_{Z'_a} Z'_a p\left(Z'_a, x\right)$$

$$D_{Z_a}(x) = \sum_{Z'_a} \left[Z'_a - \overline{Z_a(x)}\right]^2 p\left(Z'_a, x\right)$$

all for any arbitrarily chosen x.

If $\overline{\sigma}_{ex}$ is the mean charge exchange cross section, then the quantity $l_{ex} = \left(\overline{\sigma}_{ex} n_0\right)^{-1}$ where n_0 is the density of the atoms in the medium, is the mean path the beam must cover before the distribution of charge states in the beam is stabilized, i.e., a dynamic equilibrium is established between the capture and loss of electrons by an ion. The equilibrium mean ion charge

$$\overline{Z}_a(\infty) = \sum_{Z'_a} Z'_a p\left(Z'_a, x \gg l_{ex}\right)$$

and the dispersion of the equilibrium distribution are determined accordingly.
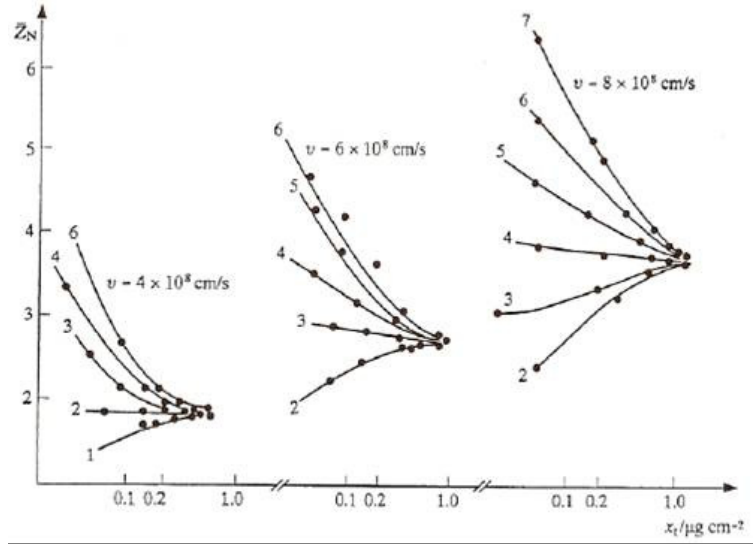
Figure 2.8: Mean charge of nitrogen ions passing through a nitrogen gas target N_2 [15]. For clarity, curves are drawn through experimental points, the number near the curves indicate the initial charge Z_N^{in}; the horizontal axis represents the target thickness x_t.

The equilibrium distribution of charge states of multicharge ions is seen to be established from experiments in which the passage of multicharge ions through matter is studied, given various initial ion charges Z_a^{in} - both above and below the

equilibrium value - at the entrance to the target. When $Z_a^{in} \gg \overline{Z}_a(\infty)$, the mean charge of the ions, $Z_a(x)$, falls monotonously as they pass through the medium, and when $Z_a^{in} \ll \overline{Z}_a(\infty)$ it rises monotonously and tends toward one and the same limit (see Fig. 2.8). Note that the higher the velocity of an ion, the easier it loses its electron instead of capturing an electron from an atom of the medium, i.e., the more the dynamic equilibrium shifts toward large values of the equilibrium charge $\overline{Z}_a(\infty)$. The charge exchange process strongly affects the stopping of multicharge ions in matter. Thus, if a beam of "bare" ions of charge Z_a impinges upon the target, then the decrease in its mean charge $Z_a(x)$, occurring as the ions penetrate the medium, leads to a weakening in the interaction of the ions with the atoms of the medium. Although the stopping power of a medium for a 'bare' multicharge ion should be greater than that for a proton of the same velocity, by a factor of Z_a^2, the stopping power for a multicharged ion is actually significantly smaller

$$\left(-\frac{dE}{dx}\right)_a < Z_a^2 \left(-\frac{dE}{dx}\right)_{proton}$$

In the characterization of the stopping of multicharge ions the special concept of the effective charge of an ion is introduced, which is close, but not identical to the concept of equilibrium charge, $\overline{Z}_a(\infty)$. The *effective charge* of a multicharge ion, Z_a^*, is defined as the ratio between the actual values of the stopping power of a medium for the ions (under conditions of an equilibrium charge distribution) and the stopping power for protons having the same velocity

$$Z_a^* = \sqrt{\frac{\left(-\frac{dE}{dx}\right)_a}{\left(-\frac{dE}{dx}\right)_p}}$$

From this definition it is seen that Z_a^* is the charge of a hypothetical charged particle that is always totally deprived of any electron shell, which would experience the same stopping in the medium as a real particle of charge Z_a. Experiments show that the effective charge Z_a^* may assume values within a broad range: it is very small at low ion velocities and tends toward the charge of a 'bare' ion, Z_a, at high velocities. Its dependence on the ion velocity can be approximated in water by the so called *Barkas formula*, widely used in radiation biology,

$$Z_a^* = Z_a \left[1 - \exp\left(-v/v_B Z_a^{2/3}\right)\right]$$

the physical meaning of which can be clarified by the following arguments ($v_B = \alpha c \approx 2 \times 10^8$ cm/s, is the Bohr velocity) . If the mean electron velocity inside an ion is much smaller than the velocity of the ion itself, the probability of stripping is high and the ion is not capable of carrying a large number of electrons with it. In the opposite case the process of the ion colliding with the atoms of the medium proceeds adiabatically, and electron stripping becomes difficult. At this point what is important to underline is that the effective charge should be used when scaling from proton cross sections to obtain heavier ion cross sections to take into account the charge changing effects described above.

2.5 Dielectric theory for electron and proton inelastic scattering cross section

For the interaction of charged particles (electrons and protons) with liquid water (or any other condensed material) it is appropriate to use the *dielectric-response function* as generally discussed in the previous Section and recently developed by different authors [16, 17, 25, 24]. Provided that an external charged particle is sufficiently fast, the dielectric response of matter upon sudden transfer of energy E and momentum $\hbar\mathbf{K}$ is given in terms of the function $\varepsilon(E, K)$, a characteristic of matter, which is defined and and can also be interpreted in the following way. Suppose that an applied electric field $\mathbf{E}$ dependent on time and space induces in matter an electric displacement $\mathbf{D}$, which is necessarily dependent on time and space and that the electric field is sufficiently weak. Then, one may write $\mathbf{D} = \widehat{\varepsilon}\mathbf{E}$, where $\widehat{\varepsilon}$ is an integral operator involving time and space variables. When both $\mathbf{E}$ and $\mathbf{D}$ are decomposed into Fourier components at frequency $E/\hbar$ and wave number K, the operator is represented by a multiplicative complex coefficient $\varepsilon(E, K)$. In general, $\mathbf{D}$ and $\mathbf{E}$ are not necessarily parallel and $\varepsilon(E, K)$ is a tensor. However, in what follows, we treat a scalar function $\varepsilon(E, K)$ representing the average over the spatial orientation. According to the plane wave Born approximation, the probability of energy transfer E and momentum transfer $\hbar\mathbf{K}$ is proportional $\Im m[-1/\varepsilon(E, K)]$. It is often convenient to use the system of atomic units, in which the length is expressed in units of the Bohr radius $a_0 = \hbar^2/me^2$, the momentum in units of $\hbar/a_0 = me^2/\hbar$ and the energy in units of *Hartrees* (1 Hartree $= me^4/\hbar^2 = 2$ Ry).

2.5.1 Calculation of the dielectric response function: the dipole limit and the Drude model

A basic task is to determine $\varepsilon(E, K)$ numerically at all values of E and K. One begins with $K = 0$, viz. the *dipole limit*, which applies to soft collisions in which external particles glances the target molecule at a large impact parameter. Following the general theory best explained in [20], one first adopts a plausible dependence of $\varepsilon_2(E, 0) = \Im m \varepsilon(E, 0) \geq 0$ for $E < 0$. The non-negative property reflects the fact that the material absorbs energy. When a value of $\varepsilon_2(E, 0)$ for $E \leqslant 0$ is required in certain calculations, one extends the function using the relationship $\varepsilon_2(E, 0) = -\varepsilon_2(-E, 0)$. Perhaps to facilitate numerical work it is possible to use [16, 17] a linear superposition $\varepsilon^{(D)}$ of the Drude functions to approximate ϵ. In the original Drude model, one considers an electron subject to a harmonic binding force $-m\omega_j^2 x$ plus a damping force $-mg_j\dot{x}$, where x is the displacement, ω_j is the characteristic angular frequency and $g_j > 0$ is the damping coefficient. The electron is also subject to a force $-e \exp(-i\omega t)$ due to a spatially uniform electric field of unit strength. Then, the electron gives rise to a dipole moment $e^2/m \left(\omega_j^2 - \omega^2 - ig_f\omega\right)^{-1} \exp(-i\omega t)$. If there are n electrons per unit volume, the induced polarization is $(4\pi ne^2/m) \left(\omega_j^2 - \omega^2 - ig_f\omega\right)^{-1}$ and the dielectric response

function $\varepsilon(E, 0)$ is

$$\varepsilon^{(D)}(E, 0) = 1 + \frac{\omega_p^2}{\omega_j^2 - \omega^2 - i g_j \omega} \tag{2.116}$$

where $\omega_p^2 = 4\pi n e^2 / m$ is the plasma angular frequency.

For convenience one may recast the above expression in the form

$$\varepsilon^{(D)}(E, 0) = 1 + \frac{E_p^2}{E_j^2 - E^2 - i \gamma_j E} \tag{2.117}$$

using the photon energy $E = \hbar \omega$ as a variable, the characteristic oscillator energy $E_j = \hbar \omega_j$, the oscillator energy width $\gamma_j = \hbar g_j$ and the plasmon energy of free electrons

$$E_p = \hbar \omega_p = \hbar \left(4\pi n e^2 / m \right)^{1/2} = 4\sqrt{\pi} \left(n a_0^3 \right)^{1/2} Ry \tag{2.118}$$

Equation (2.1) implies the following expression for the real and imaginary parts

$$\Re e \varepsilon^{(D)} = \varepsilon_1^{(D)} = 1 + \frac{E_p^2 \left(E_j^2 - E^2 \right)}{\left(E^2 - E_j^2 \right)^2 + \gamma_j^2 E^2} \tag{2.119}$$

$$\Im m \varepsilon^{(D)} = \varepsilon_2^{(D)} = \frac{E_p^2 \gamma_j^2 E}{\left(E^2 - E_j^2 \right)^2 + \gamma_j^2 E^2} \tag{2.120}$$

Now it is important to underline that the dielectric response of any real material cannot be fully described by the *Drude model*, which presumes the binding energy by an harmonic force, thus permits no ionization and fails to account for greatly different binding energies depending on the electron shell structure. For this reason it was found [16, 17] that Drude model fits realistic data in limited domains of E, with parameters E_j and γ_j specific to each of the energetic domains. In other words no single choice of these parameters enables one to fit the data over the entire range of E.

Some models have been proposed to permit a wide energy range of application of the Drude model and one of the most recent is that proposed in [16, 17] where one of the possible way to treat data over the entire range of E was the use of a linear superposition of Drude functions with different values of E_j and γ_j, that is to set

$$\varepsilon_2(E, 0) = E_p^2 \sum_j f_j \frac{\gamma_j E}{\left(E^2 - E_j^2 \right)^2 + \gamma_j^2 E^2} \tag{2.121}$$

where f_j is the effective number of oscillator characterized by E_j and γ_j and treat f_j, E_j and γ_j as fitting parameters. Here one must choose f_j so that the sum rule

$$\int_0^\infty dE E \varepsilon_2(E, 0) = \frac{\pi}{2} E_p^2 \tag{2.122}$$

is satisfied (this ensures the correct behavior of $\varepsilon_2(E, 0)$ at high E). Then the Kramers-Kronig relationship [20]

$$\varepsilon_1(E, 0) = 1 + \frac{1}{\pi} \wp \int_{-\infty}^{+\infty} dE' \frac{\varepsilon_2(E', 0)}{E' - E} \tag{2.123}$$

where $\wp$ stands for the Cauchy principal value, enables one to obtain

$$\varepsilon_1(E, 0) = 1 + E_p^2 \sum_j \frac{f_j(E_j^2 - E^2)}{(E^2 - E_j^2)^2 + \gamma_j^2 E^2} \tag{2.124}$$

The probability of energy transfer E from fast charged particle at the dipole limit is given by

$$\eta_2(E, 0) = \Im m \eta(E, 0) \tag{2.125}$$

where we define

$$\eta(E, 0) = -\frac{1}{\varepsilon(E, 0)} \tag{2.126}$$

In other words the probability

$$\eta_2(E, 0) = \frac{\varepsilon_2(E, 0)}{\varepsilon_1^2(E, 0) + \varepsilon_2^2(E, 0)} \tag{2.127}$$

is readily calculable.

This quantity differs from $\varepsilon_2(E, 0)$, which describes energy absorption from photons, in having the denominator given in Eq. (2.127). The difference is insignificant for a low-density material, e.g. a dilute gas, for which $\varepsilon_1(E, 0)$ is close to unity and $\varepsilon_2(E, 0)$ is much smaller than unity over the entire spectral range. The difference between $\varepsilon_2(E, 0)$ and $\eta_2(E, 0)$ is notable when $\varepsilon_1(E, 0)$ is comparable to, or even smaller than, $\varepsilon_2(E, 0)$. This occurs often in the valence-excitation domain of condensed matter. The difference is most conspicuous when $\varepsilon_1(E, 0) = 0$; indeed, this occurs in a metal for which $\varepsilon_1(E, 0) < 0$ at low E corresponding to intra-band transitions. Because $\varepsilon_1(E, 0)$ must generally approach unity at very high E, there is an energy at which $\varepsilon_1(E, 0)$ vanishes. Around there $\eta_2(E, 0) = 1/\varepsilon_2(E, 0)$ has a large value. This is the plasmon excitation and this case does not occur in liquid water.

2.5.2   Finite momentum transfer

Under a broad assumption of rotational invariance (which applies to our $\varepsilon(E, K)$ representing the average over spatial orientation), $\varepsilon(E, K)$ is a function of K^2 and so is

$$\eta_2(E, K) = \Im m \left(-\frac{1}{\varepsilon(E, K)}\right) \tag{2.128}$$

which determines the probability of collisions with energy transfer E and momentum transfer $\hbar K$ [20]. The above equation is often expressed in terms of the differential oscillator strength df/dE as

$$\eta_2\left(E, K\right) = \Im m\left(-\frac{1}{\varepsilon\left(E, K\right)}\right) = \frac{\pi}{2}\frac{E_p^2}{Z}\frac{1}{E}\frac{df}{dE} \tag{2.129}$$

where E_p is given in Eq. (2.118).

2.5.3   The cross section differential in energy transfer

The standard term used in physics for expressing the probability of particle collisions is the cross section σ. The mean number of collisions of a specified kind that occur during the passage of an incident particle through an infinitesimal distance dx in a material consisting of N target particles, e.g. nuclei, atoms or molecules depending on the context, per unit volume is given by $N\sigma dx$. For considerations of condensed matter it is convenient to use the product $N\sigma$ as an index of the collision probability which is called the *macroscopic cross section* in nuclear reactor physics [3] and often designated by the symbol Σ. Notice that $\Sigma = N\sigma$ has the dimension of $(\text{length})^{-1}$ and is sometimes referred to as the *inverse mean free path*. In what follows, we use Σ in the above sense and refer to it as 'cross section', dropping the adjective 'macroscopic' for brevity. Let us consider the cross section $d\Sigma = (d\Sigma/dE)dE$ for collisions of an incident particle resulting in energy transfer between E and $E + dE$ to the material. We call $d\Sigma/dE$ the cross section differential in energy transfer, i.e. the topic of the present section. Further, we consider the cross section $(d^2\Sigma/dEdK)dEdK$ for collisions of the same incident particle resulting in energy transfer between E and $E + dE$ and in momentum transfer between $\hbar K$ and $\hbar(K + dK)$. Within the FBA, it is given [19, 20] as

$$\frac{d^2\Sigma}{dEdK} = \frac{1}{\pi a_0 TK}\eta_2\left(E, K\right) \tag{2.130}$$

for an incident electron (or a proton) at nonrelativistic speed v, i.e. at kinetic energy $T = mv^2/2 \ll mc^2 = 511$ keV. Hence,

$$\frac{d\Sigma}{dE} = \frac{1}{\pi a_0 T}\int_{K_{\min}}^{K_{\max}}\eta_2\left(E, K\right)\frac{dK}{K} \tag{2.131}$$

where the integration limits are

$$K_{\min} = \frac{\sqrt{2m}}{\hbar}\left(\sqrt{T} - \sqrt{T - E}\right) \tag{2.132}$$

$$K_{\max} = \frac{\sqrt{2m}}{\hbar}\left(\sqrt{T} + \sqrt{T - E}\right) \tag{2.133}$$

for $E \ll T$ (when the Born approximation is best justified),

$$K_{\min} \approx \frac{E}{\hbar v} \qquad (2.134)$$

is small in general and approaches 0 at high T. In contrast,

$$K_{\max} \approx 2\frac{\sqrt{2mT}}{\hbar} \qquad (2.135)$$

is large and increases with T. Recognizing the above and the fact that $\eta_2(E, K)$ approaches a finite limit $\eta_2(E, 0)$ as $K \longrightarrow 0$, one readily sees that $d\Sigma/dE$ as a well characterized analytic behavior [18]

$$\frac{d\Sigma}{dE} = \frac{1}{\pi a_0 T}\left[A(E)\ln\left(\frac{T}{Ry}\right) + B(E) + O\left(\frac{E}{T}\right)\right] \qquad (2.136)$$

a form with structure similar to Eq. (2.49), where $A(E)$ and $B(E)$ are functions of E derivable from $\eta_2(E, K)$.

2.5.4 Relativistic speeds

At electron (or proton) of kinetic energies appreciable compared to the electron (proton) rest energy, the Bethe cross section formula, Eq. (2.136), needs to be modified in two respects. First, one may use relativistic kinematics to relate momentum transfer with the scattering angle and energy transfer. Second, we must account for interactions transverse to $\mathbf{K}$ in addition to the Coulomb interactions (which are longitudinal to $\mathbf{K}$) as fully discussed in [21, 20].

We report only the result that may be written as

$$\frac{d\Sigma}{dE} = \frac{1}{\pi a_0 T^*}\left[A(E)\left\{\ln\frac{\beta^2}{1-\beta^2} - \beta^2\right\} + B^*(E)\right] \qquad (2.137)$$

where $T^* \equiv mv^2/2$ (not the kinetic energy) and $\beta = v/c$. The coefficient $A(E)$ remains the same as in Eq. (2.136). This result arises because Eq. (2.134) remains true in relativistic kinematics and because the transverse interactions at low K can be expressed in terms of the dipole matrix element. The new coefficient $B^*(E)$ is related to $A(E)$ and $B(E)$ as

$$B^*(E) = B(E) + A(E)\ln\left[\left(\frac{\hbar c}{e^2}\right)^2\right] \qquad (2.138)$$

where the the *ln* term has the value 9.8405.

For further information on relativistic effects on cross sections and stopping power as well as low energy electron and proton cross section calculation a wide bibliography exists [16, 17].

2.5.5 Current PARTRAC cross sections: extension to heavy ions

Within the first order plane wave Born approximation interaction cross section for bare heavy ions of velocity v (e.g. iron ion studied in this work) are obtained from proton interaction cross sections by scaling the doubly differential cross section (differential in energy transfer W and recoil energy Q) for a proton of same velocity v by the square of the charge Z_0^2 of the ion

$$\frac{d\sigma_{ion}^2}{dW\,dQ}\,(v) = Z_0^2\,\frac{d\sigma_{proton}^2}{dW\,dQ}\,(v) \tag{2.139}$$

and as the energy decreases taking into consideration the effective charge effect previously described, that is by means of the Barkas formula

$$Z_0 \rightarrow Z^*(v)$$

A heavy ion of mass M_{ion} with kinetic energy $E_{ion} = (M_{ion}/m_p)\,E_{proton}$ has the same velocity v as a proton (mass m_p) with kinetic energy E_{proton}. This holds true for both, non relativistic and relativistic velocities.

In the PARTRAC code, proton and electron inelastic interaction cross sections are based on the non relativistic Born approximation. The DF of liquid water is modelled as a superposition of Drude like functions; parameters are adjusted to fit experimental data reported in [22]. Phase effect are considered through the DF and relativistic medium polarization effects like the Fermi effect are not currently considered in the code. It is assumed that the Fermi density effect mainly influences the cross sections at higher proton energies, say greater than 1 GeV. Currently for the study of heavy ion DNA fragmentation, such relativistic effect are not taken into account restricting ourselves in a lower energy regime (of the order of few hundreds of MeV/u), that is in the nonrelativistic regime. Implementation of the code for the extension of cross sections in the relativistic regime is under development.

2.5.6 Other cross sections and related important quantities for track structure simulations

The cross section for all collision leading to a specific product s is given by

$$\Sigma_s = \int dE \left(\frac{d\Sigma}{dE}\right) p_s\,(E) \tag{2.140}$$

where $p_s\,(E)$ is the probability of producing s upon energy transfer E. Among many quantities of interest, the first is the total cross section for inelastic scattering

$$\Sigma_{tot} = \int dE \left(\frac{d\Sigma}{dE}\right) \tag{2.141}$$

where the integral is taken over all possible values of E. The second is the cross section for the excitation of a discrete level l

$$\Sigma_l = \int dE \left(\frac{d\Sigma}{dE} \right) p_l (E) \tag{2.142}$$

where $p_l (E)$ is the probability of exciting level l upon energy transfer E. This is a sharply peaked function representing the width of the level. The third is the total cross section for ionization

$$\Sigma_{ion} = \int dE \left(\frac{d\Sigma}{dE} \right) p_{ion} (E) \tag{2.143}$$

where $p_{ion} (E)$ is the probability of producing an ion of any kind upon energy transfer E. The quantity Σ_{ion} can be further classified according to a particular ion species produced (e.g. H_2O^+, H^+ or O^+ in water).

It is also important for for track structure analysis to know the cross section for producing secondary electron of a fixed kinetic energy W. This cross section is given by

$$\frac{d\Sigma}{dW} = \int dE \left(\frac{d\Sigma}{dE} \right) \frac{dp (E, W)}{dW} \tag{2.144}$$

where $[dp (E, W) / dW] dW$ is the probability for producing secondary electrons with kinetic energies between W and $W + dW$ and includes contributions from all the electron shells.

Another quantity of importance to the Monte Carlo simulation track structure is the probability $P (E)$ that energy transfer not exceeding E occurs upon a single collision. It is defined by

$$P (E) = \frac{1}{\Sigma_{tot}} \int_{E_1}^{E} dE \left(\frac{d\Sigma}{dE} \right) \tag{2.145}$$

where the lower limit E_1 is the lowest possible excitation energy.

Finally, the mean energy loss per unit path length of an incident electron is given by

$$S = \int_0^{\infty} dE E \left(\frac{d\Sigma}{dE} \right) \tag{2.146}$$

where the integral is taken over all possible values of E.

Chapter 3

Biological effects of ionizing radiation: DNA damage

There is a strong circumstantial evidence to indicate DNA as the principal target for the biological effects of radiation, including cell killing, mutation, and carcinogenesis. A consideration of the biological effects of radiation therefore must begin logically with a description of the breaks in DNA caused by charged particles tracks and by chemical species produced by radiation.

In this Chapter we begin with a simple description of the DNA structure (far from a complete biochemical description that can be found in literature). We will describe DNA at different organization levels, from the primary and secondary structure of this macromolecule to its higher organization level in the cell nucleus, that is chromatin and chromosomes. All the DNA organization will be described again in the context of the Monte Carlo simulations (see Chapter 4), where these structrures are reproduced in the target simulation. Different types of radio-induced DNA strand breakages are described in connection with different properties of the inducing-radiation.

3.1 DNA, the principal biological target

3.1.1 The DNA primary and secondary structure

Deoxyribonucleic Acid (DNA) is a large molecule (a polymer) that most commonly occurs in nature with a well-known double helix structure. The basic features of this structure were deduced by James Watson and Francis Crick in 1953.

It consists of two strands, held togheter by hydrogen bonds between the bases. The *backbone* of each strand - *primary* structure - consists of alternating sugar and phosphate groups and the sugar involved is deoxyribose. Attached to this backbone are four bases, the sequence of which specifies the *genetic code*. The complex *base+sugar+phosphate group* is called *nucleotide*. Two of the bases are single-rings groups (pyrimidines); these are tymine (T) and cytosine (C). Two of

the bases are double-ring groups (purines); this are adenine (A) and guanine (G). The structure of a DNA strand is illustrated in Fig. 3.1.
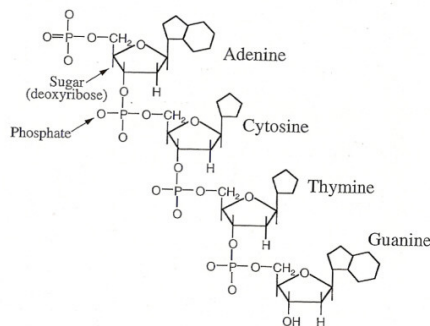
Figure 3.1: Biochemical structure of the *base+sugar+phosphate group* in a DNA strand [26].
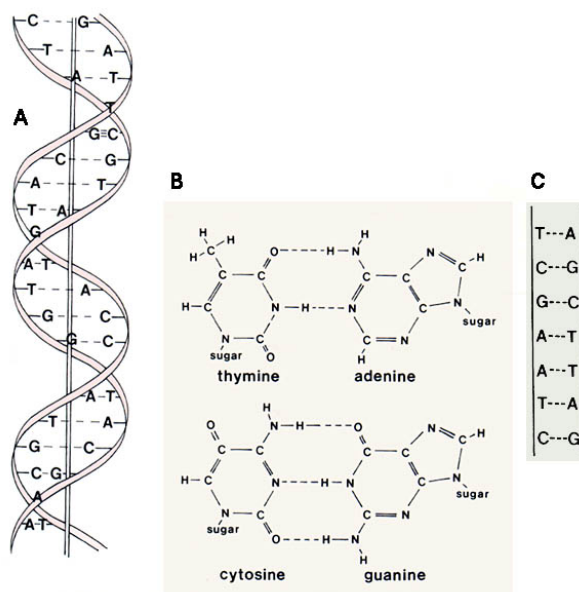
Figure 3.2: (A) Double helix structure; (B) Structure formulae and hydrogen bonds in base pairing; (C) Base pairing and complementarity [26].

Two separate chains of DNA are wound around each other following a helical (coiling) path - *secondary* structure - resulting in a right-handed double helix (or duplex). The negatively charged sugar-phosphate backbones of the molecules are on the outside, and the planar bases of each strand stack on above the other in the center of the helix. Between the backbone strands run the *major* and *minor grooves*, which also follow a helical path. The strands are joined noncovalently by hydrogen bonding between the bases on opposite strands, to form the *base pair* (bp) and the distance between the two strands is mantained regular at 2 nm. There are around 10 bp per turn in the DNA double helix. The distance between

two successive bases on the backbone is about 0.34 nm, so the helix pitch is about 3.4 nm. The two strands are oriented in opposite directions (*antiparallel*) and, most crucially, the two strands are *complementary* in terms of base sequences.

The last feature arises because the structures of these bases and the constraints of the backbone dictate that the bases hydrogen-bond to each other as purine-pyrimidine pairs wich have similar geometry and dimensions. Guanine pairs with cytosine (three H-bonds) and adenine pairs with thymine (two H-bonds). Hence, any sequence can be accomodated within a regular double-stranded DNA structure. The sequence in one strand uniquely specifies the sequence of the other, with all that implies for the mechanism of copying (or replication) of DNA and the transcription of DNA sequence. In fact, a number of different forms of nucleic acid double helix have been observed and studied, all having the basic pattern of two helically-wound antiparallel strands. The structure identified by Watson and Crick, as described above, is known as *B-DNA*, and is believed to be the idealized form of the structure adopted by virtually all DNA *in vivo*. It is characterized by a helical repeat of 10 bp/turn (although it is known that 'real' B-DNA has a repeat closer to 10.5 bp/turn), by the presence of base pairs (bp) lying on the helix axis and almost perpendicular to it, and by having well-defined, deep major and minor grooves. DNA can be induced to form an alternative helix, known as the *A-form*, under conditions of low humidity. The A-form is right-handed, like the B-form, but has a wider, more compressed structure in which the base pairs are tilted with respect to the helix axis, and actually lie off the axis. The helical repeat of the A-form is around 11 bp/turn. Although it may be that the A-form, or something close to it, is adopted by DNA in vivo under unusual circumstances, the major importance of the A-form is that it is the helix formed by RNA (ribonucleic acid) and by DNA-RNA hybrids.
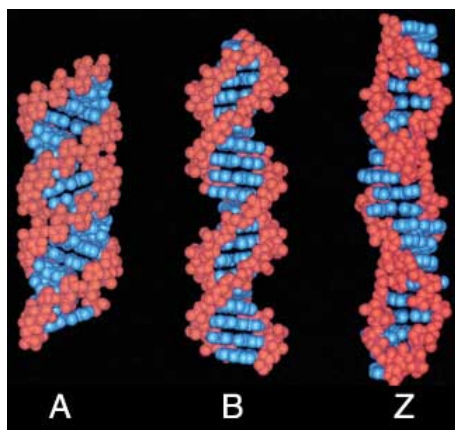

Figure 3.3: Different forms of the DNA molecules.

A furter unusual structure can be formed by DNA. The *left-handed Z-DNA* is stable in synthetic double stranded DNA consisting purely of alternating pyrimidine-purine sequences (such as CGCGCG, with the same on the other strand of course respecting complementarity). This is because in this structure, the pyrimidine and

the purine nucleotides adopt very different conformations, unlike in A-form and B-form, where each nucleotide has essentially the same conformation and immediate enviroment. The Z-helix has a zig-zag appearance, with 12 bp/turn. Z-DNA does not easily form in normal DNA, even in regions of repeating CGCGCG, since the boundaries between the left-handed Z-form and the surrounding B-form would be very unstable. Although it has its enthusiasts, the Z-form is probably not a significant feature of DNA *in vivo*.

Each organism is characterized by its own proteic constitution: enzymes and structural proteins are different from one species to the other, and are faithfully reproduced in cells of the same species. DNA is the responsible of the transmission of these ereditary characteristics.Let's see briefly how does it work.
Proteins are distinguishable for the aminoacid sequences that constitute the protein itself. Each protein is encoded on DNA by nucleotidic sequences corresponding to that of the aminoacids of that specific protein. Because there are 20 different types of aminoacids and only 4 groups of nucleotides, only one of these is not sufficient to encode only one aminoacid. There exists a precise correlation, the genomic code, between each aminoacid and a determined type of nucleotide triplet; the 4 nucleotides, taken three at a time, form 4^3 different combinations between themselves. This is enough to codify the 20 aminoacids. The characteristic nucleotide triplets of each aminoacid are called *codons*. The DNA line that contains the information for an entire protein is called *gene*. A cell able to produce thousands of different proteins has the same number of genes.

3.1.2   From DNA to chromosomes

In the mammalian cell nucleus the DNA is always bound to stable proteins called *histons*. There exist five different classes of such proteins denoted by H1, H2A, H2B, H3, H4, and others quite rare. The complex made up by an histonic octamer and DNA coiled around octamer is called *nucleosome* (see Fig. 3.4). The part of DNA that connects two nucleosomes is called *linker DNA* and has a variable lenght in the interval 10-90 bp. Nucleosomes are the elementary subunits of the *chromatin*. The latter is made up of all the DNA contained in cell nucleus, divided into long and filamentous molecules, each of one constitutes a *chromosome*. Fig. 3.5 illustrates this three-dimensional quite complex situation.

At the beginning of mitosis, the chromosomic chromatin coils with the result of an enormous condensation and in the central phases of this process (metaphase and anaphase) the cromosomes adopt the famous stick-like conformation.

3.2   Direct and indirect action of radiation on DNA

If any form of radiation is absorbed in biologic material, there is a possibility that it will interact directly with the critical target in the cell, the DNA. The atoms
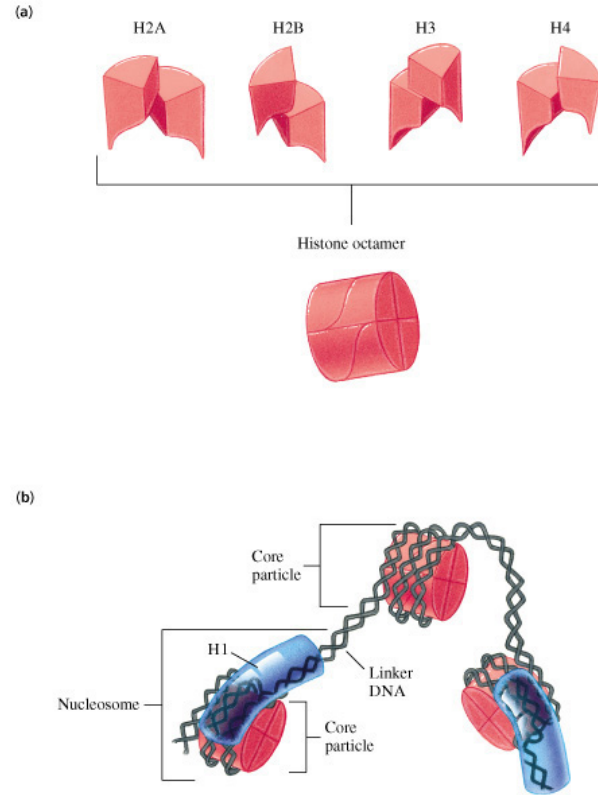
Figure 3.4: (a) Histone octamer structure and (b) *nucleosome+linker DNA* complex [26].

of the target itself may be ionized or excited, thus initiating the chain of events that leads to biological change. This is called *direct action* of radiation, and the induced damages are called *direct damages*.

Alternatively the radiation may interact with other atoms or molecules in the cell (particularly water) to produce free radicals[1] that are able to diffuse far enough to reach and damage the critical targets. This is called *indirect action* of radiation and the induced damage is called *indirect damage*.

The Monte Carlo code PARTRAC used in this work (see Chapter 4), after the simulation of physical and prechemical phase (production of ionization and chemical species) superimposes the radiation track to the biologcal structure of the target [48, 28, 29]. Here starts the analysis, with a classification of the type of damage in relation to the position where the interaction took place (in this process parameters such as energy deposited, type of interaction, and so on, are stored as output files).

The next Subsection describes such different types of damages including, for indirect damages, a brief description regarding the diffusion of chemical species in cell enviroment, an argument on which we will return in Chapter 6 in the context

---

[1]A free radical is a free (not combined) atom or molecule carrying an unpaired orbital electron in the outer shell.

Figure 3.5: Spatial structure of a chromatin filament fragment due to the nucleosomes compactification [26].

of radiation-induced non-targeted effects.

3.2.1 Direct DNA damage

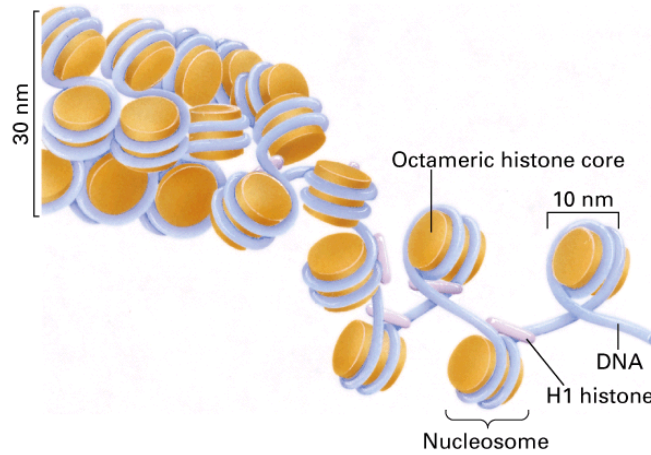In the first Chapter we described the energy depositions and track structures of different types of radiation. Now we want to to analyze the consequences of such interactions at the biological level. First, it is important to underline that intuitively the DNA damages distributions depend on the spatial distribution of energy deposition (for example in terms of event density) and on the DNA conformation and its distribution in the cell nucleus. We will see that the LET is the most important physical quantity that characterizes the radiation in terms of induced damage distribution. Studies on DNA, and in particular on the repair phenomenon have considerably extended our knowledge on molecular biology, genetics, and carcinogenesis. The most significative progresses are made up by the discovery of three principal radio-induced DNA damages: *single-strand breaks* (SSB), *double-strand breaks* (DSB), and *base dameges* (BH).

Single-strand breaks (SSB)

In general the number of SSB increases linearly with the radiation dose in a dose range quite large, say from 0.1 Gy to $6 \cdot 10^4$ Gy. The value of the eneregy requested to induce one break is about 10-20 eV. A high percentage of SSB is induced through a mechanism that involves the $\cdot OH$ water radical that reacts with sugar-phosphate causing the strand break. The repair of a SSB can be very quick and efficient. This repair mechanism begins with the removal of the nucleotidic chain containing the break, and uses the single non altered complementary strand as a *print* for the syntesis of the new chain. The process is controlled by enzymes and is temperature-dependent. The velocity of repair is exponential and generally about half of SSBs is repaired within fifteen minutes. Since a large parte of this
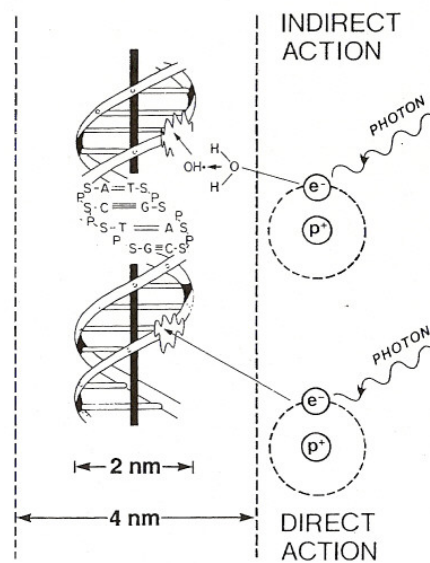
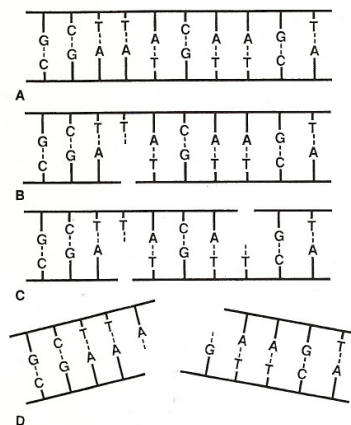Figure 3.6: Schematic view of direct and indirect action of radiation on DNA molecule [27].

Figure 3.7: Representation of DNA breackages [27]: (A) unbroken strands; (B) BH; (C) SSB; (D) DSB.

kind of breackage is repaired also in lethally irradiated cells, it is believed that SSBs are not determinant breakages for cell death with respect to more complex DNA breakages, such as DSBs.

Double-strand breaks (DSB)

DSBs are produced when two SSBs are in two opposite strands, that is on complementary strands (separated by only few base pairs, say 10 bp). In this case the piece of chromatin snaps into two pieces. A DSB is believed to be the most important lesion produced in chromosomes by radiation: the interaction of two double strand breaks may has a non-negligible probability to result in cell killing, mutation, or even carcinogenesis. There are many kinds of DSB, varying in the distance between the breaks on the two DNA strands and the kind of end groups formed. Their yield in irradiated cells is about 0.04 times that of single-strand breaks. On the relation *dose-number of DSB* induced there is not a total agreement: in most experiments there is a linear response with dose, but other studies concluded that only the first part of the curve (at very low deses) is linear and at higer doses the number of DSB increases with the $(\text{dose})^2$, and the dose-effect curve is linear quadratic

$$N_{DSB} = a + bD + cD^2 \tag{3.1}$$

where N_{DSB} is the number of DSB, D is the dose, and a, b, c are constants.

Base hits (BH)

The damage induced in the DNA bases shows a linear increase with dose, and it is believed that this damage rises through the interaction between acqueous free radicals and DNA. Neverthless, these type of damages have a very low probabilitiy to evolve to worse cellular damage.

3.2.2 Indirect DNA damage

In a complex system such as living matter the probability of ionization is larger for the molecules present in a major number. This is the case of water molecules in irradiated living material. Most of the radiaton energy is absorbed by water molecules, which constitute about the 70% of living material.

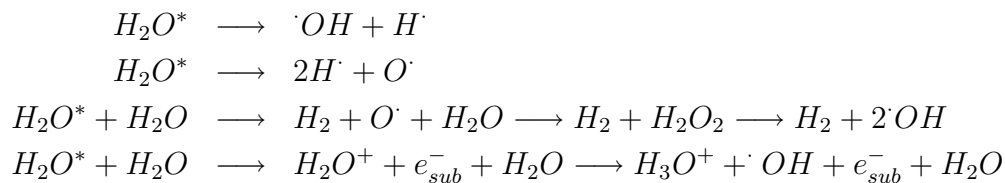For a comprehension of radiobiological effects it is extremely important to know the radiolysis of this element.

When we irradiate water, this can be ionized and the result is a free electron and a positive charged water molecule
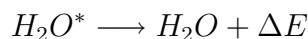
$$H_2O \longrightarrow H_2O^+ + e^-$$

Generally it is assumed that ionized water molecules react following the scheme

$$H_2O^+ + H_2O \longrightarrow H_3O^+ + {}^\cdot OH$$

while the excited molecules dissociate following

$$
\begin{aligned}
H_2O^* &\longrightarrow \ ^\cdot OH + H^\cdot \\
H_2O^* &\longrightarrow \ 2H^\cdot + O^\cdot \\
H_2O^* + H_2O &\longrightarrow \ H_2 + O^\cdot + H_2O \longrightarrow H_2 + H_2O_2 \longrightarrow H_2 + 2^\cdot OH \\
H_2O^* + H_2O &\longrightarrow \ H_2O^+ + e^-_{sub} + H_2O \longrightarrow H_3O^+ + ^\cdot OH + e^-_{sub} + H_2O
\end{aligned}
$$

Some of the excited molecules relax returning to the ground state and emitting electromagnetic energy

$$
H_2O^* \longrightarrow H_2O + \Delta E
$$

Low energy electrons (subexcitation electrons) can proceed until they are captured by another water molecule, transforming it in a negatively charged molecule

$$
e^- + H_2O \longrightarrow H_2O^-
$$
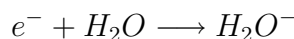
This latter process is quite slow; alternatively the electron can thermalize and become hydrated, that is surrounded by water molecules in such a way that the positive poles of the various water dipoles are oriented in line with the negative charge of the electron. This structure is quite stable at room temperature and possesses a wide absorbing spectrum, with a maximum around 720 nm. Non hydrated electrons are able to react with a wide range of solute molecules. This reactions are more probable with a high concentration of solute (0.1-1.0 M) than in more dilute solutions, where the electron hydratation is a competitive process that appears complete within 10^{-11} s.

Both H_2O^- and H_2O^+ molecules are not stable; each of these can dissociate and give an ion and a free radical

$$
\begin{aligned}
H_2O^+ &\longrightarrow \ H^+ + ^\cdot OH \\
H_2O^- &\longrightarrow \ H^\cdot + OH^-
\end{aligned}
$$
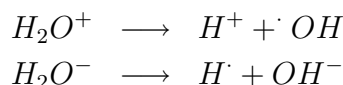
Both $^\cdot OH$ and $H^\cdot$ are highly reactive and are characterized (in absence of other reagents, or *scavengers* - see Subsection 3.2.5) by a life time of hundreds of milliseconds. However, it is probable that in tissues, where there is a high molecular density and the presence of natural scavengers, the mean-life of free radicals is shorter (of the order of microseconds or less).

The radicals can also react with each other and dimerize; the three main radical-radical interactions are the following

$$
\begin{aligned}
H^\cdot + H^\cdot &\longrightarrow \ H_2 \\
^\cdot OH + ^\cdot OH &\longrightarrow \ H_2O_2 \\
H^\cdot + ^\cdot OH &\longrightarrow \ H_2O
\end{aligned}
$$
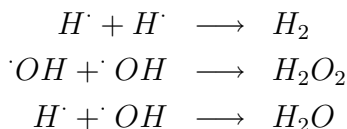
These radicals can also react with other water molecules, for example

$$H_2O + H^{\cdot} \longrightarrow H_2 + {}^{\cdot}OH$$

or radicals can react with products of their own reaction

$$H_2O_2 + {}^{\cdot}OH \longrightarrow H_2O + HO_2^{\cdot}$$

The activities and velocity constant for these reactions with molecules of various type have been experimentally determined with pulsed radiolysis techniques.

3.2.3 Diffusion and kinetics of chemical species

Between the two stages of production and reaction of chemical species, the molecules resulting from the radiolysis of water are able to diffuse in the cellular environment before they react with DNA or other molecules. The diffusion process in the chemical stage after irradiation can be described with the usual theory of diffusion processes. Generally, in Monte Carlo codes the simulation of diffusion processes of chemical species after irradiation is based on the partition of time simulation into short time steps Δt. In few words, for each Δt, known the displacement of the radical during diffusion, it is necessary to determine the direction. Usually adopted is the *random walk* assumption by which each direction is equally probable and there exists no type of correlation between the direction taken at a certain moment and the direction taken in the subsequent time step. At the end of each time step the chemical species formed in this process can interact with each other in the various modes previously listed, forming new radicals and molecules that can interact with other chemical species and DNA atoms.

3.2.4 Scavengers

One of the principal obstacles for the action of radicals are the so called *scavengers*, that is molecules that can react with free radicals instead of DNA. Most of these molecules are composed by damaged DNA fragments and protein residues after synthesis. These molecules have a chemical composition similar to that of DNA and so these fragments are able to show similar reaction rates with radicals. In this way, scavengers are able to absorb a part of the chemical impact generated by ionizing radiation, reducing the mean free path of free radicals and their mean life time.

The latter quantity is used to define the capacity of a compound to plug the free radicals action. In fact, the *scavenging capacity* (SC) is the inverse of the mean life time of radicals, and the constant $\tau = 1/SC$ is called *scavenging capacity time constant*. It is customary to associate to the quantity τ the mean life time of the ${}^{\cdot}OH$ radicals. This because it produces damages of two order of magnitude larger than other radical species. The scavenging capacity can be defined as the number of reactions per unit time between ${}^{\cdot}OH$ radical and the scavengers substrate. So,

the quantity $\tau = 1/SC$ represents the mean life time of a $\cdot OH$ radical before it reacts with a scavenger molecule.

The concept of SC allows a comparison between the effects of different scavengers. In general, some experimental studies demonstrated that the curve representing the life of radicals in cellular environment has a plunge in $10^{-10} \div 10^{-8}$ s after irradiation, and for this reason they are not able to travel a distance longer than 4-5 nm. These results are extremely important for the implementation of Monte Carlo codes because they allow us to restrict the number of radicals to be monitored after their generation, that is less time spent for computer calculations. In Chapter 4 we will see that the concept of scavenger and scavenging capacity can be extended to the different structural properties of DNA conformation.

3.3 Damage repair mechanisms

The cell possesses different mechanisms from DNA breakage. This occurs also because DNA is affected by continuous endogenous damaging reactions like oxidations, metilations, protein errors, and so on. For this reason, the cell has developed defence and repair mechanisms against the endogenous damaging agents and exogenous agents like ionizing radiation.

The simplest case is the mechanism of chemical repair where the ionized molecule has the possibility to capture the missing electron leak from the substrate and to reform the broken bond. This kind of repair is surely the most immediate type of recombination. However, frequently it is necessary the help of some appropriate proteic structures. The SSBs are repaired by enzymes called ligases. These enzymes are able to reattach the chain using the intact complementary chain as a print. However, there are phenomena like the ”oxygen effect” that can induce a delay or a total stop in the repair mechanism. In this case biomolecular oxygen can bind to one extreme of the broken chain and inhibits the reconnection with the correct extreme. In the case of two or more close SSBs on the same chain (this is the case of a probable loss of a DNA fragment), the polymerase and ligase proteins reconstruct the chain together and reconnect the extremes of the chain. In the case of DSBs the repair is more complicated. Sometimes it happens that it is not possible to recover the lost fragment and the missing structure is reconstructed. Sometimes this reconstruction is not possible or there is a lack of information necessary to the correct continuation of the genetic code. In some cases the repair mechanism forces the synthesis of new nucleotides that lead to errors. This also happens when there is the junction of incorrect fragments, for example following chromosome aberrations.

3.4 Radiation genetic effects: chromosome aberrations

In interphasic chromosomes the chromatin fiber (diameter about 25 - 30 nm) forms a more or less regular tangle composed by a large number of loops. This originates domains with linear dimensions of the order of a few microns. When a chromosome is damaged in one of the phases of cell life, it is possible that there is a creation of wrong recombination of the genetic material. These alterations of chromosome structures that brings to a different distribution or to a different arrangement of the hereditary information stored in the genetic code are called *chromosome aberrations*. Furthermore, some of the acquired alteration have the properties to be transmitted to daughter cells and to repeat themselves with the same characteristics (if compatible with cell life). A typical example is given by translocations, which are particular aberrations produced by two breaks on two distinct chromosomes. Translocations are strongly correlated with some types of tumor, in particular leukemia.

Chromosome aberrations and genetic code mutations constitute one of the main aspects of the harmful effects of ionizing radiation at cellular level.

It is possible to divide chromosome aberrations into two main classes

- simple chromosome exchanges, which involve two breaks upon two chromosomes;

- complex chromosome exchages, which involve three or more breaks upon two or more different chromosomes.

Chapter 4

The PARTRAC code: target and DNA damage simulation by USX and protons

In the previous Chapters we explained why mean quantities such as absorbed dose an LET are not able to explain in a detailed way the stochastic aspects of physical, chemical, and biological effects of the different types of radiation. Track structure theory gives more information on the spatial and temporal aspects following irradiation, and at the same time these theories need, as input, the knowledge of the cross sections relative to the physical processes described in Chapters 1 and 2. All stages of the radiation action are stochastic in nature, therefore mechanistic models, possibly applied as Monte Carlo simulations, can be of great help for a better understanding of the various steps of radiobiological damage induction. Such models mainly rely on the knowledge of track structure features and geometrical and biochemical properties of the target. Indeed, one of the main problems concerning the present status of radiobiological damage modeling is that different approaches can, in principle, lead to equally acceptable results, thus making it difficult to identify and reject erroneous working hypotheses. These kinds of problems are emphasized by the fact that several orders of magnitude, both in the time and in the space scale, are involved in the induction of radiobiological damage. Moreover, mechanisms involved at different levels are strictly interrelated, thus implying that the uncertainties in a certain step of the process can propagate in subsequent steps, and as a consequence, acceptable approximations might *evolve*, leading to unacceptable uncertainties in the final results. The recent improvement of physicochemical cross-sections in track-structure simulations and of geometrical models of the DNA and chromatin structure makes it possible to test separately different assumptions on the mechanisms, leading from the initial radiation insult to the induction of certain endpoints. It is therefore of utmost importance to develop models capable of describing each single step of the process of interest in a testable way, so that contributions from distinct mechanisms to the same

endpoint can be identified and uncoupled. The basic idea of the models regarding the interaction between radiation and biological matter is the assumption that the knowledge of the initial energy depositions (spatial and temporal coordinates, interaction types, deposited energies, and produced species) is the key for the comprehension of the various biological end-points like cellular inactivation and chromosome aberrations induction. In this research work we used the biophysical Monte Carlo code PARTRAC, developed in collaboration with the *GSF Institute* of Munich; it constitutes the evolution of the codes MOCA 8 (electron transport code) and MOCA 14 - MOCA 15 (protons and Helium ions transport code).

With the current PARTRAC code version it is possible to simulate electron and photon tracks with energy in the range 10 eV-100 MeV, and proton and heavier ions tracks with an energy per nucleon in the the non relativistic regime.

These powerful techniques are used to simulate the enormous number of physical processes that happen during irradiation. Starting from the physics of matter-radiation interactions, this code allows us to reproduce and study the consequences and the effects of various types of radiation. Some of the avaiable codes are only able to reproduce the physical stage of irradiation, while others, like PARTRAC code, are able to simulate various stages starting from the physical one (following the primary and secondary particle energy deposition) to the chemical stage where the diffusion of radical species produced in the irradiated medium is simulated.

This code also provides a detailed (atom-by-atom) description of the DNA and chromatin structures, thus making it possible to test working hypotheses on the radiation action mechanisms in a quantitative way and to perform extrapolations safer than hitherto possible to parameter regions where no experimental data exist (e.g., at low doses). In previous works [28, 29, 32], PARTRAC has been used to model the spectra of various types of DNA damage induced by different radiation fields. In this work we used the PARTRAC code in two different studies on radiation-induced DNA damage. The first one is presented in this Chapter and is focussed on the role of DNA/chromatin organization and scavenging capacity in Ultra Soft X-Ray (USX) and proton induced DNA damages. The second one is presented in Chapter 5 and is focused on the study of DNA damage induction - DNA fragmentation - by heavy ions also in the context of astronauts' exposure to Galactic Cosmic Rays during long term space missions.

4.1 Main stages of radiation track structure evolution

The evolution of track structure up to 10^{-6} s after irradiation is usually divided into three main stages. The "*physical*" stage, which can be considered completed at 10^{-15} s after irradiation, produces a primary spatial distribution of excited and ionized molecules and of subexcitation electrons, whose energy is lower than the first electronic excitation level of the target molecules. When modeling the physical stage, one needs to know the differential cross-sections for all possible

interactions capable of inducing chemical modifications in the target. Ionized and excited molecules (at present most codes deal with water molecules only) relax, auto-ionize or dissociate during the "*physicochemical*" (or "*prechemical*") stage (from 10^{-15} to 10^{-12} s after irradiation), whereas subexcitation electrons either recombine, or thermalize and become solvated. Modeling the prechemical stage requires knowledge of the probability of each dissociation mode associated with the different excited states of the water molecules, the initial relative distances among the dissociation products, and the distance traveled by subexcitation electrons before they thermalize or recombine. During the "*chemical*" stage (from 10^{-12} to 10^{-6} s after irradiation, when an intratrack equilibrium is reached) the various species diffuse and react among themselves, or they can attack cellular constituents such as the DNA. For modeling the chemical stage, one needs to know the diffusion coefficient of each species, the reaction rate constants between each pair of species, and the reaction probability of each species with the different cellular constituents. With the objective of investigating the radiation damage to the DNA, the interaction probability of (mainly) the $\cdot OH$ radical with DNA nucleotides and sugar-phosphate moieties needs to be known. Early attempts to develop stochastic models of diffusion and interaction of chemical species date back mainly to the 1980s. Many different groups have since then progressively refined such models, attaining very high levels of detail.

4.2 The structure of the PARTRAC code

The PARTRAC code used in this work is structured in *modules* that act sequentially using as input the output files generated by the previous module. These modules are (in order of action)

- *ptrac* (for photons); *protrac* (for protons); *hiontrac* (for Helium ios, recently modified also for heavier ions)

- *etrac* (for electrons, primary or secondary)

- *dnahit*

- *chemie*

- *damcheninfn*

- *chromtracks*

The first two modules (etrac after ptrac for seconday electrons, protrac or hiontrac) simulate the physical stage of the energy release by primary particles in liquid water (the medium) and the interaction stage of the produced secondary particles (electrons). In this way these modules terminate the construction of the physical tracks. This physical stage ends about 10^{-15} s after irradiation.
In the output files of the PARTRAC physical modules it is possible to check

which primary particle has interacted, and at the same time the code also follows and processes the first and higher generation electrons. Via the output files, it is possible to know which was the type of interaction and the energy deposited where the interaction took place; besides the spatial coordinates of the event, it is possible to check the hit chromosome, the genomic position (in terms of base pairs), and the atom of the specific hit nucleotide.

The fundamental object for the study of radiation effect is the target and its structure inside the cell nucleus. One of the most important features of the code is the use of geometric algorithms that allow to describe and build the principal target at different organization levels starting from single atom that constitute the DNA double helix to chromosome territories of cell nucleus (see next Section). Fig. 4.1 gives an example of the output file of the physical stage.

```
2323   10.79  -2847.33  1892.18 -1311.05 5  231173   80971 -1773    5
2323   13.39  -2847.41  1892.26 -1310.96 5  231173   80970 -1773    5
2323   10.79  -2847.42  1892.28 -1310.94 5  231173   80970 -1773    5
2323   13.39  -2847.49  1892.35 -1310.86 5  231173   80972 -1773    5
2323   16.05  -2847.87  1892.75 -1310.42 5  231173   80948 -1773    5
2323   10.93  -2847.72  1893.02 -1312.63 5  231173   81297 -1778    5
2323    6.62  -2848.45  1896.32 -1303.78 5  231173  105184 -2154    5
2323   10.20  -2852.02  1894.91 -1309.70 5  231173  146104 -2798    5
2323   10.79  -2852.21  1895.06 -1309.80 5  231173  146098 -2798    5
2323    9.86  -2855.75  1876.99 -1305.07 5  231173     159   501    5
2323    2.61  -2851.92  1895.93 -1310.02 5  231173  145948  2795    5
2323    2.09  -2849.35  1891.33 -1305.81 5  231173  109511  2222    5
2323   16.05  -2851.50  1896.58 -1306.17 5  231173  141457 -2725    5
```

Figure 4.1: Example of output file from the physics module of PARTRAC.

In the first column we can read the number that identifies the primary incident particle; in the second one there is the deposited energy in eV; the three successive columns give the three spatial coordinates (x, y, z) of the interaction event; the sixth column gives the identification number of the hit chromosome; columns seven and eight give the number that identifies the hit box[1] and hit atom respectively; the ninth column gives the genomic coordinate and the last column gives the identification number of the region where the interaction took place (number 5 indicates the cell nucleus region; Section 4.5).

The third module *dnahit* simulates the prechemical phase of the process (starting from 10^{-15} s to 10^{-12} s after irradiation). In this phase the excited and ionized water molecules dissociate, relax and autoionize, while the electrons produced by ionizations recombine or thermalize (that is, they reach thermal energies $E = kT$, where k is the Boltzmann constant and T the absolute temperature of the medium) and become "aqueous electrons", that is surrounded by a cloud of water molecules bound by ion-dipole interaction.

The dissociation schemes for water molecules are not yet determined experimentally in a quite reliable manner. In general different simulation codes use different values for the relative probabilities of the different dissociation modes. Table 4.1 shows the different dissociation schemes used in this work.

---

[1]See next Section for the definition of box.

Excitation	Decay Channel	Relative probabilities
A^1B_1	$H_2O + \Delta E$	35%
	$H^\cdot + {}^\cdot OH$	65%
	$H_2 + O$	-
B^1A_1	$H_2O + \Delta E$	23%
	$H_3O^+ + {}^\cdot OH + e_{aq}^-$	50%
	$H^\cdot + {}^\cdot OH$	20%
	$2H^\cdot + O$	3.9%
	$H_2 + O$	
	$H_2 + H_2O_2$	3.2
Ry,db,de	$H_2O + \Delta E$	50%
	$H^\cdot + {}^\cdot OH$	-
	$H_3O^+ + {}^\cdot OH + e_{aq}^-$	50%

Table 4.1: Dissociation schemes and their relative probabilities adopted in this work.

	Diffusion coefficient, $D\,[10^{-9}m^2s^{-1}]$
e_{aq}	4.5
${}^\cdot OH$	2.8
$H^\cdot$	7.0
H_3O	9.0
H_2	4.8
OH^-	5.0
H_2O_2	2.3

Table 4.2: Diffusion coefficient values (10^{-9} m^{2}s^{-1}) adopted in this work.

The PARTRAC code, after the simulation of the prechemical phase (that is ionization and chemical species production), superimposes the radiation track to the biological structure (see Fig. 4.2) of the target [48, 29, 49], classifying the type of damage according to the position where the interaction took place. If the position of the interaction coincides with an atom of the DNA molecule, the damage is classified as direct and then is analyzed by the fifth module; if the interaction occurred in coincidence with the position of a water molecule, the radiolysis process simulation begins with the diffusion and interaction of free radicals and other chemical species, whose interaction is analyzed by the following module.

The fourth module (*chemie*) simulates the chemical phase: the products of the previous stages diffuse and react, both between each other and DNA; in particular, radicals like ${}^\cdot OH$ and e_{aq}^- can directly attack the DNA. To be able to simulate these processes, the PARTRAC code has input files containing information such as reaction constants and diffusion coefficients of the chemical species described above. Tables 4.2 and 4.3 show the values of some parameters used in PARTRAC for this work. The fifth module (*damcheninfn*) receives the data from the previ-
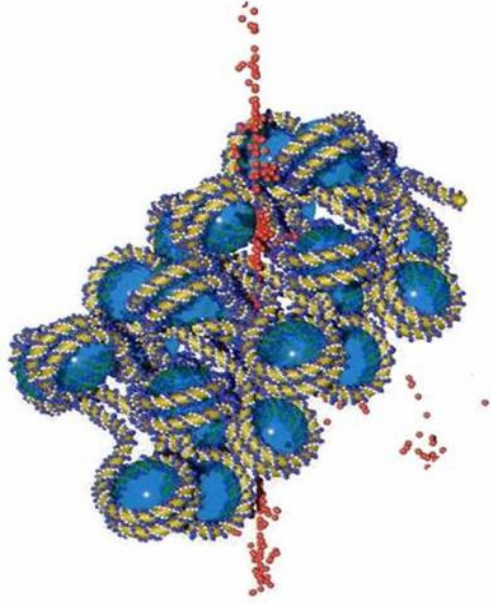
Figure 4.2: Charged particle track superimposed on a chromatin fragment [28, 29].

Reaction	Reaction constant
$e_{aq} + e_{aq} + 2H_2O \rightarrow H_2 + 2OH^-$	0.50
$e_{aq} + \cdot OH \rightarrow OH^-$	3.0
$e_{aq} + H\cdot + H_2O \rightarrow H_2 + OH^-$	2.5
$e_{aq} + H_3O^+ \rightarrow H\cdot + H_2O$	2.3
$e_{aq} + H_2O_2 \rightarrow OH + \cdot OH$	1.1
$\cdot OH + \cdot OH \rightarrow H_2O_2$	0.44
$\cdot OH + H\cdot \rightarrow H_2O$	1.44
$H\cdot + H\cdot \rightarrow H_2$	1.0
$H_3O^+ + OH^- \rightarrow 2H_2O$	14.3

Table 4.3: Reaction constant adopted in this work.

ous modules and classifies the damages using a procedure and the definitions of damage previously described.

4.3 Simulation of the DNA target model

4.3.1 DNA helix and nucleosomes

The DNA target model that has been developed includes six levels of DNA organization (deoxynucleotide pair, double helix, nucleosome, chromatin fiber structure, chromatin fiber loop, and chromosome territories) and the model completely reproduces the human genome (about $6 \cdot 10^9$ bp). Deoxynucleotide pairs are stacked in either a preselected or a random sequence with a $z-$shift of 0.3375 nm and a

90

helical turn of 36°, yielding a linear double helix in B-DNA form. The coordinates of the atoms of the deoxynucleotides are taken from [30], and the van der Waals radii (P: 0.19 nm, C: 0.17 nm, N: 0.15 nm, O: 0.14 nm. H: 0.12 nm) are from [31]. In the simulation of higher-order structures, the atomic positions are applied to a local Cartesian coordinate system moving along the DNA axis with its helical rotation and subsequently transformed to a Cartesian coordinate system in which the chromatin fiber axis is coincident with the z axis. The helical rotation of the moving coordinate system is varied slightly to fit the ends of the helices seamless when the modeled nucleosomes are stacked together. The simulation of the nucleosome core particle is based on the model reported in [33]. The core particle comprises 146 nucleotide pairs of a DNA helix wrapped in a left-handed superhelix 1.8 times around a histone octamer, which is represented geometrically by a cylinder with a diameter of 6.4 nm and a height of 6 nm. The radius of the axis of the superhelix is taken to be 4.4 nm. Thus the radius of about 1.1 nm for the DNA helix results in a total diameter of 11 nm for the core particle. The pitch is 2.7 nm per turn. A hydration shell is implicitly modeled by increasing the van der Waals radius of all DNA atoms by a factor of two. No further DNA environment (e.g. the stabilizing Na ions) is included in the model.
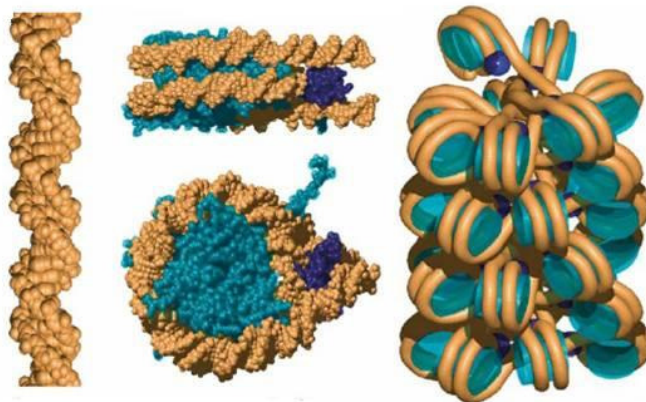

Figure 4.3: Built of chromatin fiber (right) starting from the DNA duplex (left) [28].

4.3.2 Chromatin fiber structure

The position and the orientation of each nucleosome core particle in a chromatin fiber are determined by three cylindrical coordinates describing the position of the nucleosome center and three angles describing the orientation of the nucleosomes with respect to the fiber axis. In the input data set of the model, the outer radius of the chromatin fiber, the angle and the shift along the z axis between succeeding nucleosomes are given. These data are constant for regular arrangements of nucleosomes since the positions of two succeeding nucleosomes relative to one another

and their interconnections are repeated identically.

For the determination of the position and orientation of the linker DNA, the number of deoxynucleotide pairs between succeeding nucleosome core particles is an additional input of the model. The linker length must be selected as not below a minimum number of base pairs corresponding to the shortest connection. On the other hand, to avoid major bending of the DNA helix, the linker length must be chosen as not much higher than this minimum value, especially for short interconnections. Finally, the number or nucleosomes per chromatin fiber element must be specified. The last nucleosome in a fiber element must allow for a seamless connection with the first nucleosome or an identical element stacked on top of the other element. This number or nucleosomes multiplied by the angle between them corresponds to the number of turns around the fiber axis per fiber element.

For a description of stochastic structures of the chromatin fiber, it is necessary to permit some variation of one or more parameters of the model. To generate a stochastic fiber, the position and orientation of each core particle are determined with random selection of variable parameters according to their ranges. The core particle is accepted if a sufficient smooth linker DNA connection with the former core panicle is found and no overlap occurs of the DNA helix with itself or with the histone cylinders previously positioned. If this is not achieved within a large number of trials, the formerly accepted core particles are rearranged. If only the final connection between the last core particle and the first one of a stacked fiber element is not met. the first nucleosome of the chain is discarded and the position of the last nucleosome for which all conditions are fulfilled is sought. This procedure is continued until all nucleosomes inside a fiber element are positioned and connected smoothly without overlap, or until no solution is found for the given set of parameters within a specified time. In the calculation of the stochastic fiber structure given below, more than 200.000 nucleosome core particles had to be positioned and tested. Geometrical input parameters describe three regular fiber structures with *solenoidal*, *crossed-linker* and *zigzag* formation and one *stochastic* structure. The parameters used for the three condensed formations are compatible with the structure of the 300 $\mathring{A}$ chromatin filament described in [34], apart from the orientation of the nucleosomes in the stochastic fiber for which a greater angular range was permitted in the model. Correspondingly, the zigzag model is in accord with the 100 $\mathring{A}$ nucleosome filament structure [34]. In Fig. 4.4, an illustration of the zigzag model of a chromatin fiber is given by spheres with single van der Waals radii of all atoms of the DNA and cylinders describing the histones. In Fig. 4.5, the three types of condensed fibers are displayed in a top and a side view. The solenoidal structure is similar to that which was used in [36]; however, the linker DNA is somewhat longer and thus comes closer together in the center of the fiber (the figures were generated by the Persistence of Vision$^{\text{TM}}$ Ray-tracer (POV-Ray$^{\text{TM}}$) software package). The straight chromatin fiber structure can be divided into linear chromatin fiber "boxes" consisting of all atoms with a $z-$coordinate along the fiber between 0 and the repeat length of the fiber. For the construction of looped chromatin fibers, two curved chromatin fiber boxes are
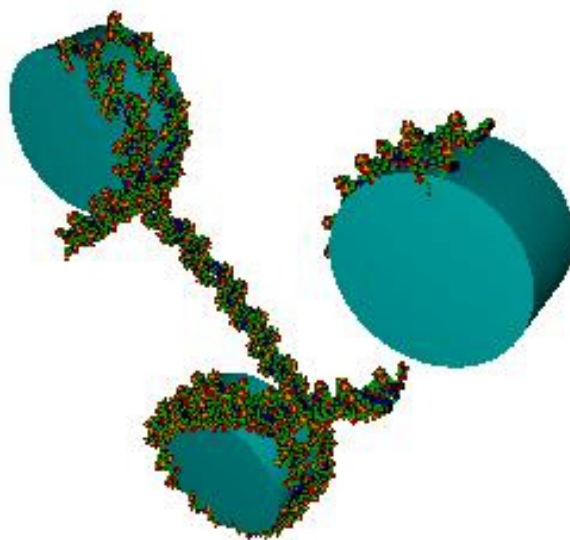
Figure 4.4: Chromatin fiber with zigzag structure (the cylinders represent histones) [28].

introduced in which the axis of the linear box is changed to an arc of a circle to the left and to the right, and the cylindrical shape is altered into two torus sectors with all atomic coordinates inside the cylinder transformed. The three types of boxes can be stacked with smooth interconnections of the DNA helices at their borders. Since the repeat Iengths differ noticeably for the fiber structures considered, the bending angles of the curved elements are chosen to be about proportional to the box height which yields similar fiber curvatures of about 65 nm radius. Flat chromatin fiber loops with comparable sizes were constructed for the four fiber structures by stacking linear and curved boxes together in a selected sequence. The fiber loop with crossed-linker structure is displayed in Fig. 4.6.

The advantage of this loop model is that the same atoms are found in each of the three boxes, and one coordinate of these atoms remains unchanged upon the transformation which reduces storage space and simplifies starting algorithms. Its limitations, however, are that the model describes only flat loops, that the cylindrical shape of the histones is distorted in the curved dements, that the distortion of the nucleosomes in the curved elements is unpleasant and unrealistic, and that the method is not capable of describing tight bends in the chromatin fiber (further work is in progress to remove these limitations).

4.3.3 Chromatin fiber loops

In the present implementation of this DNA target model in PARTRAC, the entire DNA in the nucleus of a human cell is modeled by small identical chromatin fiber loops. These loops are considered to be distributed randomly and oriented randomly inside a cylinder describing the cell nucleus. To cope with such an amount of data, the spatial information about the DNA is separated into two sets of data arrays. The first data set describes the fiber structure with all DNA atoms in the
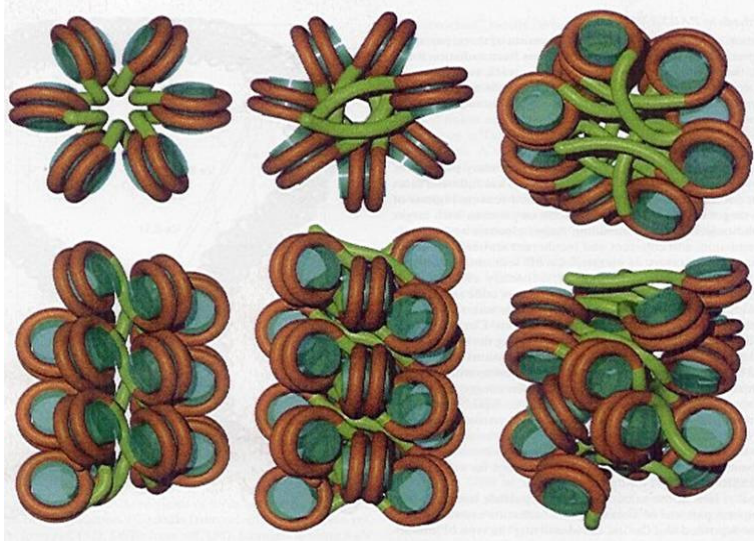
Figure 4.5: From left to right: condensed chromatin fibers with solenoidal, crossed-linker and stochastic structures [28].

chromatin fiber boxes including Cartesian coordinates in the three types of fiber elements described above, indices of atoms, deoxynucleotide pairs and strands. The second data set describes all chromatin fiber loops by the origin, the direction of the axis and a polar angle of the first box in the fiber. The origin is chosen randomly inside the nucleus with random direction of the axis and random polar angle. A particular selection is discarded if parts of the loop are found outside the nucleus. Presently the fact that some of the chromatin fiber loops overlap with each other is not taken into account. However, the overlapping volume is less than 0.1% of the total DNA volume of each chromatin fiber structure, and thus its influence on the results is negligible. The amount of computer memory needed for implementation of the DNA target model is in the range of 100 MB. Some effort was necessary to limit the computing times to an acceptable level. Besides sorting of both databases, this was achieved by a hierarchical test sequence for spatial coincidences and by using lists of possibly hit chromatin fiber loops for all events within a distance of 5 nm.

4.3.4 Chromosomic territories

In order to simulate human chromosomes with a territorial organisation, the total volume of the cell nucleus is divided into 46 domains with a volume corresponding to the real size of the chromosomes. These chromosomal domains are defined on a regular grid of $101 \times 101 \times 101$ cubic elements, each with a side length of 130 nm, forming a cube surrounding the cell nucleus. Only those grid elements which are totally inside the spherical cell nucleus were included in the following procedure. The algorithm starts with 42 elements near the surface and 4 elements in the central region of the nucleus which are the first assigned elements of each chromosome. The free elements around these assigned elements are marked as

Figure 4.6: Chromatin fiber loop with crossed-linker structure [28].

border elements of the domains. The next assigned element of each domain is selected randomly from the border elements with the highest number of neighboring assigned elements. This growth of domains is carried out element by element proportional to their volume. If the number of border elements around a domain happens to be short in relation to the number of missing elements of the domain, then adjacent border elements or even adjacent assigned elements from neighboring domains are redistributed. The procedure is finished when 95% of the grid elements are assigned to domains since the algorithm then starts to produce frayed borders. The total number of chromatin fibre loops is distributed to the 46 chromosomes proportional to their size, and the construction of connected fibre loops is limited to the volume of the grid elements assigned to the domain of the chromosome actually under construction, until the generation of the next chromosome starts at a corresponding grid element.

4.4 General methods of simulation for the present work

In the previous Sections we showed which are the four possible structures used by the code to construct the chromatin fiber. In particular in this work, the geometry module for the generation of the target organizes the nucleosomes in the crossed-
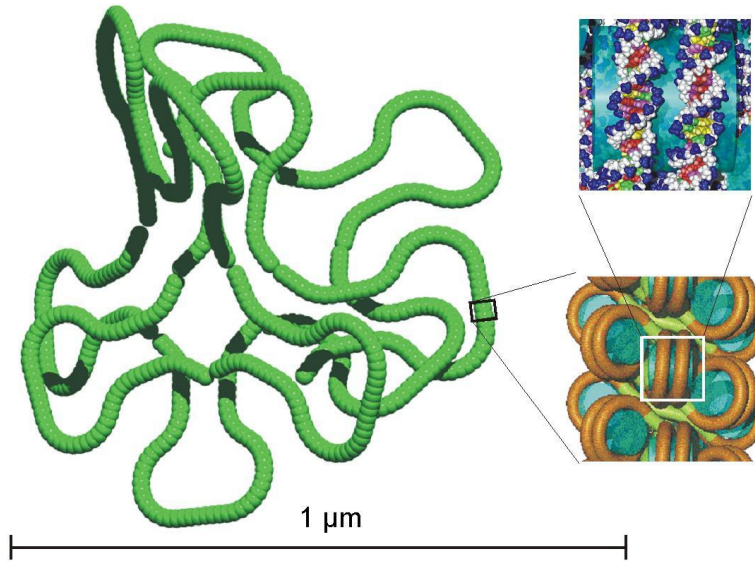
Figure 4.7: DNA fragment of 1 Mbp length represented by 11 interconnected chromatin fiber loops of 91 kbp including illustrations of the crossed-linker fiber structure (bottom right) and the atomic structure of the DNA helix (top right) [28].

linker structure, with a mean angle of 150° between subsequent nucleosomes and a mean radial distance of 11 nm between the center of the histone and fiber axis. To represent the cell nucleus a cylinder with base radius of 6 μm and height 5 μm has been used; the cell has always the form of a cylinder with base radius of 9 μm and 6 μm height. The cell lies on a cylindrical mylar thickness (see Fig. 4.12) with base radius of 10 μm and 1 μm height. For the cell and nucleus it has been assumed a density value of 1.06 g/cm^3. The radiation beams have been always taken to be parallel between themselves and to the $z-$axis of the Cartesian system fixed origin, while the radiation source has been chosen both in extended form and pointlike form according to the type of simulation in study.

The sequence of ionization and excitation events has been simulated until the energy of the secondary electron falls below 10 eV. The remaining energy has been assumed to be locally absorbed. A simulation proceeds until a certain energy, fixed as input, has been released in the cell nucleus for a fixed number of times. With the dimensions previously fixed for the cell and nucleus, for example a release of a dose of 1 Gy in the cell corresponds to an energy of about 3531 keV that has to be released in the nucleus, as can be verified with the expression
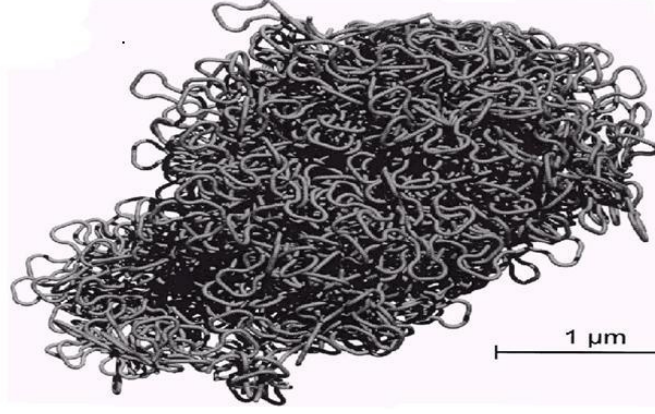
Figure 4.8: DNA fragment of 100 Mbp length (corresponding approximately to the size of human chromosome 15 simulated by 1100 interconnected chromatin fiber loops [28].

$$D\,[Gy] = \frac{E\,[eV] \times 1.6 \cdot 10^{-19}}{d\,[kg/m^3] \times V\,[m^3]}$$

where

D = dose in Gray
E = energy (eV) released in the cell nucleus
d = density of cell nucleus in kg/m³
V = nucleus volume

which gives the energy released by radiation in the cell once the dose is chosen.

In the past, two parameters of the model, precisely the energy necessary to create a SSB and the distance between two SSBs that constitutes one DSB, have been fixed to look for an agreement with measures done in experiments with human fibroblasts using X-Rays.

In the previous versions of the PARTRAC code, it has been assumed that an SSB were the result of an energy deposition larger that 17.5 eV on the sugar-phosphate backbone [37]. The weak point of this assumption is the use of a fixed mean value, with a step behaviour, to describe a stochastic process where multiple factors with different probabilities occur. For this reason the conclusion was that a theshold energy exists but the probability of SSB induction grows linearly from 0 to 1 for energy depositions in the range [5 eV;37.5 eV], remaining equal to 1 for larger energy depositions.

For what concerns the other parameter, it has been assumed that one DSB is formed by two SSBs (each of one on different chains) within ten base pairs. Moreover, two SSBs on the same chain, at a distance ≤2 bp (1 bp=0.34 nm), are considered as a single SSB. The production of DSBs from two SSBs that originate from distinct tracks has been assumed to be negligible, because their contribution is less than 1%, also with very high doses (e.g., 1000 Gy).
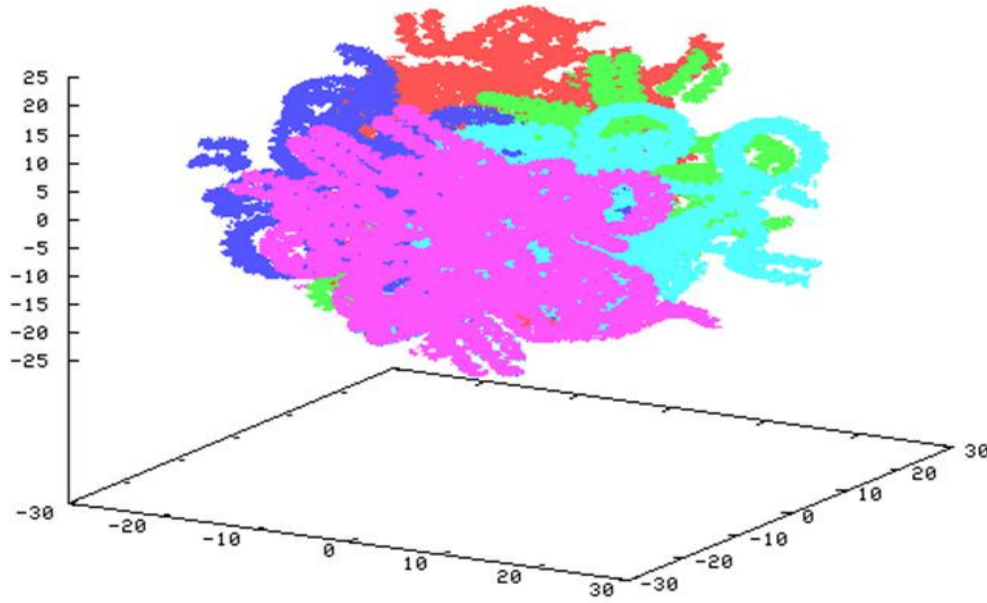
97

Figure 4.9: Partrac simulation of chromatin inside cell nucleus; the different sections of different colour correspond to 5 element (5 input files) whose union constitutes the whole human genome.

Because of the DSBs weak capability in explaining the dependence of biological end-points on LET and radiation quality, a further parameter has been introduced with the scope to identify a class of initial lesions that can be determinant for damage evolution at chromosomal and cellular level. *Complex lesions* (CL) have been defined in [38], and these are composed by two or more SSBs on each chain within 30bp. The introduction of CL has been proposed for a qualitative and quantitative description of cluster lesions generated in particular by high-LET and densely ionizing radiation.

4.4.1   Irradiation geometry

In this work the cell and its nucleus are simulated by cylinders. In the geometry input file it is possible to modify the coordinates of the center of the bases, the radii, and the cylinder heights. The overall target geometry is completed with a cylindrical mylar thickness where the cell leans and the source of the particle beam. The latter is normally of wide dimensions (and the impinging particles start from random points on its surface), but it can be made pointlike to simulate particular irradiation conditions.

A typical situation is illustrated in Fig. 4.10 where the numerical labels indicate: $1 - 2 \Longrightarrow$ vacuum; $3 \Longrightarrow$ mylar; $4 \Longrightarrow$ cytoplasm; $5 \Longrightarrow$ cell nucleus.
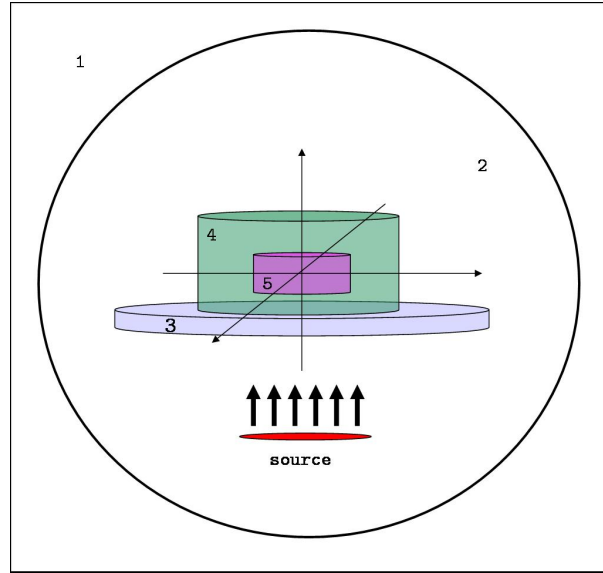
98

Figure 4.10: Scheme of irradiation conditions with the PARTRAC code.

4.5 Role of DNA/chromatin organization and scavenging capacity for USX and protons

Among the effects of ionizing radiation, DNA strand breakage is widely recognized as a major initial damage. Correlated with cell death and carcinogenesis [39, 40, 41], double-strand breaks (DSB) are crucial lesions in the processes leading to gene mutations and chromosome aberrations. The pathway complexity leading to radiation induced DNA strand breaks has not yet been fully clarified. However, the general opinion is that a single-strand break (SSB) can be produced both by a direct energy deposition in the sugar-phosphate moiety ('direct' effect) and by DNA-water radical interaction ('indirect' effect), generally an $^{\cdot}OH$. Previous studies (both theoretical and experimental) on radiation-induced DNA damage indicate that the induction of SSB and DSB is generally *linear with dose*. The absolute yields per unit dose and DNA mass (usually expressed as SSB/Gy/Da and DSB/Gy/Da), show a significant dependence on factors such as radiation quality, the level of DNA higher-order organization and DNA environment scavenging capacity [42]. Monte Carlo simulation codes are of great help in clarifying the complexity of such damage induction and the role of the different factors mentioned above. One of the main feature of these codes is to allow the study of DNA damage induction through the possibility of varying the contributions of the different modulating factors. This work is an extension of a previous work [42] similarly focused on the role of $^{\cdot}OH$ scavengers and DNA higher-order structure, where gamma-radiation induction of damage was studied through simulations. In this work, the extension is made simulating USX- and proton- radiation-induced damage with different energies for different levels of scavenging capacity but with the same DNA high-order structures, in order to quantify the role of radiation quality

99

on damage induction. Spatial distributions of energy depositions were superimposed on the various structures, and energy depositions in the sugar-phosphate were considered as potential (direct) SSB. The production, diffusion and reaction of chemical species were explicitly simulated with the "chemical module" (previously applied to simulation of liquid water radiolysis [43]. According to [44], in the chemical stage of simulations, we assumed that the 13% of the interactions between $\cdot OH$ and DNA lead to a SSB. Consequently, because the reactions of $\cdot OH$-radicals with the sugar-phosphate represent about the 20% of all the interactions with DNA, here it was assumed that an $\cdot OH$-sugar-phosphate interaction leads to "indirect" SSB with a probability of 65%. Two SSB on opposite strands within 10 base-pairs were considered as a DSB. Induction of SSB and DSB following irradiation with USX or protons with different DNA target structures was also quantified as a function of $\cdot OH$ mean lifetime (τ). The quantity τ^{-1} provides the number of reactions of a $\cdot OH$ radical with other molecules than DNA or histones per unit time. Assuming $\cdot OH$ radical as the main contributor to DNA strand breakage, the quantity τ^{-1} identifies the scavenging capacity of DNA environment ('environment scavenging capacity', SC). Both for USX and for protons, the calculated damage yields decreased by increasing the SC for the three considered target types. Such decrease can be ascribed to the competition between the reactions radical-DNA and $\cdot OH$-scavenger, which becomes more and more likely by increasing the SC. Furthermore, linear DNA was found to be more radiosensitive than SV40 minichromosomes, which in turn were more radiosensitive than compact chromatin, which is protected by histones. Furthermore, comparisons with experimental data [45] relative to USX irradiation showed very good agreement. Results from simulations for SSB and DSB yields by protons at different energies as a function of SC in different target structures are presented in order to compare different radiation qualities.

4.5.1 Material and methods

Track structure and simulations

In the case of photons (USX) as primary particles, matter-radiation interaction takes into account different processes such as photoelectric effect (including Auger electrons and fluorescence electron emission), Compton effect and coherent scattering. Each of these processes are simulated considering their respective cross-sections used as input data for the first module. The second module (for secondary electrons) uses as input data the starting point, energy depositions and directions of secondary electrons. Inelastic scattering cross sections for electron-water interaction have been evaluated within the first Born-approximation. Low-energy regime corrections to Born approximation are taken into account by electron-exchange effects and semi-empirical results.

In the present study simulation of irradiation was performed using two kind of monoenergetic and parallel particle beams impinging on DNA target structures:

USX photons (1.5 keV) and protons (with energy 600 keV, 5 MeV and 10 MeV).

DNA target models, beam characteristics and the geometry of simulations

In the simulations relative to USX, the DNA target models have been positioned in a random way inside a virtual cylinder with a 6 μm radius and 5.8 μm height representing the cell nucleus modelled in the PARTRAC code.
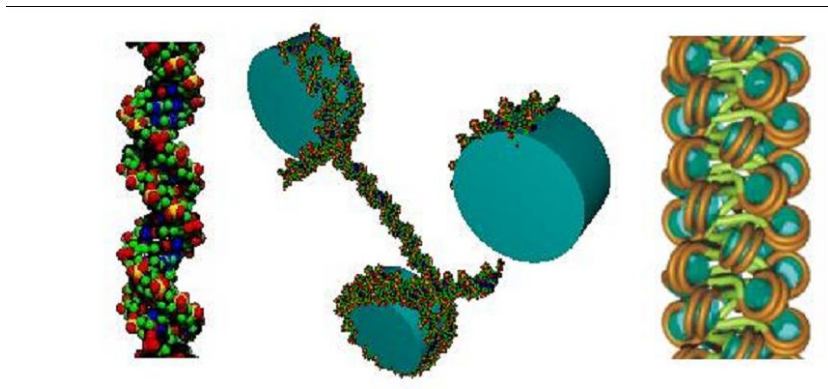

Figure 4.11: Target structures used in PARTRAC for this work [35]: linear DNA, SV40 'minichromosome' and compact chromatin fiber.

For a comparison with experimental data [45], a linear DNA fragment (with 41 bp) has been used. Other simulations have been performed with different targets: chromatin fragments in compact form (2400 bp and 12 nucleosomes) and SV40 'minichromosome' (412 bp and 3 nucleosomes). The studied target structures are shown in Fig. 4.11. The cylinder containing the targets was positioned on a $2.5\mu m$ mylar layer (density 1.4 g/cm^3) to simulate the mylar base used in the experiment. To optimize the time of calculations, each DNA fragment or chromatin fragment has been included in a cylindrical box of 14 nm height (for linear DNA) or 20-25 nm height (for compact chromatin and SV40 'minichromosome'). The cylinder radius was variable and it is given by the sum of the target radius and the mean free path of $\cdot OH$ radical. The last quantity has been calculated by the relation $(6D/SC)^{1/2}$, where D is the diffusion coefficient relative to $\cdot OH$ radical ($2.8 \cdot 10^9$ nm^2 s^{-1}) and SC is the environment scavenging capacity. Simulations have been performed for different values of scavenging capacity, ranging from $9.9 \cdot 10^5$ to $7.5 \cdot 10^8$ s^{-1} (a value corresponding to $4 \cdot 10^8$ s^{-1} was taken for SC relative to cell environment as proposed in [46]). Irradiation with USX has been performed with a parallel and monoenergetic beam of photons with energy 1.5 keV and the beam (with a $9\mu m$ radius) has been directed perpendicularly to the mylar layer. In each irradiation, in order to obtain a sufficient number of damages, $6.687 \cdot 10^7$ eV have been deposited in the cylinder corresponding to a dose of 156 Gy (this value has been choosen randomly but high enough to guarantee to obtain a high number of damages). Furthermore, to obtain a significant statistics, for each value of scavenging capacity, irradiation has been repeated ten times (ten independent

simulation runs). In this way the errors were maintained below 10% for SSB and below 20% for DSB and considered acceptable.

As mentioned above, after testing the code comparing the results of simulations with experimental data related to irradiation with USX, a series of simulations have been performed to calculate the proton-induced DNA damage to evaluate how this effect can be modulated by radiation quality.

For each type of target, simulations have been repeated for values of scavenging capacity ranging from $4 \cdot 10^6$ s^{-1} to $6.67 \cdot 10^9$ s^{-1}, corresponding to a $\cdot OH$ mean free path of 64.8 nm and 1.6 nm, respectively. Irradiation has been performed with a parallel beam (10 μm radius) perpendicular to mylar surface with protons at different energies: 0.6 MeV (LET = 36.8 keV/μm), 5 MeV (LET = 7.9 keV/μm) and 10 MeV (LET = 4.6 keV/μm). In order to obtain a number of damages statistically significant, each irradiation has been repeated ten times, and for each of them it has been deposited in the cylinder $5.85 \cdot 10^8$ eV, corresponding to 100 Gy.

4.5.2 USX experimental data used for validation

In the experiment described in [45], SSBs and DSBs yields induced by USX with energy 1.5 keV in DNA fragments in aqueous solution (for a wide spectrum of scavenging capacity), were obtained through the ionization of Aluminium K-shell. The target, made of pUC18 plasmids (2686 bp) in aqueous solution (thickness 7.8 μm), with gradual injection of TRIS (as chemical scavenger), was positioned on a mylar layer (thickness 2.5μm). After radiation passed through the mylar lyer, interaction of USX with water gave (as primary product, $\sim$ 94%) a photoelectron with energy 0.96 keV (coming from oxygen K-shell) and an Auger electron with energy 0.52 keV. The mean dose-rate was 30 Gy/min. DNA damage was evaluated by Pulsed Field Gel Electrophoresis (PFGE)[45, 47] . The experiment has been performed for scavenging capacity ranging between $9.9 \cdot 10^5$ and $7.5 \cdot 10^8$ reactions/s. The solution scavenging capacity has been calculated using the TRIS-$\cdot OH$ reaction-constant ($1.5 \cdot 10^9$ dm^{3}ml^{-1}s^{-1}). In the interval given above relative to SC, the mean number of SSB/Gy/Da obtained in the experiment varied from $4.61 \pm 1.5 \cdot 10^{-9}$ (for SC=$9.9 \cdot 10^5$ s^{-1}) to $3 \pm 1 \cdot 10^{-10}$ (for SC=$7.5 \cdot 10^8$ s^{-1}). The mean number of DSB/Gy/Da, varied from the value $1.26 \pm 0.41 \cdot 10^{-10}$ (for SC=$9.9 \cdot 10^5$ s^{-1}) to $2.27 \pm 0.75 \cdot 10^{-11}$ (for SC=$7.5 \cdot 10^8$ s^{-1}).

4.5.3 Results

Simulations with USX: comparison with experimental results and extension to different target structures

The induction of SSBs and DSBs by 1.5 keV USX impinging on different target structures (e.g. linear DNA, SV40 'minichromosome and compact chromatin) was simulated as a function of SC of DNA environment. The model predictions (solid lines) compared with Fulford experimental data are reported in Fig. 4.12 and

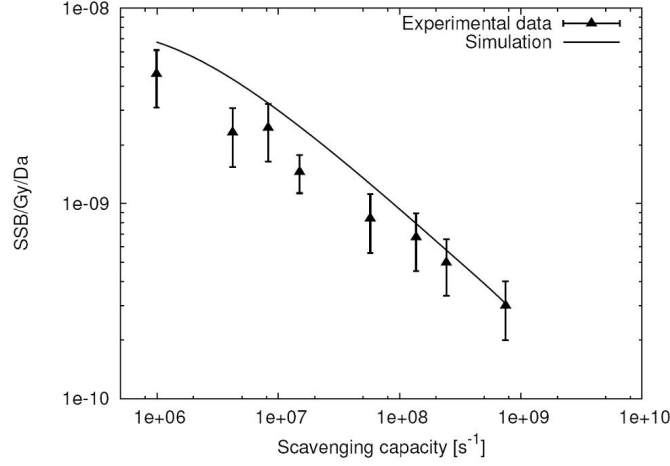4.13, which show calculated yields of SSB/Gy/Da and DSB/Gy/Da following irradiation of linear DNA target.

Figure 4.12: SSB per Gy per Da induced by 1.5 keV USX in linear DNA as a function of scavenging capacity: comparison between simulations [35] and experimental data from [45].

Results of simulations showed a good agreement with experimental data from [45] providing a validation of the model both in terms of adopted assumptions and in terms of simulation techniques. As expected, results showed a reduction in SSB and DSB induction by increasing SC. Simulations with USX have been extended to other target structures with a higher level of compactness: for example, results for DSB/Gy/Da as a function of SC (see Fig. 4.14) showed a decrease of damage induction by increasing the target compactness level.
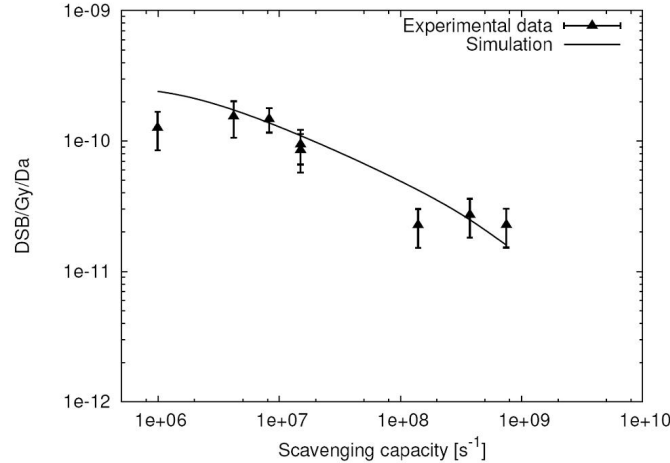

Figure 4.13: DSB(Gy/Da induced by 1.5 keV USX in linear DNA as a function of scavenging capacity: comparison between simulations [35] and experimentaldata from [45].

More specifically, the comparison between different targets (for SC value kept fixed) provided a quantification of the protection due to the presence of histones
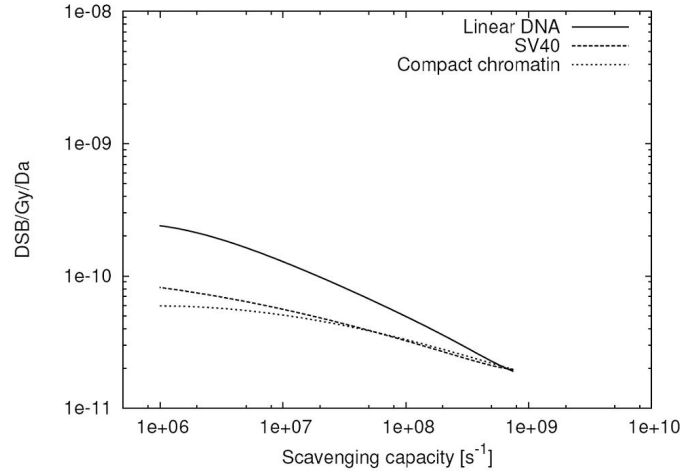
Figure 4.14: Calculated DSB induced by 1.5 keV USX as a function of scavenging capacity using different targets [35].

and to a first level of DNA folding and to the higher order of chromatin folding and compactness.

Simulations with protons: the role of target structures and radiation quality

The model was tested using protons of different energies in order to quantify the dependence on radiation quality. Fig. 4.15 shows examples of results of simulations with 5 MeV energy protons relative to the mean number of DSB/Gy/Da with different target structures as a function of scavenging capacity, obtained with the PARTRAC code.

Similar simulations were performed with 600 keV and 10 MeV protons using

Figure 4.15: Calculated DSB as a function of scavenging capacity for 5 MeV protons for different target structures [35].

104

the same targets. As expected, for all proton energy values, the results showed an increasing DSB yield by increasing scavenging capacity. This represents the effect of scavengers that reduce the number of radicals present in the environment. Moreover, independently of pr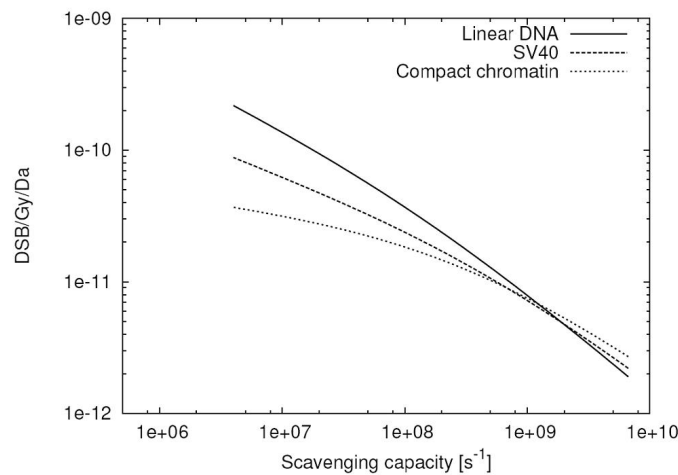oton energy, linear DNA was found to be more radiosensitive than SV40 'minichromosomes', which in turn were more radiosensitive than compact chromatin, which is protected by histons.

Fig. 4.16 shows DSB yields from simulations with protons (at different energies) as a function of scavenging capacity in linear DNA compared with previous results relative to USX irradiation. For what concerns protons, results from simulations
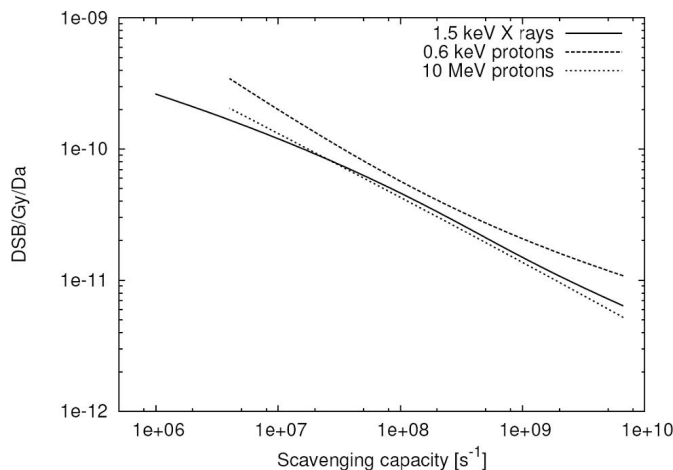

Figure 4.16: Calculated DSB as a function of scavenging capacity for 600 keV and 10 MeV protons compared with USX for linear DNA [35].

showed a behaviour analogue to that found for USX, confirming the protective role of scavengers, histons and chromatin compactness.

4.5.4 Discussion

The induction of SSBs and DSBs following USX and proton irradiation of DNA in different folding conditions (e.g. linear DNA, SV40 'minichromosomes' and compact chromatin) was modelled with the biophysical simulation code PARTRAC. Simulations were carried out for different values of the $\cdot OH$ mean lifetime corresponding to different environment scavenging capacities (SC), with the aim of uncoupling the role of histones and chromatin folding from that of (non-histonic) $\cdot OH$ scavengers. Good agreement was found with available experimental data relative to USX irradiation [47] of linear DNA and in different $\cdot OH$-scavenging conditions, thus providing a further validation of the adopted assumptions and simulation techniques. As expected, linear DNA was more radiosensitive than SV40 'minichromosomes', which in turn showed higher radiosensitivity with respect to compact chromatin due do the larger accessibility offered to $\cdot OH$. Comparing USX- and proton- induced damages from simulations, in order to quantify the role of radiation quality, what was expected was in general found: increasing

LET showed a reduction of SSB yield while an increase in DSB induction was observed. This confirms the effect of high LET radiation which is characterized by a more clustered track, yielding a higher probability of simultaneous DNA breaks (separated by few base pairs) in opposite strands. This confirmed the relevance of the radiation track structure (at different LET) both at the nanometer level (clustering at the DNA damage level, or "small-scale clustering") and at the micrometer level (clustering along high-LET tracks, or "large-scale clustering"). These results reflect the general feature of mechanistic ab initio models and simulations codes, which are fundamental tools to understand the role of stochastic phenomena, of the different mechanisms leading to radiation damage and, of radiation quality. To be more specific, Monte Carlo simulations with the PARTRAC code allow the quantification of the protective effects of different DNA structures and compactness levels (typically chromatin folding and histones) and the relative roles of scavengers in the induction of single- and double- strand breaks. With these simulation results, a possible quantification of both the role of complexity level of distribution of DNA damages and the role of the level of DNA compactness is possible. These two roles were found to play in an interconnected way in damage induction processes.

Chapter 5

Heavy ion track structure and DNA fragmentation

The evaluation of the risk associated to low doses of ionizing radiation is still an open question in radiation research [1]. For radiation protection purposes, the risk at low doses is generally obtained by extrapolations from data at higher doses, mainly obtained from A-bomb survivors. However, the Hiroshima and Nagasaki survivors were mainly exposed to low-LET radiation, thus providing estimations which might not hold for high-LET exposure. Astronauts' exposure to space radiation represents an example of scenario where high-LET radiation plays a relevant role since GCRs (*Galactic Cosmic Rays*) spectra contain a large component of high-LET particles, not only He ions but also heavier ions such as Carbon and Iron (HZE particles, i.e. with high charge and energy).

The continuous exposure to Galactic Cosmic Rays is one of the main concerns for astronauts participating in long term missions [51, 53, 54], and reliable risk estimations demand for a deeper knowledge of the action of heavy ions. Therefore there exists a strong need for both experimental and modelling studies, the latter possibly based on radiation track-structure simulations taking into account the complex structure of the heavy ion tracks, which are characterized by energetic secondary electrons that can travel several tens of microns far away from the primary ion track. Monte Carlo code based on a description of the track structure at the nm level, also called "event-by-event" codes, are particularly suitable as a starting basis to build soundly-based mechanistic models of the action of ionizing radiation (including heavy ions) on biological structures. The scenario at low doses can be further complicated, as will be discussed in the next Chapter, by the possible occurrence of "non-targeted" effects [1] - typically *bystander effects* - consisting of the induction of cytogenetic damage in cells which have not suffered any energy deposition by radiation, but respond to molecular signals released by irradiated cells. These effects might play a non negligible role following exposure to radiation in space, where only a fraction of cells are traversed by radiation. This might have important implications on the estimation of low-dose risks, which is currently based on the so-called "Linear No Threshold" (LNT) hypothesis. Accord-
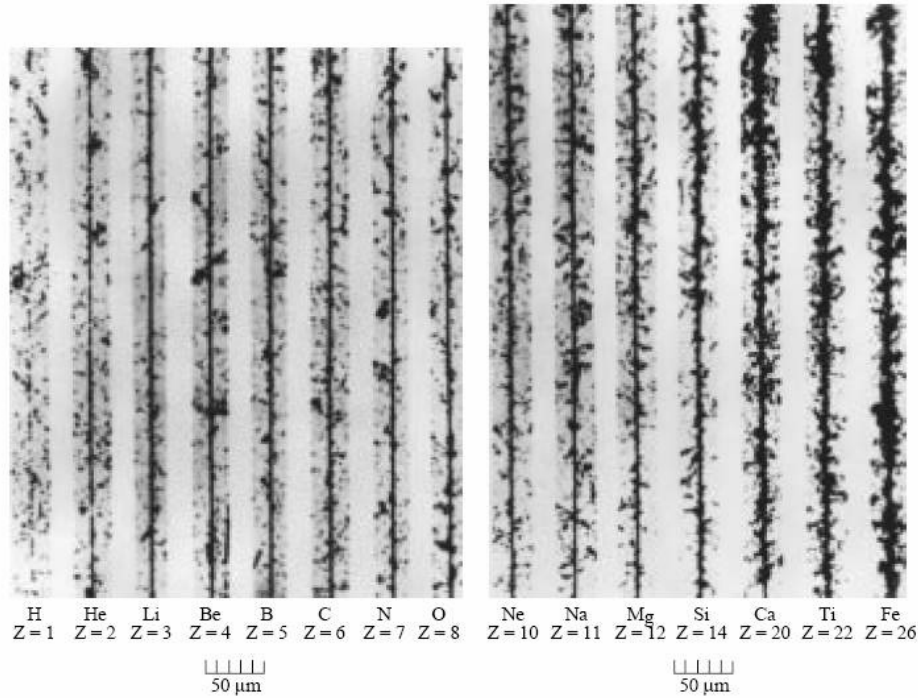
Figure 5.1: Cosmic-ray ion tracks in nuclear emulsion [51]. An increase of event density around the primary track is visible with increasing ion charge.

ing to this approach, the risk at low doses can be estimated by linear extrapolation of data at higher doses. Indeed, during the last decade the large amount of data on non-targeted effects has challenged the LNT hypothesis, suggesting that the risk at low doses might be not linear. Whether the risk would be most likely to be supralinear or sub-linear is still not clear, and probably it does strongly depend on the specific exposure conditions. In particular, whether the exposure is in vitro or in vivo is a fundamental issue. Despite the large amount of data produced in the last ten years, the mechanisms underlying non targeted effects are still very unclear even in vitro, and the scientific community will largely benefit from new experimental data and theoretical models. Such models should be "as mechanistic as possible", avoiding the introduction of free parameters to be fitted a posteriori and using parameters with a clear biophysical meaning, which can be fixed by ad hoc experiments designed in the framework of a continuous collaboration between experimentalists and modellers. In this Chapter, we present and discuss a modelization of DNA fragmentation induced by iron ions [50], whereas non targeted effects, in particular the diffusion of molecular signals in the context of the bystander effect, will be discussed in Chapter 6.

5.1 Upgrade of the physical module for heavy ions

In the initially available version of the PARTRAC code it was only possible to run irradiation simulations with photons, electrons, protons and alpha particles. The various files that constitute the program (written in Fortran 77) have been suitably modified to introduce the possibility to simulate irradiation with any type of primary ion in the non relativistic regime.

The physical *hiontrac* module, initially valid only for helium ions, has been modified in some physical parameters to adapt the code to reproduce the physics (i.e. track structure) of different heavier ions.

The mean free path λ of the primary particle has been rescaled with the help of the following formula

$$\lambda \longrightarrow \lambda' = \lambda \cdot \frac{Z_\alpha^{*2}}{Z_{ion}^{*2}}$$

where Z_α^* and Z_{ion}^* are the effective helium ion charge (see Barkas formula) and specific ion charge respectively (for two different particles having the same velocity, the LET ratio becomes equal to the ratio of the effective charges squared). In addition to the rescaling of the mean free path of the primary particle we have to consider the heavier mass of the specific ion respect to helium ion: for this reason the energy lost in each interaction has been rescaled multiplying it by the ratio A_α/A_{ion}, that is the ratio of respective mass numbers. To validate the correctness of the method adopted, some preliminary tests have been performed [13], also reproducing the results of radial energy and dose distributions obtained in a previous work [52] for protons and helium ions

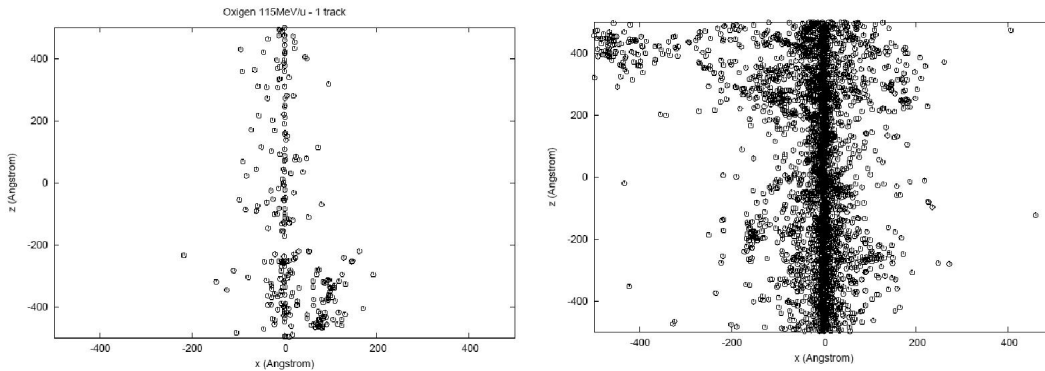## 5.1.1 Comparison between different particle tracks

Figure 5.2: PARTRAC track simulations for different ions with the same energy per nucleon in liquid water. *Left*: two-dimensional projection of a 115 MeV/u oxygen ion track; *Right*: two-dimensional projection of a 115 MeV/u iron ion track .
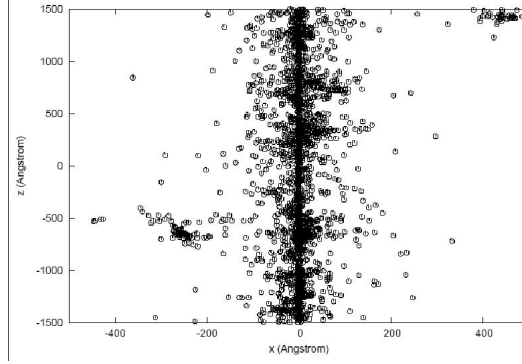
Figure 5.3: Two-dimensional projection of a 414 MeV/u iron ion track simulated with the PARTRAC code.
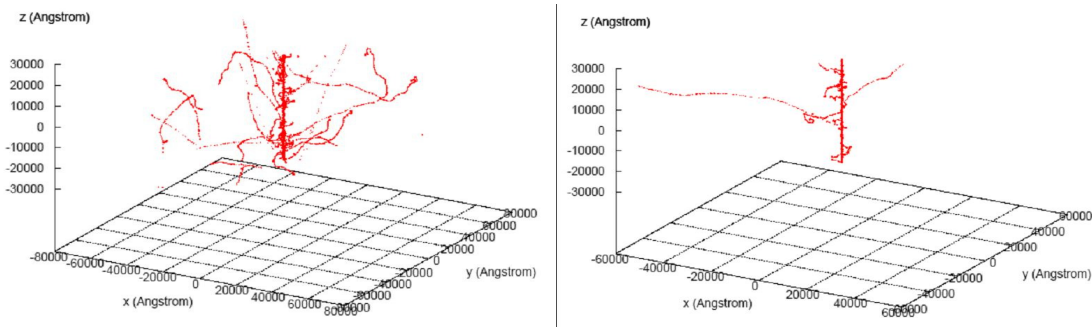

Figure 5.4: PARTRAC simulations of iron ion tracks in liquid water. *Left*: three-dimensional plot for a 115 MeV/u iron ion; *Right*: three-dimensional plot for a 414 MeV/u iron ion.

We begin comparing some examples of tracks simulated for different particles with the same energy per nucleon (that is, the same velocity). Fig. 5.2 shows tracks of different ions (oxygen and iron) having the same energy, that is 115 MeV/u. All the track plots shown in this Subsection have been obtained irradiating, starting from the same point, the same target. Afterwards the same track segment has been isolated, keeping the same track length. The points in the plots represent all the interactions of primary and secondary particles with the target (not only DNA direct interactions, but also indirect ones) given as an output file from the physical modules (*protrac/hiontrac* for primary particles and *etrac* for secondary electrons). These interactions have been subsequently processed and plotted by graphical programs.

For the calculation of the LET we used*SRIM2006* [55], a free software for LET and range calculation. The figures confirm what has been written in the previous Chapters: the LET is inversely proportional to the velocity squared and directly proportional to the charge squared of the ionizing particle (see Fig. 5.2). It is also important to analyze iron ion tracks for different energies. A comparison of the three-dimensional plots in Fig. 5.4 shows that in 414 MeV/u iron ion track we have the presence of longer tracks due to secondary electrons that depart from the primary track respect to the 115 MeV/u iron ion plot, where the secondary tracks

are shorter. Indeed greater is the energy (therefore the velocity) of the primary particle, greater is the maximum energy that can be transferred in the production of secondary electrons, consequently greater will be the range of secondary particles. Figures 5.2 (rigth) and 5.3 show a two-dimensional projection of an iron track with different energies. As it can be seen in these plots, the event density near the primary track is different due to the different LET of the correspondig particle energies.

5.2 Relative biological effectiveness (RBE)

It is experimentally observed that densely ionizing radiations, e.g. helium ions or heavier ions, have a greater biological effectiveness respect to the same X-rays dose. A comparison of two dose-effect curves for cell inactivation following X-ray and helium ion exposure are shown in Fig. 5.5.
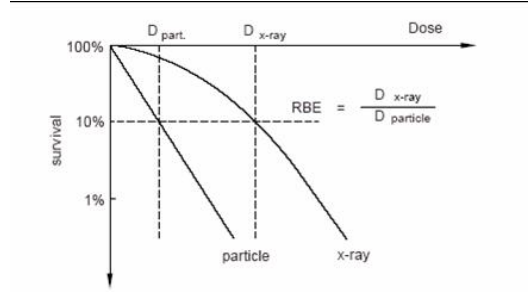
Figure 5.5: Dose-effect curves for cell inactivation after exposure to X-rays and helium ions.

The X-ray curve can be approximated by a linear-quadratic curve type with the formula

$$S = S_0 \exp\left[-\left(\alpha D + \beta D^2\right)\right] \tag{5.1}$$

where S/S_0 is the fraction of survived cells, and α and β are parameters that describe the behavior of the curve as a function of dose D.

For helium ions, and in general for high LET radiation, the quadratic component of Eq. (5.1) (thanks to the increasing of the ionization density) becomes negligible respect to the linear component. For this reason the survival curve is characterized by a pure exponential behavior with dose, of the type given by

$$S = S_0 \exp\left(-\alpha D\right) \tag{5.2}$$

To compare the effectiveness of different radiations, the concept of *relative biological effectiveness* (RBE) was introduced. It is defined as the ratio of the dose of a reference radiation (generally X-rays) and the dose of the radiation under consideration necessary to obtain the same biological effect

$$RBE = \frac{D_X}{D_{ion}} \qquad\qquad (5.3)$$

The RBE is a quantity that is variable with dose because of the non linearity of the X-rays curves, and depends strongly on the effect level on the target: is very high for low doses and diminishes for higher doses. Heavy particles are characterized by high local doses. For ions, high doses are yet produced near the single track core. For example, at the end of a carbon ion track, the local ionization density reaches very high levels, and for this reason the most non-repairable DNA damage is produced by a single track: this means high RBE and high effectiveness in tumor cell inactivation.

5.3 Modelization of DNA fragmentation induced in human fibroblasts by ^{56}Fe ions

There is by now a wide consensus in the recognition that DNA double strand breaks (DSB) are critical lesions in the pathways leading from the deposition of energy by radiation to cellular damage. In this framework, the spatial distribution of radiation induced DSB is most likely a very important factor for the fate of cells that have been irradiated: cellular endpoints such as gene mutations, chromosome aberrations and cell death will depend on the statistical properties of the DSB ensemble induced by the irradiation [40]. Indeed, the spatial correlation of DSB, both in terms of physical distance and of genomic distance, is thought to affect their reparability. Therefore, the biological consequences at a given dose can depend on the radiation quality, since the DSB distribution will be determined not only by the chromatin conformation, but also by the radiation track structure. At the scale of the nucleosome, i.e., 100 bp, and of the low-level chromatin fiber organization, i.e., 1 kbp, DSB induced by radiation are correlated, as outlined by some experimental and theoretical studies [28, 57, 36, 58, 59]; it is expected that for high-LET charged particles the correlation is much higher than for low-LET radiation. However, also at larger scales, where low-LET radiation should induce a random distribution of DSB, high LET-radiation can still produce a DSB distribution that deviates considerably from randomness [60, 61, 62, 63, 64]. The statistical properties of the induced DSB can be studied through the DNA fragment size distribution that is present after the irradiation. Therefore, the analysis of fragment spectra can give an important contribution in the quest of a more precise prediction of the consequences of irradiation by HZE particles, such as those that would be encountered during long term space travel.

In this work we investigated the DNA fragment spectra induced by 115 MeV/u iron ions (LET=442 keV/μm in the sample) in human fibroblasts [50]. Recently we extended the same analysis (see Subsection 5.3.3) for 414 MeV/u iron ions (201 keV/μm in the sample). The experimental spectra correspond to several doses up to 200 Gy, and they concern the size range 1-5700 kbp. The DNA fragment spectra induced by 115 MeV/u were also analyzed with a phenomenological tool, the

generalized broken stick (GBS) model [65], which characterizes in an approximate but simple way the non-random nature of a spectrum. For comparison, the same analysis was performed on the experimental fragment spectra induced, on the same cell line, by γ-rays. Together with this analysis, simulated fragment spectra induced by iron ions were obtained in this work through the Monte Carlo code PARTRAC, that has been upgraded with the implementation of heavy ions. The comparison between experimental and simulated data was performed analyzing the number of radiation induced DNA fragments, as a function of dose, in four different size ranges, by which the total experimental range 1-5700 kbp can be divided. The ranges are 1-9 kbp, 9-23 kbp, 23-1000 kbp, and 1000-5700 kbp. Furthermore, the simulations allowed to evaluate the number of fragments also outside the experimental range, i.e., for sizes <1 kbp and for sizes >5700 kbp.

The implementation of heavy ions in the PARTRAC code offers the possibility to extend this study to high LET iron ions. In the four experimental size ranges we found a satisfactory agreement between the two sets of data, in particular if the still ongoing development of heavy ions transport in PARTRAC is taken into account. In addition, a relevant result is represented by the very high number of fragments that, according to the Monte Carlo simulations, are produced by iron ions in the size range <1 kbp. This is consistent with the very high DSB correlation that is found also through the GBS model in the lower part of the experimental size range (1-9 kbp) for iron ions [65].

5.3.1 Materials and Methods

This Subsection provides the most relevant information about the experimental procedures and the theoretical tools.

Experimentals

The experiments were performed by colleagues of the Istituto Superiore di Sanitá on AG1522 normal human fibroblasts. For a complete description of cell culture, irradiation procedures and DNA fragment spectra measurement the reader is referred to two recent publications [66, 67], dedicated to the presentation and analysis of experimental fragment spectra obtained after irradiation with several different iron ion beams and with γ-rays. Here we consider few relevant details.

Irradiation with 115 and 414 MeV/u iron ions was performed at the *Heavy Ion Medical Accelerator* (HIMAC) of the National Institute of Radiological Sciences (NIRS), Chiba, Japan; the dose-averaged LET at sample position was 442 keV/μm (in water), and the dose rate was about 10 Gy min^{-1}. Irradiation with ^{60}Co γ-rays was performed at the Istituto Superiore di Sanità, with a dose rate of about 3.5 Gy min^{-1}. DNA fragment spectra were measured with gel electrophoresis, using four different electrophoresis conditions, each one optimized for the detection of fragment sizes in a particular range: three different conditions of *Pulsed Field Gel Electrophoresis* were employed for the measurement of fragments in the size ranges 9-23 kbp, 23-1000 kbp and 1000-5700 kbp, respectively; *Constant Field Gel*

Electrophoresis was used for the detection of the smallest detectable fragments, in the size range 1-9 kbp.

Setup of the PARTRAC code

In the present study, a model nucleus embedded in a water surrounding was irradiated from the bottom with a parallel beam. Each energy deposition event in the cell nucleus was recorded, so that for each simulated irradiation, the dose could be calculated dividing the total deposited energy by the mass of the cell nucleus, given by the product between the nucleus density (1.06 g cm^{-3}) and volume. Starting points, energy and directions of secondary electrons were used as input data of the electron module as fully described in Chapter 4.

The simulated yields of radiation-induced DNA strand breaks were determined by the superimposition of the track structure pattern of inelastic events on the DNA target model [48, 28, 29]. The probability of inelastic energy deposition events in that volume producing a SSB was assumed to be 0 for energy depositions smaller than 5 eV, to increase linearly from 0 to 1 for energy depositions in the range 5-40 eV, and to be equal to 1 for energy depositions larger than 40 eV. Concerning indirect effects, ionized water molecules were assumed to dissociate following the scheme $H_2O^+ + H_2O \rightarrow H_3O^+ + \cdot OH$, whereas excited water molecules were assumed to undergo either relaxation or dissociation. An interaction between an $\cdot OH$ and a sugar-phosphate was assumed to induce a SSB with 65% probability. Two SSB on subsequent nucleotides in the same strand were considered as one SSB, whereas a DSB was assumed to occur when two SSB were found on opposite strands within 10 bp. To take into account transfer processes, a conversion into a DSB was assumed for 1% of all breaks produced by both direct and indirect effects.

The starting point of fragmentation analysis was the output data set of the effect module, containing the genomic positions of DSB due to irradiation with a dose of n Gy. The number of double-stranded fragments, for each fragment size range, was computationally determined by calculating the distances between adjacent breaks or chromosomes ends.

5.3.2 Results for 115 MeV/u iron ions

From the experiments it resulted that it is possible to define, both for γ-rays and for iron ions, separate yields for the two size ranges 1-23 kbp and 23-5700 kbp. Indeed, the number of radiation-induced fragments in these two ranges can be well fitted by a linear function, at least for the doses considered here, which are in the interval 40-200 Gy for the range 23-5700 kbp, and 100-200 Gy for the range 1-23 kbp, where the more difficult detection of fragments requires higher doses. Obviously, the total experimental DSB yield, in the size range 1-5700 kbp, is given by the sum of the two separate values measured in the two size regions. Table 5.1 summarizes the experimental results. It can be noted that, for 115 MeV/u iron ions, in the region 1-23 kbp one finds about 30% of the total number of fragments,

as measured in the "complete" range 1-5700 kbp; for γ-rays this fraction is only about 15%.

Radiation type		< 1kbp	1-23 kbp	23-5700 kbp
115 MeV/u Fe ions	PARTRAC	53.73	13.47	34.01
	Exper.		16.06±4.75	37.00±2.63
$\gamma-rays$	Exper.		5.78±1.16	33.86±2.63

> 5700 kbp	Total (cell Gy^{-1})	RBE
2.25	107.47 (all sizes)	2.39 (all sizes)
	53.06±5.46 (1-5700 kbp)	1.34±0.17 (1-5700 kbp)
	39.64±2.89 (1-5700 kbp)	

Table 5.1: The yelds in each column are given in units of (cell Gy^{-1}) and the lower part of the table is the continuation of the upper part. Experimental data are given for both radiations, while simulations results are shown only for iron ions. Simulation results for γ-rays, used for the evaluation of RBE, can be found in [65]. Extremely small fragments, of size less than 1 kbp, and fragments of size larger than 5700 kbp, are not detected experimentally, and thus the corresponding entries are blank. Consequently, the RBE given in the last column considers, for the experimental evaluation, only fragments in the range 1-5700 kbp, while the PARTRAC value takes into account fragments of all sizes.

The comparison of the data concerning 115 MeV/u iron ions with the PAR-TRAC results is shown in Fig. 5.6. In each of the four panels of the figure, the number of fragments with sizes belonging to the specified range is plotted as a function of dose. The four ranges are those corresponding to the four different electrophoresis conditions. Full symbols refer to the experimental values, while open symbols denote the PARTRAC results. The simulations were performed for five dose values, i.e., 5, 50, 100, 160 and 200 Gy. In all cases the data were normalized to give the number of fragments per Mbp. The agreement between experiments and simulations, although far from being perfect, can be considered satisfactory, given that no a posteriori adjustment of the code parameters was introduced. It should be noted that in the range 9-23 kbp the experimental values are somewhat less reliable, as outlined in particular by the unlikely variation of the data with the dose. It might be necessary to point out that this fact does not contradict, from a practical point of view, the possibility to fit by a linear function the number of fragments in the enlarged size range 1-23 kbp : indeed the scales of the ordinate axes in Fig. 5.15 show that, within this size region, the contribution from the range 1-9 kbp is predominant.

The comparison with the experimental data gives confidence on the results obtained with PARTRAC outside the measured size range. Fig. 5.7 consists of two panels; in the first one we show the calculated number of fragments with a size larger than 5700 kbp, while in the second one the two sets of simulated data correspond to the fragments smaller than 1 kbp (lower line) and to the total number of
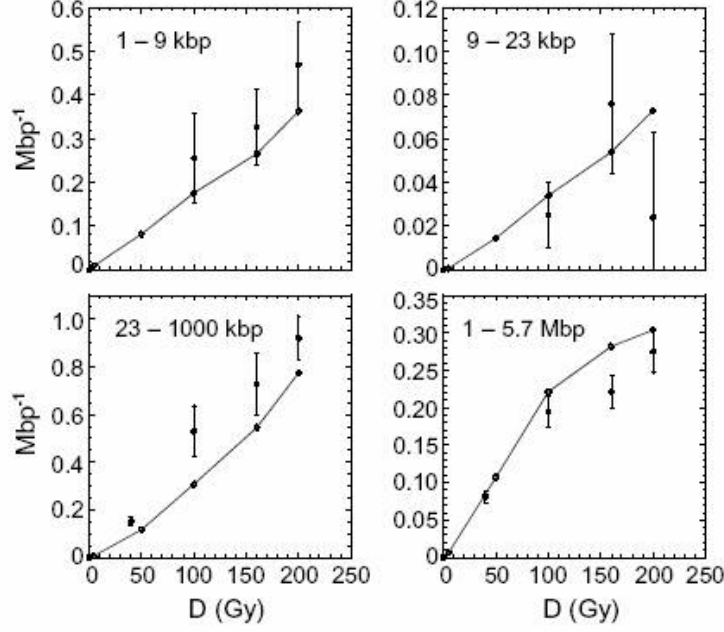
Figure 5.6: Number of DNA fragments per Mbp (of size belonging to the ranges indicated in the corresponding panels) induced by irradiation with 115 MeV/u iron ions, as a function of dose. Full symbols: experimental data with error bars. Open symbols: PARTRAC simulation data at doses of 5 Gy, 50 Gy, 100 Gy, 150 Gy, and 200 Gy; the lines are a guide for the eye.

fragments (upper line), which counts the fragments of any size. Fragments of size <1kbp can be denoted by the notation "*extremely small fragments*". We chose to plot these results in the same panel to outline that the number of extremely small fragments accounts for about half of the total number. As a consequence, the fragment yield as computed by the usual experimental techniques, which cannot detect extremely small fragments, heavily underestimates the real yield.

5.3.3 Extension to 414 MeV/u iron ions

The work described above has been recently extended to 414 MeV/u iron ions. The simulations with the PARTRAC code have been performed with the same irradiation contition setup (geometry of irradiation and dose ranges) described above for 115 MeV/u iron ions and for fragments spectra belonging to the same size range. The comparison of the experimental data with the PARTRAC simulation results concerning 414 MeV/u iron ions is shown in Fig. 5.8, 5.9 and 5.10.

In each of the four panels in Fig. 5.8, the number of fragments with sizes belonging to the specified range is plotted as a function of dose (the four ranges are those corresponding to the four different electrophoresis conditions). Red symbols refer to the experimental values, while black symbols denote the PARTRAC results. The simulations were performed for four dose values, i.e., 50, 100, 160 and 200 Gy and the data are normalized to give the number of fragments per Mbp. The agreement between experiments and simulations, can be considered

Figure 5.7: PARTRAC simulation data giving the number of DNA fragments per Mbp, induced by irradiation with 115 MeV/u iron ions, as a function of dose. Dose values as in the PARTRAC data of Fig. 5.6. Left panel: fragments of size larger than 5.7 Mbp. Right panel: fragments of size smaller than 1 kbp (open symbols) and of any size (full symbols). The lines are a guide for the eye.
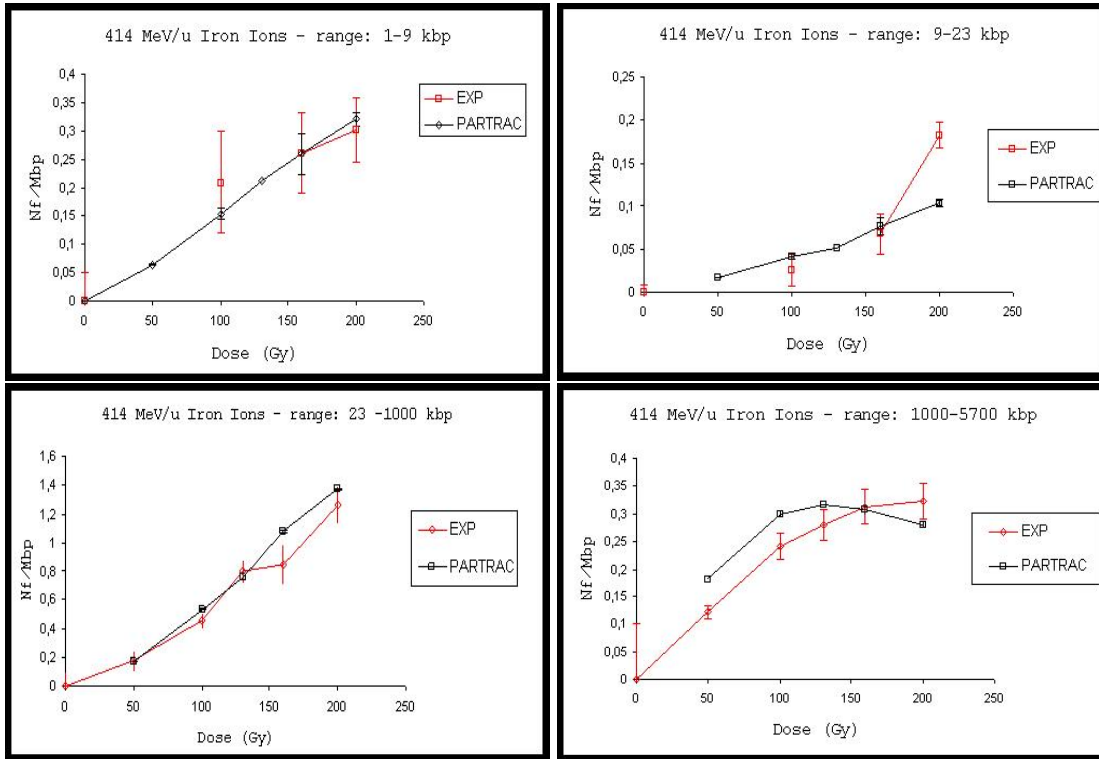
Figure 5.8: Comparison between PARTRAC and experimental data of the number of DNA fragments per Mbp (of size belonging to the ranges indicated in the corresponding panels) as a function of dose induced by irradiation with 414 MeV/u iron ions (PARTRAC simulation data at doses of 50 Gy, 100 Gy, 160 Gy and 200 Gy); the lines are a guide for the eye.

satisfactory, given that, also for this iron ion energy, no a posteriori adjustment of the code parameters was introduced.

Also for 414 MeV/u iron ions, the comparison with the experimental data gives confidence on the results obtained with the PARTRAC code inside the range 1-

5700 kbp and outside the measured size range. In the left panel of Fig. 5.9 it is shown the calculated number of fragments with size larger than 5700 kbp, while in the rigth one there are shown the two sets of simulated data corresponding to fragments smaller than 1 kbp (lower line) and to the total number of fragments (upper line) which counts the fragments of any size. These results, shown in the same panel, first outline that the number of extremely small fragments accounts for about one-third of the total number, second that we have the same general behaviour of the as for 115 MeV/u. As a consequence, also for higher iron energies, the fragment yield given by experimental techniques, which cannot detect extremely small fragments, heavily underestimates the real yield. In the Fig. 5.10 (left panel)it is shown a comparison between experimental data and simulation results for fragments belonging to the range 1-5700 kbp (that is the experimental detectable range) and the results of the PARTRAC simulations relative to all ranges (that is including extremely small fragments ad fragments larger than 5700 kbp). Also this panel gives confidence on the results obtained with the PARTRAC code showing a good agreement between experimental and simulation data. Finally, the left panel of Fig 5.10 shows the linear behaviour of the fragment spectra distibution as a function of dose obtained in the simulations for the range 0-1 kbp.
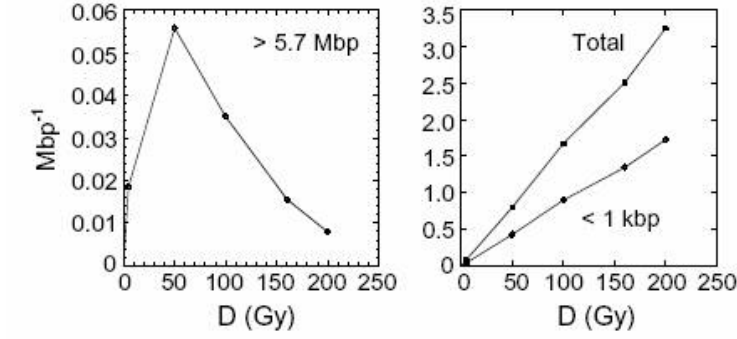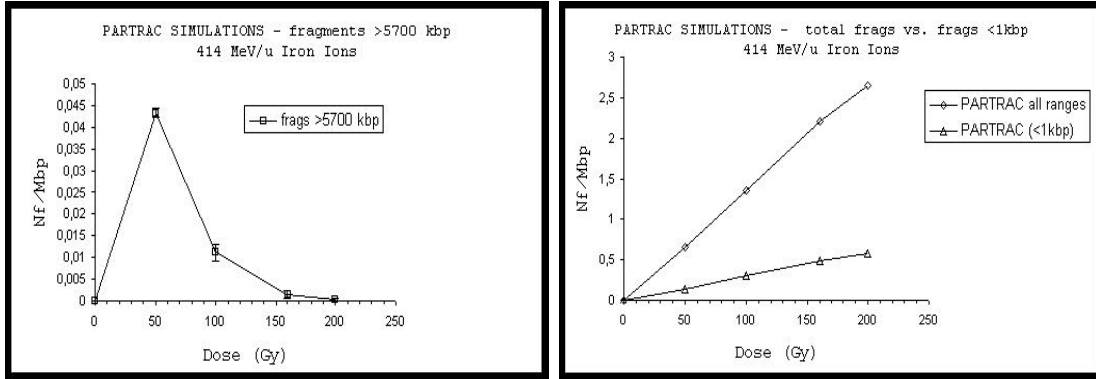

Figure 5.9: PARTRAC simulation data giving the number of DNA fragments per Mbp, induced by irradiation with $414 MeV/u$ iron ions, as a function of dose. Dose values as in the PARTRAC data of Fig. 5.9. Left panel: fragments of size larger than 5.7 Mbp. Right panel: fragments of size smaller than 1 kbp (lower line) and of any size (lower line). The lines are a guide for the eye.

5.3.4   Discussion

The integration of different approaches can be useful in a problem like the determination of the characteristics of DNA DSB induction by radiation.

In summary, the PARTRAC simulations and the GBS model can provide complementary roadways when applied to the study of experiments on DNA fragmentation: the PARTRAC code, especially in its new heavy ion implementation, can test its predictive power against the data concerning the number of fragments in suitable size ranges (not too restricted), whereas the GBS model can estimate

Figure 5.10: Left panel: comparison between experimental data and simulation results for fragments belonging to the range 1-5700 kbp (that is the experimental detectable range) and the results of the PARTRAC simulations relative to all ranges (that is including extremely small fragments ad fragments larger than 5700 kbp). Right panel: PARTRAC simulation data for the number of extremely small fragments (< 1kbp) as a function of dose; the lines are a guide for the eye.
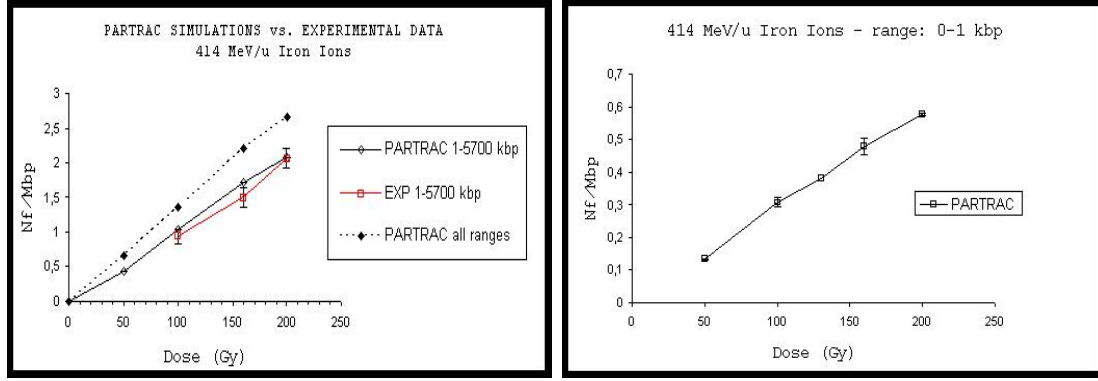
from the data the length scale at which the radiation induced DSB are more correlated.

Moreover, the comparative study (now only for 115 MeV/u iron ions) of the results obtained by the two theoretical methods [65, 50] can also provide a consistency evaluation. With this respect, we point out the relation that can be envisaged between the high DSB correlation at the scale of 1-9kbp (proved, in the framework of the GBS model for 115 MeV/u iron ions) and the very high number of fragments of size smaller than 1 kbp (found also for 414 MeV/u), that has been found in the PARTRAC simulations of the same beam. It is possible to argue that a high DSB correlation can be produced only by the ionizations caused by the same track. However, it is not obvious to infer in which way such a predominant intra-track component in the spectrum, in the range 1-9 kbp, would behave at even smaller sizes, i.e. less than 1 kbp; indeed, at the length scale around 1 kbp one expects, besides the track structure influence, also an important dependence on chromatin conformation, on which there is not yet clear-cut evidence [59]. The PARTRAC simulations provide a response to this point, at least for the model of chromatin conformation implemented in the code [57]. Extremely small fragments, with size less than 1 kbp (mainly due to DSBs caused by the same track), account for about one half of the total fragments for 115 MeV/u iron ions and one-third of the total fragments for 414 MeV/u iron ions in the simulations.

Experimental data on the extremely small fragments would therefore be very valuable for two reasons. First, they would provide a more precise experimental determination of the DSB yield; secondly, they would act as a validation for the low-level chromatin structure implemented in PARTRAC. We point out that, using purposely prepared fragment detection techniques, it was possible to obtain experimental data on radiation induced DNA fragments of sizes below 1 kbp, for human fibroblasts and Chinese hamster cells irradiated with X-rays and helium,

nitrogen and iron ions (of higher energy and lower LET than those considered here), which have been used to gather information about the chromatin structure at that scale [58, 59].

Equally important will be the study of other radiation qualities, even iron ions of different energies and thus LET, by means of the PARTRAC simulations. This will help to verify the dependence on radiation quality of the production of small and extremely small fragments. Protons and alpha particles of relatively low energy (LET values in water of about 27 keV/μm and about 121 keV/μm, respectively) have been already considered [68], but the results can not be compared with the present study, since in that case only an enlarged size range was checked, including fragments smaller than 23 kbp. The data indicated that the alpha particles produced, in that size range, about three times more fragments than the protons. Extending and refining these small fragments evaluations to different radiation qualities will provide, among the other information, also a reliable DSB yield. Its experimental values, if derived from fragment measurement restricted to the usual experimental ranges, are often such that the RBE of the DSB yield is not very larger than 1 even for HZE particles [67], in spite of the expected much higher biological effectiveness of these ions for cellular endpoints. It should be investigated whether the higher effectiveness is entirely due to the larger complexity of the DNA damage (e.g., DSB correlation), or if also a higher DSB yield is an important cause; this yield, as explained above, is generally heavily underestimated in experiments.

Chapter 6

Modelling radiation-induced bystander effect and cellular communication

In the previous Chapters, we treated the induction of DNA damage in irradiated cells. However, starting from the early 1990s, more and more data became available indicating that cells not directly hit by radiation can develop cytogenetic damage, most likely following the release of molecular signals by irradiated cells (*bystander effect*) [71]. This phenomenon was observed for different radiation types and for a wide damage spectrum including both lethal damage, such as clonogenic inactivation [72] and apoptosis [73], and non-lethal damage, typically gene mutation [74, 75] and oncogenic transformation [76, 77]. Chromosome damage [78, 79] and altered expression of specific genes [80, 81] were also reported. While the earlier data were mainly obtained following irradiation with low fluences of light ions, microbeam experiments allow the scoring of cells targeted with a known number of particles [73, 75, 77]. Other techniques include the treatment of unirradiated cells with medium taken from exposed cultures [72] and the sharing of the same culture medium between irradiated and unirradiated cells [81]. Extensive reviews on bystander data can be found in the literature [82, 83].

6.1   Some general aspects of cell communication and bystander effect

It is now widely accepted that *cellular communication*, in its various aspects, plays a pivotal role in the induction of bystander effects (BEs). While the main pathway for cells that are not in close contact is likely to involve the release, diffusion and reception of protein-like molecules [72], adjacent cells can also communicate via gap junctional channels [80], which allow for direct exchange of ions - typically Ca^{++} - and small molecules such as $cAMP$ and organic radicals. In both

121

cases, reactive oxygen species ROS and NO are thought to be involved as well [84]. The identification of the involved signals is currently one of the main open questions. Cytokines, in particular IL-8, IL-2, TNFα and TGFβ were detected in the medium of irradiated cell cultures [85, 86].

A *cytokine* is a hormone-like protein that can serve as intercellular messenger in an autocrine or paracrine fashion. It can be produced by virtually every nucleated cell type in the body, with pleiotropic regulatory effects on hematopoietic and many other cell types participating in host defence and repair processes. Cytokines influence cell function by binding to specific cell-surface receptors, which use phosphorylation and other intracellular mechanisms to trigger signals that produce changes in gene expression. The pattern of cytokine effects is extremely complex, being profoundly influenced by the milieu in which cytokines act, and especially by the presence or absence of other biologically active agents. In addition, cytokines act in a complex, intermingled network where one cytokine can influence the production of many other cytokines. Indeed under natural conditions a cell rarely, if ever, encounters only one cytokine at a time. Indeed, different signal molecules are likely to be involved at the various levels of the communication cascades underlying BEs. Furthermore, the involved signal type(s) can be strongly dependent on parameters such as cell line, cell-cycle stage etc. Indeed unirradiated MSU human fibroblasts treated with medium taken from exposed MSU cultures did not show any BE [72], whereas significant BE was observed in unirradiated AG1522 fibroblasts sharing the culture medium with irradiated cells [81]. Even the signal concentration might play a role, since it has been shown that low concentrations of TGFβ can promote cell proliferation [87], whereas TGFb often acts as a proliferation inhibitor [88]. Despite the progress made in the last few years, many aspects of this phenomenon are still unclear. Examples of important open questions are the following: (1) what is the 'initial' damage that can trigger the release of bystander signals by an irradiated cell?; (2) what is the role played by radiation quality, cell line, cell-cycle stage etc?; (3) how many signals can be released by a single cell?; (4) what is the probability for a bystander cell to develop cytogenetic damage following interaction with a signal, or is there any threshold?; and (5) can bystander cells release signals in turn? BE data also raise the question of the implications of such phenomena for radiation protection and possibly radiotherapy. Indeed if BEs are significant also in vivo, the linear no-threshold approximation generally adopted for low-dose risk might not necessarily hold. Furthermore, BE might be used to optimize tumor control in radiotherapy, allowing one to obtain the same control probability with lower doses.

6.2 Examples of theoretical models

Due to the large uncertainties affecting the knowledge of the mechanisms governing BEs, only a few theoretical models were developed until now. In this section, two models reported in the literature [89, 90], as well as an approach under development at the University of Pavia, are described in detail. All the

three deal with BEs following high-LET irradiation of cells cultured in vitro as monolayers. A stochastic model with allowance for 3-D cell spatial location, cell killing and repopulation was also recently published [91]. The model assumes a 3-D lattice of fixed points where each cell can either be: (1) alive (or undifferentiated) but unaffected; (2) affected and signalling; (3) affected and non-signalling; or (4) dead (or differentiated). Only the affected signalling cells can release bystander signals, which fall off as an exponential function of distance. Although a more detailed description of this complex approach is beyond the scope of this Chapter, it is worth reporting that, consistent with some experimental data, the predicted time-response increases in a saturation-like fashion. Furthermore, the model predicts the effect augmentation following fractionated dose delivery, as well as pronounced downward curvature in the high dose-rate region.

6.2.1 The 'bystander and direct model'

A pioneering approach in modeling bystander effects is the "BaD" (Bystander and Direct) model, developed for in vitro oncogenic transformation induced by alpha particles [89]. The model, which incorporates a bystander response superimposed on a direct response, postulates that the oncogenic bystander response is a binary "all or nothing" phenomenon in a (small) subpopulation of sensitive cells. These cells are also assumed to be particularly sensitive to alpha-particle direct hits, generally resulting in clonogenic inactivation.

The model was applied to acute irradiation of C3H 10T1/2 cells with a microbeam [77], as well as a conventional broad-beam [76]. In particular, microbeam data showed that, when only 1 in 10 cells had its nucleus traversed by a known number of alpha particles, after an initial sharp increase, the oncogenic response shows little further increase with the particle number. Furthermore, the frequency of induced oncogenic transformation is not lower than when all the cell nuclei are hit by the same number of particles. The apparent saturation of the bystander response at low fluences suggested the binary nature of the process, whereas the rationale for the existence of a sensitive subpopulation was suggested by the fact that both a saturation-type dose response and a low-dose inverse dose-rate effect are characteristics of the existence of a hypersensitive subpopulation. Since the main aim of the model was to analyze induced oncogenic transformation frequencies, it was also necessary to analyze clonogenic inactivation of bystander cells, compared to directly hit cells.

For the microbeam experiment where 1 in 10 cells was traversed by an exact number of alpha particles, the surviving fraction was expressed as

$$SF = 0.1q^N + 0.9F(N)$$

where q is the probability for a cell to survive a single alpha-particle traversal, N is the number of traversals per cell nucleus and $F(N)$ is the fraction of bystander cells surviving in this experiment. Having estimated q by the microbeam experiment where 100% of the cell nuclei were hit, $F(N)$ was empirically esti-

mated by subtraction. Concerning oncogenic transformation when 10% of the cell nuclei were hit, the transformants per surviving cell were expressed by

$$TF = \left[0.1\nu N q^N + 0.9\sigma F\left(N\right)\right]/SF$$

where ν (slope of the linear dose–response related to the direct component) and σ (fraction of cells hypersensitive to bystander transformation) are the two parameters of the model, which were adjusted by fitting to transformation experimental data where all cells were irradiated with an exact number of alpha particles [76]. With the two parameters fixed this way, the authors then applied their model to predict the transformation frequency for the case where only 10% of the cells were irradiated with exact numbers of alpha particles [77]. The model predictions could reproduce the data trend, including the observation that irradiation of 10% cells with exactly one particle resulted in a larger effect than irradiation of 100% of cells (with exactly one particle). It is to be noted that no detailed signalling mechanisms were hypothesized in this model. Therefore the approach can apply both to cells that are in direct contact, and to cells that are further apart. Furthermore, the hypersensitivity of the cells belonging to the subpopulation can occur both by virtue of their geometrical location, and by virtue of their biological status. On the possible consequences for radiation risk, the authors state that if the postulated mechanisms were applicable also in vivo, then a linear extrapolation of risk from intermediate to lower doses could underestimate the risk at very low doses, that may be relevant in domestic radon risk estimation.

6.2.2 The 'bystander diffusion modeling' approach

A model of BE based on diffusion of protein-like signals [ByStander Diffusion Modelling, (BSDM)] between hit and non-hit cells was developed by Nikjoo and co-workers, specifically for those situations where gap-junction intercellular communication can be neglected [90]. The BSDM approach assumes that (a) each directly inactivated cell releases m bystander signals, which can interact with unhit cells switching them into a state of cell death or oncogenic transformation; (b) a reaction of a signal with a (bystander) cell occurs when their distance falls below a reaction radius R (taken as 10 mm); (c) such signals are protein-like molecules diffusing in the culture medium according to Brownian motion. More specifically, considering the microbeam experiment where 10% of cells were directly hit with an exact number of alpha particles [77], the surviving fraction was written as

$$SF = 0.1a^N + 0.9\left(1 - B_S\right)$$

and the transformation frequency was expressed as

$$TF = \left[0.1a^N bN + 0.9\left(1 - B_S\right)cB_C\right]/SF$$

where a is the probability of a cell surviving a single cell nucleus traversal, N is the number of particles, BS is the fraction of bystander cells inactivated after

124

treatment with 'irradiated conditioned medium (ICM)', $B_C = f B_S$ (f being the fraction of non-hit cells) and b and c are constant parameters. The values of a, b and c were obtained by statistical analysis of the microbeam experiment where 100% of cell nuclei were hit by an exact number of particles [77], whereas BS was derived from the experiment on clonogenic survival of unexposed cells treated with ICM, i.e. medium filtered from irradiated cultures [72].

The two main parameters used to model molecular signalling are the mobility (i.e. diffusion coefficient D) and the concentration of signals. The mass of the signal was assumed to vary in the range 400-400000 Da; the corresponding values of D were taken from literature data. Fitting the model to ICM data provided $D = 10^8$ nm^{2}s^{-1}, corresponding to a mass of ~ 10 kDa. This is consistent with the hypothesis that cytokines (like Interleukin-8) may play an important role in BE. By comparing the predictions of the BSDM model with experimental data [72, 77], the number of released signals was calculated as $\mu = 8$ for high-LET radiation, $\mu = 1$ for low LET.

The model predictions showed good agreement with the survival fraction and the transformation frequency of the microbeam experiment when 10% of cells were hit by an exact number of particles [77]. In contrast with the conclusions of Brenner and coworkers, the BSDM approach implies an increase in the effect by increasing the number of particle traversals per nucleus (keeping fixed the fraction of irradiated nuclei). In agreement with Brenner and co-workers also the authors of the BSDM model conclude that, if the results seen in vitro could occur also in vivo, linear extrapolations from intermediate to lower doses could underestimate the risk in the low-dose region.

6.2.3   A fully Monte Carlo approach

The approach adopted at the University of Pavia [71] consists of starting from a scenario which is 'as controlled as possible', in order to minimise the number of assumptions and free parameters in the model. An example is provided by experiments with cells seeded at low density, so that one can assume that intercellular communication through gap junctions will not play a significant role. In particular, works are reported in the literature where one to four cells were microbeam irradiated over about 800 normal human fibroblasts seeded on a 10×10 mm^2 dish [73, 92]. The nucleus of each selected cell was traversed by an exact number of He ions, in the range 1-15. Three days after, both irradiated and unirradiated cells were scored for micronuclei and apoptosis. Even when only a single cell was irradiated, that is the situation on which we will focus herein, the fraction of damaged cells (i.e. micronucleated or apoptotic) was found to be about 3%, i.e., two- to three-fold with respect to the control.
This scenario was reproduced by simulating a 10×10 mm^2 grid, with 841 (29×29) cells located at regular distances so that the distance between a cell and its (four) closest neighbors is 0.35 mm. Main assumptions of our model, specific for high-LET irradiation of sparsely seeded cells, are the following: (a) each irradiated cell releases N signalling molecules; (b) at each time step Δt, the signals move in the

extracellular environment according to the diffusion laws, with the mean square of the travelled distance given by $< r^2 > = 6D\Delta t$, where D is the diffusion coefficient of the considered molecule; (c) a reaction between a signal and a (bystander) cell occurs when the distance between the signal and the cell centre falls below a reaction radius R; (d) whenever a reaction occurs, the signal molecule is ruled out of the simulation, whereas the cell will become damaged with probability p_{dam}; and (e) specifically for the second version of the model (see below), also bystander, damaged cells can in turn emit signals with probability p_{em}. Assumption (a) is consistent with the evidence that, at least for high-LET irradiation of sparsely seeded cells, the bystander response does not show significant dose-dependence, i.e. the fraction of (bystander) damaged cells is almost independent of the fraction of irradiated cells, as well as of the number of cell traversals [92]. On the basis of both experimental [85, 86] and theoretical [90] studies, the signals were assumed to be protein-like molecules. Good candidates are cytokines such as IL-8, which has a mass of about 10k Da and a diffusion coefficient in water of $\sim 10^8$ nm^{2}s^{-1}. Concerning the number of molecules released by each cell, in this work we will present examples of applications obtained with $N =$400000. This choice is based on measurements of IL-8 concentration, which was found to be of the order of 50 pg ml^{-1} in an experiment where about 7000 cells were irradiated and cultured in 2 ml medium [86]. Despite pure diffusion was applied, possible effects of the gravity force can be implicitly taken into account by choosing small values for the culture medium thickness (typically 20 mm, although simulations were run also for values of the order of 1 mm). Assumption (c) was adopted on the basis of the diffusion approach described above [90], where a value of 10 mm was estimated for R. p_{dam} is the first parameter of our model, accounting for all those biochemical events (e.g. successful binding of the signal to membrane surface receptors, production of ROS and other molecules involved in intra-cellular signalling etc.) which can lead to observable cytogenetic damage in bystander cells. When applying the model in its second version, p_{em} is the second parameter. Fig. 6.1 shows an example chosen among simulation outcomes obtained with 400000 molecules starting from a 5 mm radius hemi-spherical surface with centre in position $(0, 0)$ on the $x - y$plane. Quantitative agreement with the 3% fraction of damaged cells observed experimentally [73, 92] was obtained with $p_{dam} = 0.00005$. As expected, the fraction of damaged cells increases with time according to a saturation-like pattern. The saturation time strongly depends on the amount of culture medium, since more medium requires longer saturation times. The values found in this work (0.5-1 hour for 20 mm thick medium, 10 h for 1 mm) are consistent with measurements of IL-8 concentration, which was found to remain roughly constant in the time range 0.5-20 h after irradiation [86]. As shown in Fig. 6.1, making the signals start diffusing from the irradiated cell leads to a scenario where the damaged cells tend to cluster in the vicinity of the irradiated cell itself. This might not necessarily be the case, since the damaged cells observed experimentally were distributed over the dish almost randomly [73, 92]. A 'version 2' of the model was then developed, assuming that also bystander, damaged cells can in turn emit
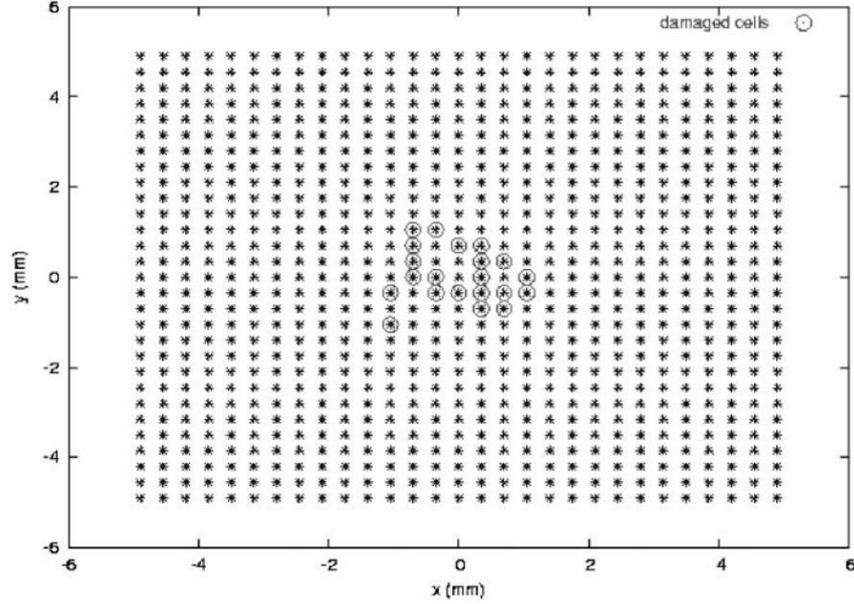
126

Figure 6.1: Top view of the 841-cell grid with an example of damage pattern obtained simulating [71] the release of 400.000 signalling molecules by the irradiated cell [which is in position (0,0)] in a 20 μm thick culture medium, with $p_{dam} = 0.00005$.

signals with probability p_{em}.

Fig. 6.2 shows an example of simulation outcome obtained with $N = 100$ (both from the irradiated cells and from the other emitting cells), $p_{dam} = 0.04$, $p_{em} = 0.5$ and $20mm$ thick culture medium. The value of p_{em} was chosen on the basis of the assumption that bystander cells release signals with lower probability with respect to directly irradiated cells, whereas $p_{dam} = 0.04$ leads to quantitative agreement with the 3% damage fraction observed experimentally. Under the assumption that also bystander (damaged) cells can release signals with probability pem, the damage time-dependence shows a sigmoidal shape. What is represented in Fig. 6.2 is the damage pattern at one hour after irradiation. Indeed, under this assumption each (bystander) cell on the dish eventually becomes damaged, unless there are limitations to the duration of the release and diffusion process. This might represent a possible future development for this work. Also with the second version of the model, the damaged cells tend to 'appear' as grouped in subsequent clusters, starting from the vicinity of the mirradiated cell and progressively 'moving' towards the borders of the dish with increasing time. This led us to revisit the first version of the model, introducing a slight modification: only the irradiated cell was assumed to release signals, but the molecules were made diffusing starting from 3-D random locations in the culture medium rather than from the irradiated cell itself. This is consistent with the fact that soon after irradiation, the dish needs to be moved and transported to the incubator, that might produce a 'shaking' effect in the medium and thus result in a random distribution of the signals within the medium itself. An example of simulation outcome obtained under this assumption is reported in Fig. 6.3, from which it is
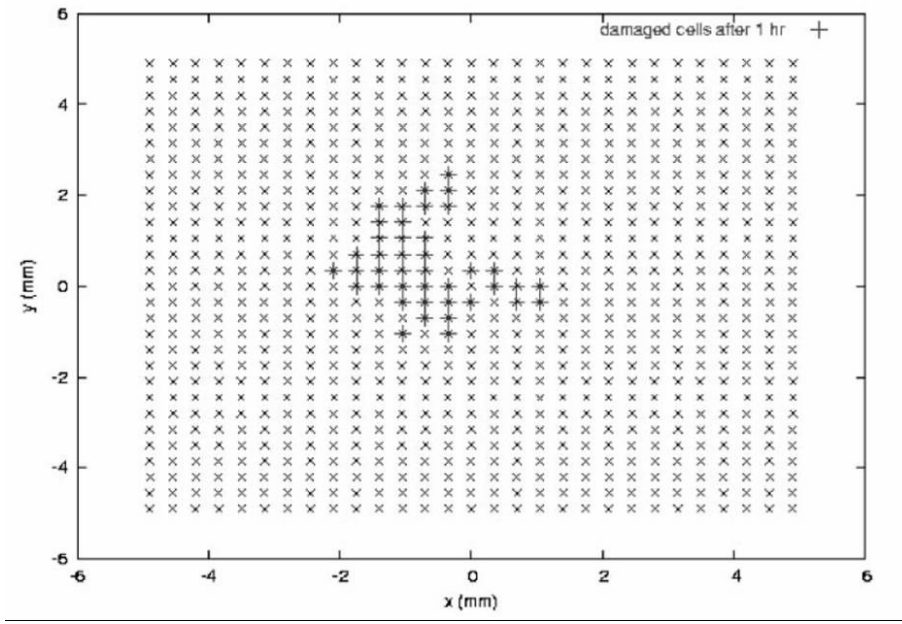
127

Figure 6.2: Top view of the 841-cell grid with an example of 1 h post-irradiation damage pattern obtained simulating [71] the release of N signalling molecules not only by the irradiated cell [position (0,0)] but also by bystaner damaged cells, with probability p_{em}. The example shown in the figure refers to $N = 100$, $p_{dam} = 0.04$, $p_{em} = 0.5$, medium thickness of 20 μm.

apparent that the damaged cells are randomly distributed throughout the dish, in qualitative agreement with the considered experimental data. As like with the first version of the model, quantitative agreement with the observed 3% fraction of damaged cells was obtained with $p_{dam} = 0.00005$.

6.3 Discussion

Available theoretical models of radiation-induced BEs were reviewed in this Chapter, and a fully Monte Carlo approach under development at the University of Pavia was presented. The focus was mainly on the assumptions adopted by the authors on the underlying mechanisms, which are still largely unknown. At least for in vitro high-LET irradiation of 2-D cell layers, it is generally accepted that the overall response in terms of cytogenetic damage is due to a direct response from cells affected by radiation energy deposition superimposed on a bystander response from a subpopulation of unirradiated cells. While one of the models [89] does not make any explicit assumption on this subpopulation, the others make the assumption that the damage occurring in bystander cells is a response to protein-like molecular signals which are released following irradiation and diffuse in the extracellular environment, possibly interacting with unirradiated cells and leading to cytogenetic damage. According to the BSDM model [90], which implies relatively low numbers of involved signals, each chemical reaction between a signal and a (bystander) cell will evolve into cytogenetic damage. By contrast, our
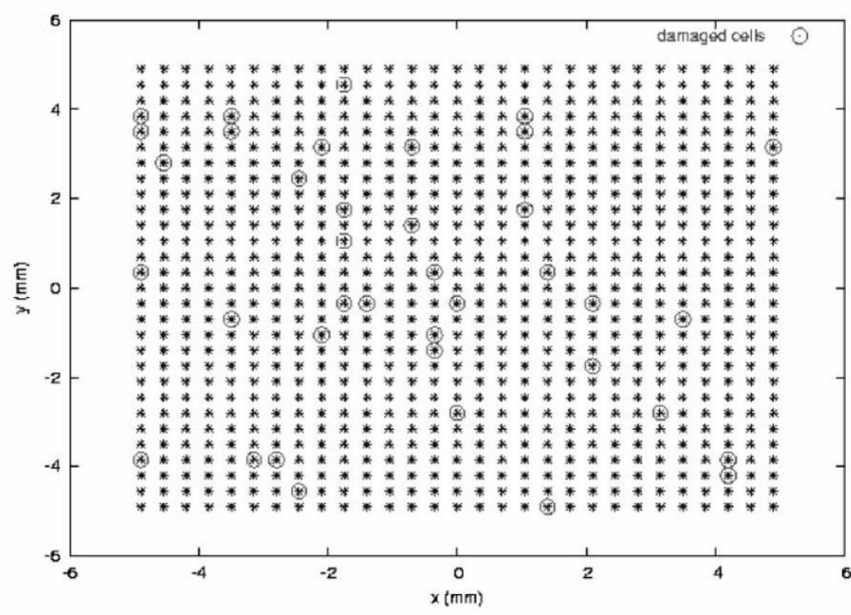
128

Figure 6.3: Top view of the 841-cell grid with an example of 1 damage pattern obtained simulating [71] the release of 400.000 signalling molecules by the irradiated cell [which is in position (0,0)] in a 20μm thick culture medium with $p_{dam} = 0.00005$. In contrast with Fig. 6.1, here the molecules start diffusing from 3-D random locations within the culture medium.

approach, which is based on much larger signal numbers on the basis of cytokine concentration data, implies a probability p_{dam} much lower than unity. All the considered models include a certain number of parameters (two for the literature models and our model in its 'version 2', one for our model in its 'version 1') that can be estimated by comparisons with data. The unavoidable use of free parameters, which should be kept at minimum in mechanistic modelling, outlines the lack of information affecting BE phenomena. It is indeed highly desirable that more data become available on the intermediate steps leading from irradiation to bystander cell damage, including the dependence on cell type and cell-cycle stage, cell-to-cell contact, time between irradiation and observation, signal(s) identification and concentration etc. On this latter point, very useful information can be provided by concentration measurements of specific candidate signals such as cytokines, ROS and NO.

Although most of the currently available information on BEs (both from experiments and from theoretical studies) is related to in vitro irradiation, there exists evidence suggesting BEs can also occur in vivo. This is a crucial point, since it raises the question of the implications of such phenomena for radiation protection and possibly for radiotherapy. Indeed, if BEs occur also in vivo, the linear no-threshold approximation for low dose risk might not necessarily hold. A detailed discussion on this is beyond the scope of this work, which is more focussed on the underlying mechanisms rather than the implications. However, it is worth mentioning that while mutation and transformation of bystander cells might imply a supra-linear risk at low doses, lethal effects such as clonogenic inactivation

129

and apoptosis suggest that BE might represent a protective strategy developed by the tissue as a whole, consisting of preventing proliferation of functional groups of potentially damaged cells by apoptosis/inactivation or premature differentiation [93]. However, the process is so complex that in vitro data cannot be used for straightforward extrapolations to in vivo scenarios, although they are useful to elucidate the mechanisms under controlled conditions. In this framework very useful information can be provided by experiments with tissue explants and/or 3-D artificial tissues [94].

Chapter 7

Conclusions and future perspectives

This work belongs to one of the various research lines of the Radiobiology and Biophysics Group of the University of Pavia and it is focussed mainly on the study and the modelization of radio-induced DNA damage with the help of the PAR-TRAC Monte Carlo code, developed in collaboration with the GSF Institute of Munich, and on the modelization of cellular communication and bystander effect following irradiation.

Track structure analysis based on computer simulations, described in Chapter 1, requires the cross sections for the interaction of primary and secondary charged particles in liquid water which serves as a substitute of soft tissue in most Monte Carlo codes.

In Chapter 2, starting from the basic principles of Perturbation Theory and Dielectric Theory [19, 20, 21], we rewieved and discussed how to express in a general form the cross sections for such inelastic processes in condensed phase matter in terms of the dielectric properties of the medium. These calculations give an idea of the adopted theoretical bases and starting point of the different theoretical approaches avaliable in literature [16, 17, 18, 24, 25] for the study of such extremely complex processes.

For what concernes cross section calculations, one of the main perspective for the future is the upgrade of the PARTRAC code for relativistic energies, that is for heavy ions with energy greater than 1 GeV per nucleon. Actually, some test simulations and results on DNA fragmentation for heavy ions with energy around 1 GeV/u are under investigation. Relativistic medium polarization effects like Fermi density effect mainly influences the cross sections at energy higher than 1 GeV/u and are currently not considered in the code. Comparison between the preliminary test simulations for 1 GeV/u iron ions and experimental data gives a quite good agreement but at the same time gives an idea about the limitation of the actual version of the PARTRAC code. As an example to clarify this point, what happens is that the Fermi density correction to the total ionization cross section for proton impact in liquid water [70] becomes more and more important

above 1 GeV, giving a negative contribution to the total ionization cross section without correction and in this way, if the correction is not taken into account, we overestimate the total cross section for inelastic processes.

The pathways complexity leading to radiation induced strand breaks have not yet been fully clarified. Previous studies (both theoretical and experimental) on radiation-induced DNA damage indicated that the induction of SSBs and DSBs is generally linear with dose. The results presented in Chapter 4, focussed on the protective role of DNA/chromatin organization, showed that the absolute yield of DNA damages per unit dose (usually expressed as SSB $Gy^{-1}Da^{-1}$ and DSB $Gy^{-1}Da^{-1}$) has a significant dependence on factors such as radiation quality, the level of DNA higher-order organization and DNA environment scavenging capacity. We extended a previous work [42] simulating USX- and proton- radiation induced damage with different energies for different DNA target structures. The PARTRAC code has been of great help in clarifying the complexity of the such processes regarding DNA damage induction. In this study, one of the main features of PARTRAC gave us the possibility of varying the contributions of the modulating factors mentioned above such as the different DNA structures implemented in the code.

In the context of the evelution of risk associated with astronauts' exposure to high-LET radiation (e.g. GCRs), the results given in Chapter 5, obtained by comparison between the upgraded PARTRAC code simulation data for iron ions and experimental data, showed the predictive power of the code against the data concernig the number of fragments in all the avaliable ranges and in non-experimentally detectabe ranges. The good agreement between simulated and experimental fragment spectra in the complete fragment range demonstrates the reliability of the improved version of the code and the future possibility of an extension of this kind of study to other different ions and to other research fields (e.g. carbon and oxygen ions for hadrontherapy). The possibility of testing different target structures and the recent upgrade of the PARTRAC code for heavy ions will also permit us to combine the two preceeding studies, allowing a further extention of the investigation of the role of DNA structure in the case of irradiation with heavy ions.

In Chapter 6, concerning the modelization of cellular communication following irradiation, available theoretical models of in vitro radiation induced *bystander effect* were rewieved along with a fully stochastic model using Monte Carlo methods, which is under development at the University of Pavia. This phenomenon was largely observed for different radiation types and for a wide damage spectrum [72, 73, 74, 75, 76, 77, 78, 79, 80, 81] including both lethal and non lethal damage. For this reason, the scenario at low doses can be further complicated by the possible occurrence of these 'non-targeted' effects. The unavoidable use of free parameters (e.g. type and number of released signals) which should be kept at minimum in mechanistic modelling, outlines the lack of information affecting BEs phenomena. It is indeed highly desirable that in future more data become available on the intermediate steps leading from irradiation to bystander

132

cell damage, including the dependence on cell type and cell-cycle stage, cell-to-cell contact, time between irradiation and observation, signal(s) identification and concentration etc. On this latter point, very useful information can be provided by concentration measurements of specific candidate signals such as cytokines, ROS and NO. Further investigations, both experimental and theoretical, will help to better understand the mechanism underlying specific in vitro situations taking into account that in vivo scenario can be very different, and that the knowledge acquired in vitro cannot be directly extrapolated to draw conclusions on in vivo low-dose exposures.

Bibliography

[1] F. Ballarini, D. Alloni et *al.*, Radiation risk estimation: modelling approaches for 'targeted' and 'non-targeted' effects, *Adv. Space Res.*, (2007) (*in press*).

[2] K. H. Beckurts and K. Wirtz, *Neutron Physics*, Springer, Berlin, 1964.

[3] J. Lamarsh, *Introduction to Nuclear Reactor Theory*, Addison-Wesley, 1972.

[4] U. Fano, *Phys. Rev.* **72**, 26 (1974). (b) M. Inokuti, D. A. Douthat, and A. R. P. Rao, *Phys. Rev.*, **A22**, 445 (1980). (c) W. Neumann, in *Seventh Symposium on Microdosimetry*, J. Booz, H. G. Herbert, and H. D. Hartfiel (Eds.), Report EUR 7147, Harwood Academic, London, 1981, p. 1067.

[5] W. E. Wilson and H. G. Paretzke, in *Fourth Symposium on Microdosimetry*, J. Booz, H. G. Herbert, R. Eickel, and A. Waker (Eds.), Report EUR 5122, Commission of the European Communities, Luxemburg, 1974, p. 113.

[6] (a) L. G. Christoporu, *Atomic and Molecular Radiation Physics*, Wiley, New York, 1971. (b) L. G Christoporu (Ed.), *Electron-Molecule Interactions and their Applocations*, 2 vols., Academic Press, New York, 1984.

[7] S. E. Schnatterly, in *Solid State Physics*, Vol. 34, H. Ehrenreich, F. Seitz, and D. Turnbull (Eds.), Academic Press, New York, 1979, p. 275.

[8] H. Raether, *Excitations of Plasmons and Interband Transitions is Solids*, Springer Tracts in Modern Physics 88, Springer-Verlag, New York, 1980, p. 1.

[9] D. Rapp and P. Englander-Golden, *J. Chem. Phys.*, **43**, 1464 (1965).

[10] F. J. de Heer and M. Inokuti, *Electron Impact Ionization*, in T. D. Mark and G. H. Dunn (Eds.), Springer-Verlag, Heidelberg, 1985.

[11] H. G. Paretzke, *Radiation Track Structure Theory*, in *Kinetics of Nonhomogeneous Processes*, G. R. Freeman (Ed.), Wiley Interscience Publication, New York, 1987.

[12] J. Kiefer, *Biological Radiation Effects*, Springer-Verlag, 1990.

[13] M. Liotta, *Effetti della Struttura di Traccia sulle Distribuzioni Radiali di Dose e di Danni al DNA Indotti da Particelle Cariche di Interesse in Adroterapia*, 'Laurea' Thesis, University of Pavia, 2004.

[14] S. Molinelli, *Simulazione della distribuzione del danno subcellulare indotto da protoni e particelle alfa*, 'Laurea' Thesis, University of Pavia, 2003.

[15] V. P. Zaikov et *al*, VINITI 600-187 (1987) 75.

[16] M. Dingfelder et *al.*, *Rad. Phys. Chem.*, **53** (1988) 1-8.

[17] M. Dingfelder et *al.*, *Rad. Phys. Chem.*, **59** (2000) 255-275.

[18] M. Inokuti, *Rev. Mod. Phys.*, **43**, No. 3, (1971).

[19] U. Fano, *Ann. Rev. Nucl. Sci.*, **13**, (1963) 1-66.

[20] L. D. Landau and E. M. Lifshitz, *Electrodynamics of Continuous Media*, 2nd Ed., Pergamon Press, London, 1970.

[21] U. Fano, *Phys. Rev.*, **102** (1956) 385-387.

[22] J. M. Heller et *al.*, *J. Chem. Phys*, **60** (1974) 3484.

[23] V. V. Balashov, *Interaction of Particles and Radiation with Matter*, Springer-Verlag, Berlin, 1993.

[24] D. Emfietzoglou, *Rad. Phys. Chem.*, **66** (2003) 373-385.

[25] M. Dingfelder and M. Inokuti, *Radiat. Environ. Biophys.*, **39** (1999) 93-96.

[26] B. Lewin, *Il Gene VIII*, Zanichelli, 2006.

[27] J. E. Coogle, *Effetti Biologici delle Radiazioni*, Ed. Minerva Medica, 1998.

[28] W. Friedland et *al.*, *Radiat. Res.*, **150** (1998) 170-182.

[29] W. Friedland et *al.*, *Radiat. Environ. Biophys.*, **38** (1999) 39-47.

[30] R. Chandrasekaran et *al.*, In *Landolt-Bornstein, Numerical Dataand Functional Relationship in Science and Technology*, New Series VII, 1b, Springer-Verlag, Berlin, 1989.

[31] W. Saenger, *Principles of Nuleic Acid Structure*, Springer-Verlag, New York, 1994.

[32] F. Ballarini et *al.*, *Radiat. Environ. Biophys.*, **39** (2000) 179-188.

[33] E. Pomplun and M. Terrisol, *Radiat. Environ. Biophys.*, **33** (1994) 279-292.

[34] J. Widom, *Annu. Rev. Biophys. Byophys. Chem.*, **18** (1989) 365-395.

[35] D. Alloni et *al.*, *Rad. Prot. Dosim.*, **122** (2006) 141-146.

[36] W. R. Holley and A. Chatterjee, *Radiat. Res.*, **145** (1996) 188-199.

[37] D. E. Charlton et *al.*, *Int. J. Radiat. Biol.*, **56** (1989) 1-19.

[38] A. Ottolenghi et *al.*, *Radiat. Environ. Biophys.*, **34** (1995) 239-244.

[39] J. S. Bedford, *Int. J. Radiat. Oncol. Biol. Phys.*, **21** (1991) 1457-1469.

[40] D. T. Goodhead, *Int. J. Radiat. Biol.*, **65** (1994) 7-17.

[41] D. T. Goodhead, *Int. J. Radiat. Biol.*, **63** (1993) 543-566.

[42] A. Valota et *al.*, *Int. J. Radiat. Biol.*, **79** (2003) 643-653.

[43] F. Ballarini et *al.*, *Radiat. Environ. Biophys.*, **39** (2000) 179-188.

[44] J. R. Milligan et *al.*, *Radiat. Res.*, **133** (1993) 151-157.

[45] J. Fulford et *al.*, *Int. J. Radiat. Biol.*, **77/10** (2001) 1053-1066.

[46] J. F. Ward et *al.*, *Factors controlling the radiosensitivity of cellular DNA*, In *Microdosimetry - An Interdisciplinary Approach*, (1997) 57-64.

[47] J. Fulford et *al.*, *J. Phys. Chem. A*, **103** (1999) 11345-11349.

[48] J. A. LaVerne et *al.*, *Rad. Res.*, **141** (1995) 208-215.

[49] A. M. Miterev, *High Energy Chem.*, **28** (1990) 323-334.

[50] D. Alloni et *al.*, Modeling of DNA fragmentation induced in human fibroblasts by ^{56}Fe ions, *Adv. Space Res.*, (2007) (*in press*).

[51] *Shielding strategies for human space exploration*, NASA Conference Publication 3360, December, 1997.

[52] A. Ottolenghi et *al.*, *Radiat. Environ. Biophys.*, **36** (1997) 97-103.

[53] F. A. Cucinotta and M. Durante, *Lancet. Oncol.*, **7** (2006) 431-435.

[54] M. Durante et *al.*, *Cytogenet. Genome Res.*, **103** (2003) 40-46.

[55] J. F. Ziegler (SRIM.com Annapolis, MD 21 037 USA), J. P. Biersack (Hahn-Meitner Inst. 1, Berlin, Germany).

[56] G. Kraft, *Radiobiological effect of highly charged ions. Their relevance for tumor therapy and radioprotection in space*, In *The Physics of Highly and Mutiply Charged Ions*, Chapter 10, F. J. Currel Kluwer, Academic Press, 1994.

[57] W. Friedland et *al.*, *Radiat. Res.*, **159** (2003) 401-410.

[58] B. Rydberg, *Radiat. Res.*, **145** (1996) 200-209.

[59] B. Rydberg et *al.*, *J. Mol. Biol.*, **284** (1998) 71-84.

[60] M. Belli et *al.*, *Int. J. Radiat. Biol.*, **78**, (2002) 475-482.

[61] D. Frankenberg et *al.*, *Radiat. Res.*, **151** (1999) 540-549.

[62] Höglund et *al.*, *Int. J. Radiat. Biol.*, **76** (2000) 539-547.

[63] M. Löbrich et *al.*, *Int. J. Radiat. Biol.*, **70** (1996) 493-503.

[64] H. C. Newman et *al.*, *Int. J. Radiat. Biol.*, **71** (1997) 347-363.

[65] A. Campa et *al.*, *Int. J. Radiat. Biol.*, **80** (2004) 229-238.

[66] F. Antonelli et *al.*, *Adv. Space Res.*, **34** (2004) 1353-1357.

[67] M. Belli et *al.*, *Radiat. Res.*, **78** (2006) 713-720.

[68] A. Campa et *al.*, *Int. J. Radiat. Biol.*, **81** (2005) 841-854.

[69] M. Pinto et *al.*, *Radiat. Res.*, **162** (2004) 453-463.

[70] M. Dingfelder et *al.*, *Rad. Prot. Dosim.*, Vol. 122, No. 1-4 (2006).

[71] F. Ballarini, D. Alloni et *al.*, *Rad. Prot. Dosim.*, **122** (2006) 244-251.

[72] C. Mothersill et *al.*, *Int. J. Radiat. Biol.*, **71** (1997) 421-427.

[73] K. Prise et *al.*, *Int. J. Radiat. Biol.*, **74** (1998) 793-798.

[74] H. Nagasawa et *al.*, *Radiat. Res.*, **152** (1999) 552-557.

[75] H. Zhou et *al.*, *Proc. Natl. Acad. Sci.*, USA **97**, (2000) 2099-2104.

[76] R. C. Miller et *al.*, *Proc. Natl. Acad. Sci.*, USA **96**, (1999) 19-22.

[77] S. G. Sawant et *al.*, *Radiat. Res.*, **155** (2001) 397-401.

[78] H. Nagasawa et *al.*, *Cancer Res.*, **52** (1992) 6394-6396.

[79] A. Desphande et *al.*, *Radiat. Res.*, **145** (1996) 260-267.

[80] E. I. Azzam et *al.*, *Proc. Natl. Acad. Sci.*, USA **98** (2001) 473-478.

[81] H. Yang et *al.*, *Oncogene*, **24** (2005) 2096-2103.

[82] F. Ballarini et *al.*, *Mutat. Res.*, **501** (2002) 1-12.

[83] P. J. Coates et *al.*, *Mutat. Res.*, **568** (2004) 5-20.

[84] C. Shao et *al.*, *Int. J. Cancer*, **116** (2005) 45-51.

[85] P. K. Narayanan et *al.*, *Radiat. Res.*, **152** (1999) 57-63.

[86] A. Facoetti et *al.*, *Radiat. Prot. Dosim.*, **122** (2006) 271-274.

[87] B. E. Lehnert et *al.*, *Proc. Eleventh Int. Congress of Radiat. Res.*, **2** (1999) 488-491.

[88] M. H. Barcellos-Hoff et *al.*, *Radiat. Res.*, **156** (2001) 618-627.

[89] J. D. Brenner et *al.*, *Radiat. Res.*, **155** (2001) 402-208.

[90] H. Nikjoo et *al.*, *Int. J. Radiat. Biol.*, **79** (2003) 43-52.

[91] M. P. Little et *al.*, *J. Theor. Biol.*, **232** (2005) 329-338.

[92] O. V. Belyakov et *al.*, *Br. J. Cancer*, **84** (2001) 674-679.

[93] O. V. Belyakov et *al.*, *Radiat. prot. Dosim.*, **99** (2002) 249-251.

[94] O. V. Belyakov et *al.*, *Proc. Natl. Acad. Sci.*, USA **102** (2005) 14203-14208.

List of publications

- F. Ballarini, D. Alloni, G. Battistoni, F. Cerutti, A. Ferrari, E. Gadioli, M. V. Garzelli, M. Liotta, A. Mairani, A. Ottolenghi, H. G. Paretzke, V. Parini, M. Pelliccioni, L. Pinsky, P. Sala, D. Scannicchio, S. Trovati and M. Zankl (2006), Modelling human exposure to space radiation with different shielding: the FLUKA code coupled with anthropomorphic phantoms, *J. of Phys. Conf. Series*, **41** (2006) 135.

- F. Ballarini, D. Alloni, A. Facoetti, A. Mairani, R. Nano and A. Ottolenghi), *Modelling radiation-induced bystander effect and cellular communication*, *Radiat. Prot. Dosim.*, **122**,(2006) 244-251.

- D. Alloni, F. Ballarini, W. Friedland, M. Liotta, S. Molinelli, A. Ottolenghi, H.G. Paretzke and M. Rossetti (2006), Role of DNA/chromatin organisation and scavenging capacity in USX- and proton- induced DNA damage, *Radiat. Prot. Dosim.*, **122** (2006) 141-146.

- D. Alloni et *al.*, Modelization of DNA fragmentation induced in human fibroblasts by ^{56}Fe ions *Adv. Space Res.*, **40** (2007) 1401-1407.

- F. Ballarini, D. Alloni, A. Facoetti, A. Mairani, R. Nano, A. Ottolenghi (2007), Radiation risk estimation: modelling approaches for targeted and non-targeted effects, *Adv. Space Res.*, **40** (2007) 1392-1400 .

- A. Ottolenghi, D. Alloni, F. Ballarini, D. Scannicchio, Modelling the evolution of radiobiological damage with focus on target structures, *RADAM Conference*, Potsdam, *Book of abstracts*, 2005, p. 33

- F. Ballarini, D. Alloni, G. Battistoni, F. Cerutti, A. Ferrari, E. Gadioli, M. V. Garzelli, A. Mairani, A. Ottolenghi, H. G. Paretzke, V. Parini, M. Pelliccioni, L. S. Pinsky, P. R. Sala, D. Scannicchio, M. Zankl, Modelling human exposure to space radiation with different shielding: the FLUKA code coupled with anthropomorphic phantoms. *The NPDC19 conference*, Pavia, 5-9 Sept. 2005, *Book of abstracts*.

- F. Ballarini, D. Alloni, A Facoetti, A. Mairani, A. Ottolenghi, Modelling approaches in investigating cell communication and bystander effects following irradiation, *The 14th Symposium of Microdosimetry*, Venice, November 2005 (invited talk), *Book of abstracts.*

- D. Alloni, F. Ballarini, W. Friedland, M. Liotta, S. Molinelli, A. Ottolenghi, H.G. Paretzke, M. Rossetti, Role of DNA/chromatin organisation and scavenging capacity in USX- and proton- induced DNA damage,*The 14th Symposium of Microdosimetry*, November 2005 *Book of abstracts.*

- D. Alloni, F. Ballarini, A. Mairani and A. Ottolenghi, Bystander Effect: a diffusion-based modelling approach (oral presentation). Bad Honnef, *RISC-RAD annual meeting*, April 2005, *Book of abstract.*

- F. Ballarini, D. Alloni, A. Facoetti, A. Mairani, R. Nano, A. Ottolenghi, Theoretical models and simulation codes to investigate bystander effects and cellular communication at low doses. *36th COSPAR Scientifc Assembly*, Bejing, China, July 2006, *Published on CD-ROM.*

- A. Campa, D. Alloni, F. Ballarini, M. Belli, G. Esposito, W. Friedland, M. Liotta, A. Ottolenghi, H. Paretzke, Modellizazione della frammentazione del DNA indotta in fibroblasti umani da ioni Fe-56, *Convegno SIRR*, Bologna, Novembre 2006, *Book of Abstracts.*

- A Facoetti, D Alloni, F Ballarini, A Mairani, L Mariotti, R Nano, A Ottolenghi, How do experimental conditions and radiation affect cytokine signals?, *Int. Cong. Radiat. Res*, San Francisco, July 2006.

- G. Magrotti, D. Alloni, A. Borio di Tigliole, M. Cagnazzo, M. Coniglio, S. Manera, M. Prata, A. Salvini, G. Scian, The new area radiation monitoring system of the TRIGA nuclear research reactor facility of the University of Pavia, *11th International Topical Meeting on Research Reactor Fuel Management* (ENS RRFM), Lyon, France, Conference proceedings, 2007 .

- D. Alloni, A. Borio di Tigliole, M. Cagnazzo, M. Coniglio, G. Magrotti, S. Manera, A. Piazzoli, M. Prata, A. Salvini, G. Scian, The cyclotron facility at the Laboratory of Applied Nuclear Energy (L.E.N.A.) of the University of Pavia, CYCLOTRONS 2007, *18th International Conference on Cyclotrons and their Applications*, Giardini Naxos, Italy, *Conference Proceedings.*

- D. Alloni, F. Antonelli, F. Ballarini, M. Belli, A. Campa, V. Dini, G. Esposito, W. Friedland, M. Liotta, A. Ottolenghi, H. G. Paretzke, G. Simone, E. Sorrentino, M. A. Tabocchini, Small DNA fragments induced in human fibroblasts by 56Fe ions: experimental data and MC simulations, Abstract, *IBIBA Conference Proceedings*, September 2007.